

4-2014

Assessment of the Thermal Advantages of Biased Supersonic Cooling

Michael J. Carkin
Embry-Riddle Aeronautical University - Daytona Beach

Follow this and additional works at: <https://commons.erau.edu/edt>



Part of the [Aerospace Engineering Commons](#)

Scholarly Commons Citation

Carkin, Michael J., "Assessment of the Thermal Advantages of Biased Supersonic Cooling" (2014).
Dissertations and Theses. 34.
<https://commons.erau.edu/edt/34>

This Thesis - Open Access is brought to you for free and open access by Scholarly Commons. It has been accepted for inclusion in Dissertations and Theses by an authorized administrator of Scholarly Commons. For more information, please contact commons@erau.edu.

Assessment of the Thermal Advantages of Biased Supersonic Cooling

by

Michael J. Carkin

A Thesis Submitted to the College of Engineering Department of Aerospace Engineering in
Partial Fulfillment of the Requirements for the Degree of
Master of Science in Aerospace Engineering

Embry-Riddle Aeronautical University
Daytona Beach, Florida
April 2014

Assessment of the Thermal Advantages of Biased Supersonic Cooling.

by

Michael J. Carkin

This thesis was prepared under the direction of the candidate's thesis committee chair, Dr. Sandra Boetcher, Professor, Daytona Beach Campus, and thesis committee members Dr. Lakshmanan L. Narayanaswami, Professor, Daytona Beach Campus, and Dr. Eric R. Perrell, Professor, Daytona Beach Campus, and has been approved by the thesis committee. It was submitted to the Department of Aerospace Engineering in partial fulfillment of the requirements for the degree of Master of Science in Aerospace Engineering

Thesis Review Committee:



Sandra Boetcher, Ph.D.
Committee Chair



Lakshmanan L. Narayanaswami, Ph.D.
Committee Member



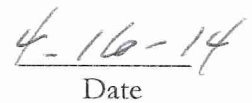
Eric R. Perrell, Ph.D.
Committee Member



Graduate Program Chair, Aerospace Engineering
Yi Zhao, Ph.D.



Associate Vice President of Academics
Robert Oxley, Ph.D.


Date

Acknowledgements

I would like to begin by giving my utmost thanks to Dr. Sandra Boetcher who not only oversaw the execution of this work, but realized the potential of the research at its earliest stages. Without her willingness to oversee and provide recommendations throughout the course of research, the work would not have been produced.

Secondly, I would like to thank a number of individuals for their contributions to the thesis: Mike Borgi for aiding in the gridding process, members of the ERPL CFD Team for their numerical investigations, Gregory Carkin for on-going technical support, and Matt Meyers for formatting assistance.

I'd also like to thank those who I consider my support structure: my parents for their undying support and aid, Aliraza Rattansi, Warren Hiner, and Alvydas Civinskas for numerous recommendations, and Kelly Donnenwirth for seeing me through the thick and thin of the research.

Lastly, I would like to thank both Professor Lakshmanan L. Narayanaswami and Professor Eric R. Perrell for their willingness to review the research presented in the following work.

I do not think there is any thrill that can go through the human heart like that felt by the inventor as he sees some creation of the brain unfolding to success... such emotions make a man forget food, sleep, friends, love, everything.

-Nikola Tesla

Abstract

Researcher: Michael J. Carkin
Title: Assessment of the Thermal Advantages of Biased Supersonic Cooling
Institution: Embry-Riddle Aeronautical University
Degree: Master of Science in Aerospace Engineering
Year: 2014

The following work investigates an alternative supersonic film cooling method for hydrogen-fueled, gas-generator cycle rocket engines. The research is intended to serve as an initial proof-of-concept for a biased supersonic film cooling method envisioned for nozzle extension thermal management. The proposed method utilizes a dual-stream injection process that leverages the high heat capacity of the fuel-rich gas-generator gases. By comparing the proposed cooling strategy to the conventional mixed injection process, the research numerically validates the biased supersonic film cooling scheme for low supersonic slot Mach numbers. The average film cooling effectiveness was improved 5%-8% with increases as high as 12%. The average reduction in wall temperature ranged from 9%-15% with maximum reductions as high as 36% over the conventional method.

Table of Contents

	Page
Thesis Review Committee	ii
Acknowledgements	iii
Abstract.....	v
List of Tables	x
List of Figures	xi
Nomenclature	xiv
Greek.....	xv
List of Acronyms and Abbreviations	xvi
Chapter	
I Introduction.....	1
Motivation	1
Problem Description.....	4
Proposed Cooling Method.....	7
Objective Statement.....	7
II Film Cooling Overview.....	8
Introduction	8
Film Cooling Classification.....	10
Discrete Injection	10
Slot Injection	11
Subsonic Injection	13
Supersonic Injection.....	13
Core-Driven.....	14
Wall-Jet.....	15

	Previous Work	16
	Introduction.....	16
	Analytical Work.....	16
	Experimental Work	18
	Numerical Work	18
	Film Cooling Reviews	19
III	Methodology.....	20
	Introduction	20
	Phase I: Preliminary Steps.....	20
	Phase II: Computational Gas Model.....	20
	Phase III: Biased Flat Plate Models	21
	Phase IV: Implementation	21
IV	Preliminary Steps.....	23
	Introduction	23
	Flat Plate Analysis	23
	CAL-Tech Experiments.....	23
	CFD Flat Plate Models	25
	Turbulence Model Selection	27
	Engine Selection.....	29
	Vulcain II Parameters.....	30
	Nozzle Contour.....	32
	Phase I: Nozzle Extension	32
	Phase II: Combustion Chamber.....	34
	Phase III: Throat Region	34

	'Default' Engine Geometry	35
	Conventional and Biased Supersonic Film Cooling Definitions.....	37
V	Computational Gas Model	41
	Introduction	41
	Alternative Gas Models	41
	Core-Flow Composition.....	44
	Core-Flow Specific Heat Approximation	45
	Core-Flow Transport Properties.....	48
	Turbine Exhaust Gas Composition and Properties	48
	Lennard-Jones Parameters	49
	Film Mole Fraction Adjustment.....	52
	Temperature-Dependent Gas Property Plots	55
	Constituent Temperature-Dependent Plots	55
	Gas Mixture Temperature-Dependent Plots.....	57
VI	Biased Flat Plate Analysis	59
	Introduction	59
	Model Parameters.....	59
	Proof-of-Concept.....	60
VII	Modified Vulcain II	62
	Introduction	62
	Geometry and Slot Injector	62
	Meshing Process	64
	Mesh Independence Study	64
	Finalized Mesh	67

	Model Parameters.....	67
	Parameter Ratio Matching Process	68
VIII	Results.....	71
	Biased Flat Plate Investigation	71
	Biased Flat Plate Film Cooling Effectiveness.....	71
	Biased Flat Plate Wall Temperature Reduction.....	72
	Modified Vulcain II Investigation.....	72
	Modified Vulcain II Film Cooling Effectiveness.....	73
	Modified Vulcain II Wall Temperature Reduction.....	75
IX	Discussion and Conclusion	78
	Introduction	78
	Film Cooling Effectiveness.....	78
	Wall Temperature Reduction.....	79
	Conclusions.....	80
X	Extension and Future Work.....	81
	Hydrocarbon Analysis	81
	Fluid Structure Interactions	81
	Turbulence Effects.....	82
	References	82
	Appendices	
A	Engine Coordinates and Contours	91
B	Tabulated CEA Results.....	95
C	Gas Property Curve-Fit Coefficients and Water Models.....	98
D	Matlab Script Files	102

List of Tables

	Page
Table	
1 Flat-plate model boundary conditions.....	26
2 Investigated turbulence model descriptions	27
3 Vulcain II combustion chamber characteristics	30
4 Vulcain II nozzle characteristics.....	31
5 Vulcain II gas-generator characteristics.....	31
6 Vulcain II engine characteristics.....	31
7 Mole and mass fractions of core-flow gas mixture.....	45
8 TEG mole and mass fractions.....	49
9 L-J characteristic length parameters and weighted values	50
10 Lennard-Jones parameters and weighted values	50
11 Biased flat plate boundary condition parameters.....	59
12 Film Cooled Nozzle Slot Locations.....	63
13 Mesh independence model mesh sizes.....	63
14 Slot parameters for film cooled nozzle models.....	64
15 Slot-averaged Mach and corresponding velocity	68
16 Initial film cooling reference parameters and corresponding ratios.....	68
17 Model 'A' film cooling velocity and blowing ratios.....	68
18 Model 'B' film cooling velocity and blowing ratios	69
19 Model 'C' film cooling velocity and blowing ratios	69
20 Model 'D' film cooling velocity and blowing ratios	70

List of Figures

Page

Figure

1	Reaction-Engines' 'Skylon' Single-Stage-to-Orbit (SSTO) vehicle concept.....	1
2	Regenerative cooling channel cross section.....	3
3	Computer model of the J2-X SSFC engine currently under development.	5
4	F-1 gas-generator cycle rocket engine.....	6
5	Discrete film injection on an advanced turbine vane.	11
6	F-1 engine turbine exhaust manifold and nozzle extension film injection.	12
7	Turbulent mixing in binary layer.	14
8	Wall-Jet velocity profile.	15
9	2D film cooling schematic utilized by Simon to predict film cooling effectiveness...	17
10	CAL-Tech experimental set-up.	24
11	CAL-Tech experimental film cooling values extracted from documentation.	25
12	2D flat plate model configuration (side-view).....	25
13	Laminar film cooling effectiveness values for various turbulence models.	28
14	Turbulent film cooling effectiveness values for various turbulence models.	28
15	Vulcain II engine developed by Snecma Motors of Safran Defense Group.	30
16	Vulcain II Hot-Fire Test.....	31
17	Scaled Vulcain II image overlaid with a MOC nozzle contour (orange).....	33
18	Vulcain II thrust chamber and throat region used for immersive sketching.....	35
19	Scaled Vulcain II image overlaid with the image-processing contour (orange)	36
20	Vulcain II approximate geometry.....	37
21	Simplified Vulcain II cooling system schematic.....	38
22	Conventional supersonic film cooling method with mixed TEG injection.....	39

23	Biased supersonic film cooling method with separated TEG injection	40
24	Combustion product mole fraction variation.....	43
25	Hydrogen and water-vapor mole fraction variation	43
26	Core-flow and water-vapor specific heat temperature variation	47
27	Lennard-Jones parameters and weighted values	51
28	Lennard-Jones parameters for core-flow constituent gases	52
29	Atom-count relations between normalized film thickness and mole fraction.....	53
30	Temperature-dependent constituent specific heat.....	55
31	Temperature-dependent constituent viscosity	56
32	Temperature-dependent constituent conductivity.....	56
33	Temperature-dependent gas-mixture specific heat.....	57
34	Temperature-dependent gas-mixture viscosity.....	57
35	Temperature-dependent gas-mixture conductivity.....	58
36	Biased flat plate film cooling effectiveness	60
37	BSSFC wall temperature reduction.....	61
38	Sample injection geometry produced by Matlab script.....	63
39	Default engine contour with splines for mesh independence purposes.....	65
40	Mesh independence analysis: ‘Near-Center Spline’ temperature percent differences	66
41	Mesh independence analysis: ‘Near-Wall Spline’ temperature percent differences	66
42	Biased flat plate film cooling effectiveness for CSSFC and BSSFC Methods.....	71
43	Biased flat plate wall temperature reduction percentage variation	72
44	Model ‘A’ film cooling effectiveness comparisons	73
45	Model ‘B’ film cooling effectiveness comparisons	73
46	Model ‘C’ film cooling effectiveness comparisons	74

47	Model ‘D’ film cooling effectiveness comparisons.....	74
48	Model ‘A’ BSSFC wall temperature reduction	75
49	Model ‘B’ BSSFC wall temperature reduction.....	76
50	Model ‘C’ BSSFC wall temperature reduction	76
51	Model ‘D’ BSSFC wall temperature reduction.....	77

Nomenclature

a : Speed of Sound [m/s]

C_1 : Empirical Constant

C_p : Specific Heat at Constant Pressure

C_v : Specific Heat at Constant Volume

k : Conductivity [W/(m-K)]

M_{slot} : Slot-Averaged Mach Number

\bar{M} : Molecular Weight

P_r : Prandtl Number

\bar{R} : Universal Gas Constant

R_{gas} : Specific Gas Constant

s : Slot Height [m]

T : Static Temperature [K]

T_r : Recovery Temperature

T_o : Stagnation Temperature [K]

x : Axial Distance [m]

x_i : Mole Fraction of Species i

x/s : Non-Dimensional Horizontal Distance

y_i : Mass Fraction of Species i

Greek

β : Blowing Ratio

γ : Specific Heat Ratio

η : Film Cooling Effectiveness Parameter

θ : Temperature Ratio

μ : Dynamic Viscosity [Pa s]

ρ : Density

ϕ_{ij} : Binary Viscosity Parameter

ψ_{ij} : Binary Conductivity Parameter

List of Acronyms and Abbreviations

BSSFC: Biased Supersonic Film Cooling

CATIA: Computer Aided Three-dimensional Interactive Application

CEA: Chemical Equilibrium with Application

CFD: Computational Fluid Dynamics

CSSFC: Conventional Supersonic Film Cooling

EELV: Evolved Expendable Launch Vehicle

ICBM: Intercontinental Ballistic Missiles

K-EpRNG: K-Epsilon Re-Normalization Group Model

K-EpStand: Standard K-Epsilon Model

K-OmegaSST: K-Omega Shear Stress Transport Model

K-OmegaStand: Standard K-Omega Model

LES: Large Eddy Simulation

MOC: Method of Characteristics

NASA: National Aeronautics and Space Administration

RLV: Reusable Launch Vehicle

ReySS: Reynolds Shear Stress Model

SpalartAll: Spalart Allmaras

SSFC: Supersonic Film-Cooling

SSTO: Single-Stage-to-Orbit

TEG: Turbine Exhaust Gas

TM: Technical Memorandum

TSTO: Two-Stage-to-Orbit

Chapter I: Introduction

The purpose of this chapter is to enhance the reader's understanding of film cooling, its applications to rocketry, review previous work in the field, and discuss the motivation behind the research.

1.1 Motivation

For the better part of the twentieth century, only countries with both the technological background as well as the will to invest in space exploration were able to gain access to space. However, the past decade has seen a paramount shift in the space industry with the rise of private, space-oriented companies [1-5]. The shift from government agencies to the commercial sector has revitalized the launch vehicle market as businesses strain to make vehicles both reliable and profitable.

The renewed interest in launch systems has culminated in a series of new launch vehicles and spacecraft. While these efforts are impressive, the future and viability of space-oriented companies will require new vehicles and technology to be developed with cost-effectiveness and reusability in mind.



Figure 1: Reaction-Engines' 'Skylon' Single-Stage-to-Orbit (SSTO) Vehicle Concept [6].

On paper, the most reusable and cost-effective vehicle design follows a single-stage-to-orbit methodology [7]. Unfortunately, such a design is not commercially feasible with the limits of current technology [8]. The next logical design choice is the two-stage-to-orbit (TSTO) launch vehicle option. The Evolved Expendable Launch Vehicle (EELV) program headed by the United States Air Force in the 1990s came to similar conclusions which resulted in the development of the Delta IV and Atlas V launch vehicles [9-10]. While EELVs have a proven track record of reliability, the lack of reusable components keeps the operational costs of these vehicles high.

Numerous sources [7, 11-13] have indicated that replacing EELVs with reusable launch vehicles (RLVs) can greatly reduce the cost per flight. Additional sources [7, 14-17] indicate that the launch vehicle engines, due to their manufacturing, overhaul, and replacement costs, greatly influence the operational cost and turn-around time of reusable launch vehicles. The impact of engine reusability issues within the industry was further underlined in an interview conducted by the author with Alex Lanzendorf: an Embry-Riddle alumnus employed by XCOR Aerospace. In short, previous cost analyses have concluded an alteration in liquid engine technology with emphases on reusability and reduced operational expenses can lower overhead costs.

In principle liquid rocket engines have not drastically changed since the 1950s [18]. Each adaptation that has been introduced since that time period has made small improvements on previous engine designs in one form or another. Such improvements have progressively improved the efficiency and reliability of launch vehicles, but have not dramatically lowered engine production and maintenance costs. Reviewing the costs associated with rocket engine manufacturing and maintenance indicates that one of the driving forces behind liquid rocket engine expenses is the cooling system [19, 20].

Liquid rocket engine cooling has relied on a combination of cooling methods in order to maintain engine temperature within the operational envelope. These cooling systems include radiative cooling, regenerative cooling, ablative cooling, film cooling, and evaporation cooling [20]. While the number of cooling combinations is rather large, the majority of engines rely on a regenerative cooling loop of one form or another. A cross section cut of a series of regenerative cooling passages has been provided in Fig. 2 below.



Figure 2: Regenerative Cooling Channel Cross Section [21].

Regenerative cooling is the method of passing pressurized coolant through narrow channels or tubes fabricated into the nozzle wall. The channels cool the nozzle by soaking up excess heat via convection before expelling the heated liquid, typically fuel, into the combustion chamber or recirculating heat exchanger. Regenerative cooling has been the cooling method of choice for rocket engines due to the technology's maturity and effectiveness [22].

The presence and commonality of regenerative cooling is primarily due to the military history of rocketry. Modern rockets can trace their lineage to the Intercontinental Ballistic Missiles (ICBMs) designed during the Second World War and the Cold War [18, 20, 22-25]. During the development of ICBMs, performance and range were prioritized above cost effectiveness and reusability. The push for performance led to the adoption of

regenerative cooling for ICBMs and eventually by the space programs of the United States and Russia [18, 23, 24]. The pervasive nature of regenerative cooling is a testament to the technology's maturity, but the cooling method does have a series of disadvantages.

Regenerative cooling is a proven technology that provides a means to manage high thermal loads. Conversely, regenerative cooling is costly to manufacture, difficult to maintain, and described as too complex by Robert Goddard [20, 22, 26]. These technological drawbacks can be overlooked if performance outweighs cost effectiveness, but the private industry does not have such luxuries. If RLVs and cost-effective, reusable liquid engines are to be developed, a different cooling scheme must be introduced to mitigate regenerative cooling, improve engine life cycle, and reduce maintenance costs. A strong candidate for an effective cooling strategy is supersonic film cooling (SSFC) [27].

1.2 Problem Description

Previous cost analyses have suggested fully reusable launch vehicles could provide a means of economically reaching orbit until SSTO vehicles become viable [7-17]. Such a development would prove beneficial to private corporations by reducing manufacturing and overhead costs. In order to develop such a launch vehicle, new engine technology must be developed that is reliable, reusable, and has minimum manufacturing and operational costs. A means of achieving the feasibility of such an engine is the introduction of supersonic film cooling.

In 2001 Volvo Aerospace Corporation demonstrated the viability and cost effectiveness of a SSFC engine. The design reduced overall engine cost by forty percent and was chosen as the primary cooling method for the redesigned Vulcain II nozzle extension in 2005 [28-30]. The technology was later selected by Pratt and Whitney-Rocketdyne to cool the nozzle extension of the J2-X engine under development in 2007 [30]. While the rapid

implementation of SSFC is promising, the cooling method can be further improved to increase cooling effectiveness.



Figure 3: Computer model of the J2-X SSFC engine currently under development [31].

Numerous parametric studies [32-37] have been conducted to investigate the key flow parameters that produce the strongest film protection. The studies have largely concluded that injecting relatively cool, high heat capacity, low viscosity gases at low supersonic speeds provide the best film characteristics. For obvious reasons hydrogen gas is a well suited medium for film injection and tends to limit SSFC to hydrogen fueled engines.

Hydrogen fueled, gas-generator cycle rocket engines are well suited for supersonic film cooling due to the feed system architecture and availability of hydrogen-rich gases exiting the turbomachinery. The hydrogen-rich turbine exhaust gases (TEG) are commonly redirected into a turbine exhaust manifold that injects the TEG along the inner wall of the

nozzle extension. Fig. 4 below outlines a typical gas-generator and turbine exhaust manifold combination.

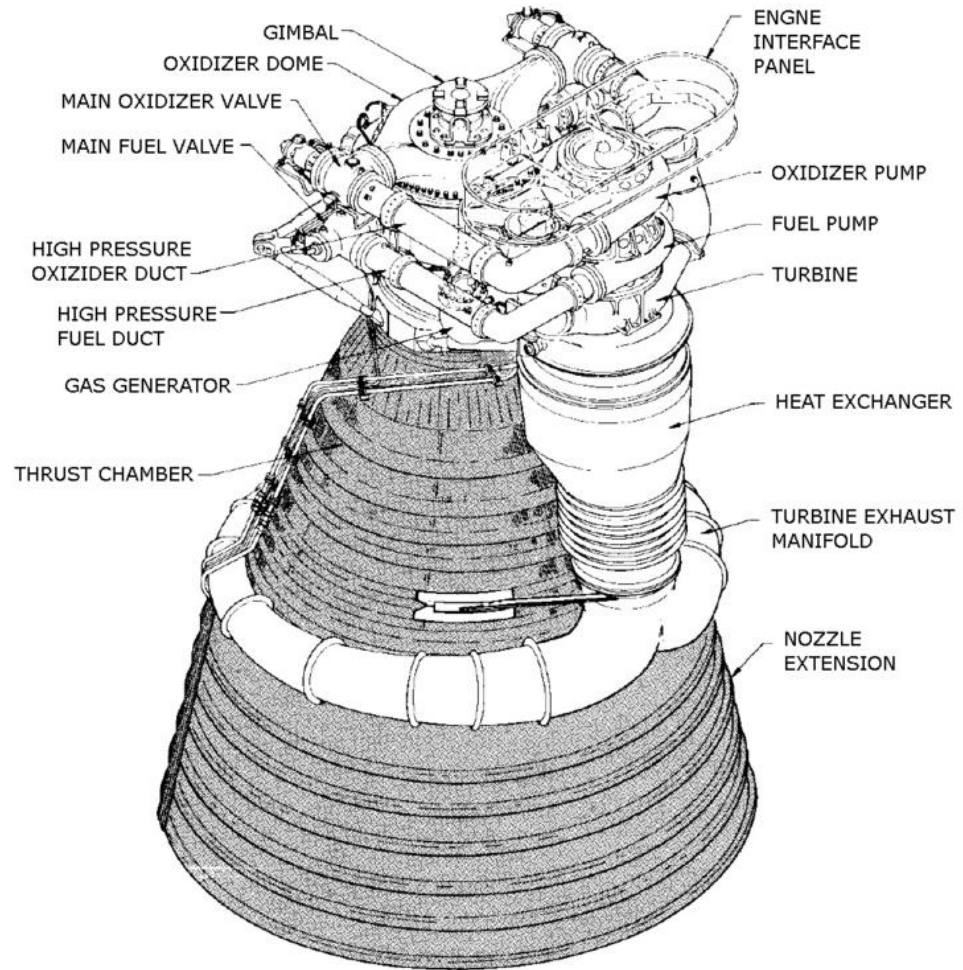


Figure 4: F-1 gas-generator cycle rocket engine [38].

Conventional Western and European gas-generators utilize a fuel-rich combustion process to power the turbomachinery [20]. In the case of a hydrogen fueled rocket engine, the fuel-rich combustion process creates a gas mixture comprised of hydrogen and water-vapor that is ultimately injected along the nozzle wall via a turbine exhaust manifold. While this process has a proven track record of effectively cooling the nozzle, the presence of water-vapor in the TEG negatively affects the cooling efficiency of the film.

1.3 Proposed Cooling Method

Current supersonic film cooled rocket engines inject a mixture of hydrogen and water-vapor along the inner wall of the nozzle extension via an enhanced turbine exhaust manifold. The protective layer of supersonic film produced by this injection process has been proven to be more effective than conventional subsonic film cooling. However, the presence of water-vapor dilutes the specific heat and degrades the capabilities of the film. In essence, current supersonic film cooling (CSSFC) methods work well, but can be improved.

The hydrogen atoms within the TEG hold the key to improving the cooling effectiveness. The proposed cooling method entails extracting and biasing a layer of hydrogen gas along the wall of the nozzle. It is hypothesized that such a biased injection process will increase the cooling effectiveness of the system without the need to carry or use additional gases

1.4 Objective Statement

The objective of this research is to assess the thermal effectiveness of the proposed biased supersonic film cooling method when employed on a hydrogen-fueled, gas-generator cycle rocket engine. The research is meant to serve as an exploratory investigation into the cooling characteristics of biased supersonic film cooling.

Chapter 2: Film Cooling Overview

2.1 Introduction

Film cooling is an active cooling method that has been used extensively in both jet turbine and large-scale rocket engines. The principle behind film cooling is rather straightforward: a cool gas, known as the film, is injected into the boundary layer surrounding a component to separate the surface from a hot gas environment [39]. In jet engines, film cooling is typically employed in the combustion chamber as well as along the turbine blades in an effort to achieve higher engine temperatures without melting critical components. The same technique is applied to the nozzle and combustion chamber of rockets to prevent premature failure.

The combustion chamber liner and nozzle extension are commonly cooled with a subsonic film to prevent failure of the engine during operation. In the case of rocket combustion chamber film cooling, a small percentage of fuel is injected as a film to coat the inner liner. This method, combined with injector and combustion biasing, prevents the combustion chamber from melting [20]. The nozzle extension on a number of engines utilizes subsonic film cooling methods to reduce the thermal loads. As discussed previously, these gases are often provided by the turbomachinery via a turbine exhaust manifold. While the purpose of film cooling is to protect a surface from a hot gas environment, the effectiveness of one system to the next can vary.

The ability of a film to protect a surface is quantified with an efficiency-like definition known as the film cooling effectiveness. The following expressions mathematically define the film cooling effectiveness for both subsonic and supersonic film injection [40, 41].

$$\eta_{sub, film} = \frac{T_w - T_\infty}{T_i - T_\infty} \quad (1)$$

$$\eta_{super, film} = \frac{T_{rw} - T_{r\infty}}{T_{ri} - T_{r\infty}} \quad (2)$$

The expressions above relate the component surface temperature, denoted by a subscript w , to the temperature of the edge of the viscous sub-layer which is denoted with a subscript i . It should be mentioned that the supersonic relation requires the use of the recovery temperature which is a means of accounting for the dissipative effects within the boundary layer via a correction factor based on the Prandtl number. The following expressions outline the recovery temperature calculations.

$$T_r = T_\infty \left(1 + r \frac{\gamma - 1}{2} M^2 \right) \quad (3)$$

$$r_{lam} = \sqrt{Pr} \text{ or } r_{turb} = \sqrt[3]{Pr} \quad (4,5)$$

It has been shown that film cooling effectiveness is influenced by the convective Mach number, turbulence effects, velocity ratio, temperature ratio, blowing ratio, density ratio, and compressibility effects that arise at high speeds [32-37, 40, 41]. In general, these effects can be lumped together in the following form [42].

$$\eta_{film} = C_1 Re_s^{0.2} \left(\frac{x}{\beta s} \right)^{-0.8} \quad (6)$$

The above expression relates the film cooling effectiveness, η_{film} , to the injection slot Reynolds number, Re_s , linear downstream distance, x , slot height, s , and blowing ratio, β . The leading coefficient, C_1 , is an appropriate empirical value or function that strongly influences the correlation. While this expression is helpful, the empirical nature of the leading coefficient limits the accuracy of the correlation to specific flow regimes.

Since the late 1950s there has been a concerted effort on the part of researchers and experimentalists to develop an all-encompassing correlation between flow parameters and

film cooling effectiveness. Such an expression would allow for accurate film cooling predictions for a wide range of parameters. Unfortunately, such an expression has yet to be developed due to the complexity of turbulent mixing flows [32]. A brief summary of previous work since the early 1950s has been presented in section 2.3. Although film cooling is rather diverse in both application and execution, the present thesis will focus exclusively on supersonic film cooling injected through a rearward-facing slot.

2.2 Film Cooling Classification

Film cooling can be classified in a number of different ways based on the manner in which the film is injected. The classification methods focus on the geometry of the injection site, velocity of the injection, as well as the ratio of film parameters to core-flow values. The following sub-sections outline a number of important film categories that are commonly found in industry.

2.2.1 Discrete Injection

Discrete film injection utilizes a number of small holes surrounding a component to shield the surface from a hot gas environment. The small holes are desirable when structural and manufacturing constraints are present. In the aerospace industry, discrete film injection is commonly used in the hot-section components of air-breathing engines.

In a typical jet engine, film gases are injected via discrete holes in order to blanket a region with relatively cool air. For example, turbine vanes inject air provided by the high pressure compressor through small holes covering the surface of the blade [43]. Fig. 5 on the following page provides a cross section cut of an advanced turbine vane that incorporates discrete film cooling.

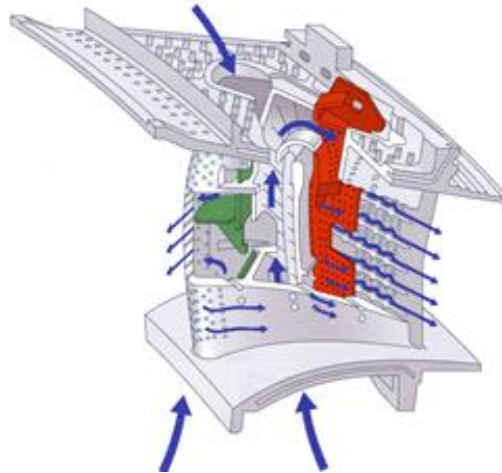


Figure 5: Discrete film injection on an advanced turbine vane [44].

As one can observe from Fig. 5 above, cool gases are forced into the top and bottom of the hollow turbine vane. The cavity within the vane allows the gases to cool the inner surfaces of the component before being injected into the boundary layer via discrete holes. The film injection surrounds the vane with a cool boundary layer which prevents premature failure of the turbine assembly.

2.2.2 Slot Injection

In a number of applications it becomes beneficial to inject film in a sheet or curtain. Discrete film injection, while a proven cooling method, cannot blanket an entire region with a uniform film. To achieve a blanketing effect, the film gases must be injected through a slot upwind of the region requiring protection [45]. Rocket engine nozzle extensions commonly employ the use of slot injection to protect the nozzle wall. An image of a gas manifold injector has been provided in Fig. 6.

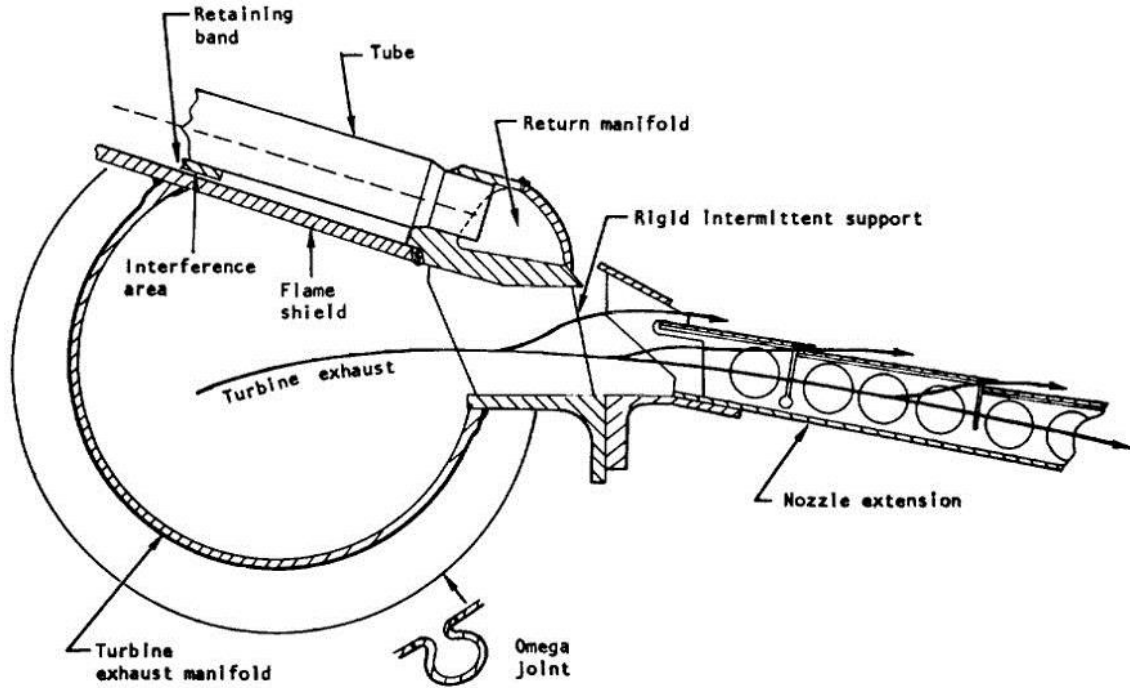


Figure 6: F-1 engine turbine exhaust manifold and nozzle extension film injection [46].

Gases injected through a slot can protect a far larger region than discrete injection sites. However, the presence of a large transverse slot can present structural and manufacturing issues for small, highly loaded components such as turbine blades [47]. For these reasons, slot injection has largely been used for cooling non-rotating components such as combustion chamber liners, nozzle extensions, and advanced nosecones.

2.2.3 Subsonic Injection

As the name implies, subsonic film injection utilizes gases that are injected at low to moderate Mach numbers. Subsonic injection is ubiquitous within many industries due to its ease of implementation. In the aerospace industry, subsonic film injection is common in both air-breathing engines as well as conventional rocket engines.

2.2.4 Supersonic Injection

Similar to other forms of film cooling, supersonic film cooling leverages high velocity and relatively cool gases to shield a surface. Supersonic film cooling is not as common as subsonic film injection due to the additional measures that must be undertaken to accelerate the secondary flow to supersonic velocities. For this reason, supersonic film cooling has not been widely adopted by the aerospace industry. However, supersonic film cooling offers an advantage over other film cooling techniques with respect to shear layer growth reduction.

The compressible shear layer growth rate is a measure of the mixing between two flows due to shearing and turbulence effects. In other words, the shear growth rate is directly proportional to the mixing region thickness, which is highlighted by the swirl-like structures found in Fig. 7 on the following page. By nature, supersonic flows are characterized by relatively small shear growth rates which increase the overall film cooling effectiveness by mitigating the premature break-up of film [32]. In addition to reducing the shear layer growth rate, supersonic injection techniques better match the velocities experienced in the nozzle extension of a rocket.

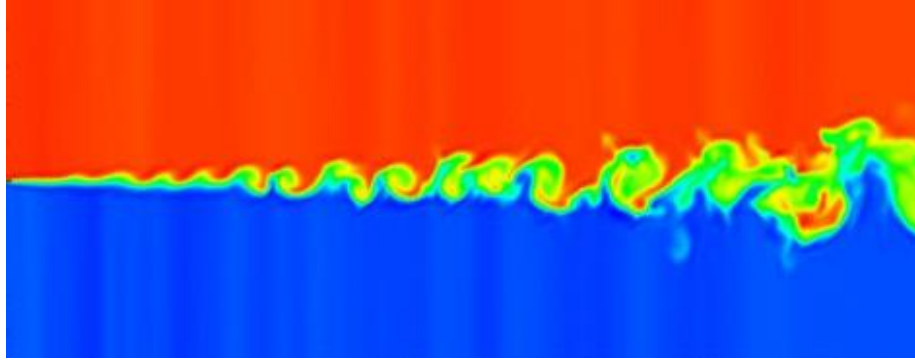


Figure 7: Turbulent mixing in binary layer [48].

A film's capacity to shield a component is largely a function of the film's ability to remain adhered to the component's surface and the properties of the film. If the film is subjected to a stream of much greater velocity, the film will have a tendency to break up due to entrainment [49]. This scenario is common in the nozzle extension of a rocket engine where Mach numbers are generally several times greater than the speed of sound. Injecting a subsonic film into such an environment causes the film to rapidly break up. These effects can be mitigated by injecting the film at a velocity of the same order of magnitude as the mainstream. Therefore, a component subjected to a supersonic flow can be better protected with the application of a supersonic film.

2.2.5 Core-Driven

Film cooling applied to a stream of higher velocity is known as a core-driven flow. In this particular scenario the film gas is entrained by the mainstream and is accelerated to a higher velocity. The difference in velocities gives rise to a shearing effect as the gases meet, which causes abrupt mixing that breaks up and dilutes the film [49]. The resulting effect is premature loss of film cooling effectiveness and increased component surface temperatures. This issue can be mitigated with moderate core-to-film velocity ratios.

2.2.6 Wall-Jet

Wall-jets form when a secondary flow is injected along a wall at velocities greater than the mainstream. The increased velocity gives rise to greater convective heat transfer coefficients and thus alters the heat flux of the surface. While a wall-jet film improves the convective heat transfer of the surface, excessive film velocity can cause shearing between the flows and potential boundary layer heating. Wall-jets must therefore enhance the heat transfer characteristics while minimizing the mixing and boundary layer heating effects.

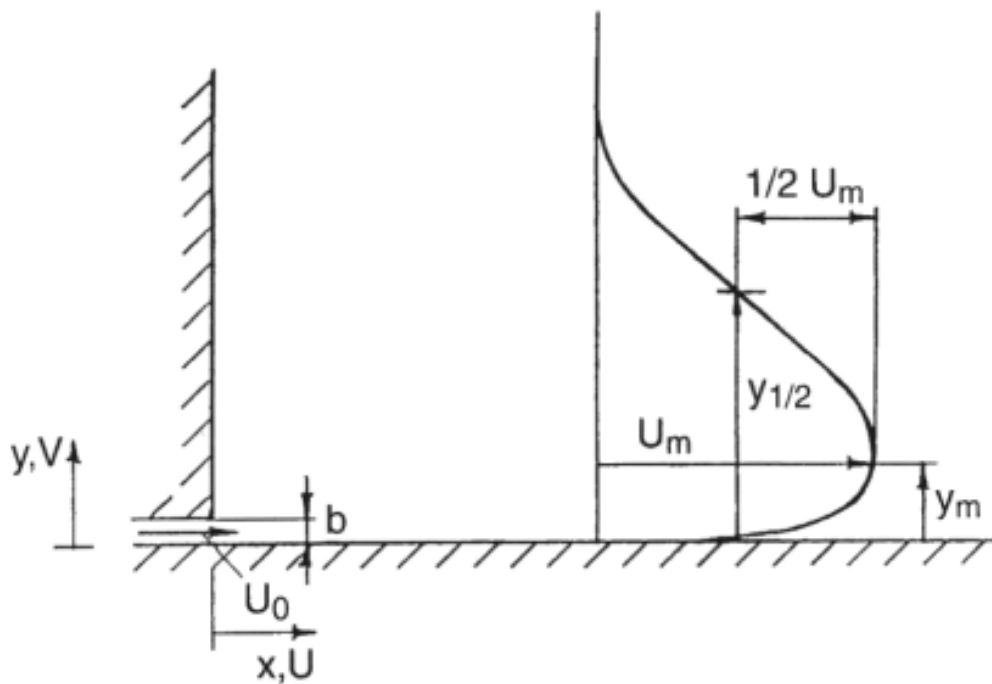


Figure 8: Wall-Jet velocity profile [50].

2.3 Previous Work

Film cooling has been heavily investigated over the past fifty years due to its use as a primary thermal management technique in the aerospace industry [39, 51, 52]. The investigations carried out during that time period have taken the form of analytical work, experimental work, and more recently numerical work. These efforts have attempted to generate key governing parameters effecting film cooling effectiveness, explore correlations between flow parameters, and produce useful parametric experimental data. The following subsections outline the major steps undertaken in the field of film cooling.

2.3.1 Analytical Work

The analytical work applied to film cooling has largely focused on boundary layer or wall-jet analysis [32]. While numerous analytical correlations have been produced since the late 1950s, many are only accurate under certain circumstances or make unreasonable assumptions. For example, in 1959 Hatch and Papell produced correlations between flow parameters and film cooling effectiveness under the assumption that the film does not mix with the mainstream. As one can imagine such an assumption did not produce accurate results. To address this issue, Papell continued the work by refining the existing correlations throughout the early 1960s [53,54].

During the same time period, Hartnett was conducting similar film cooling analysis through an analytical analysis of the film boundary layer. The resulting correlations utilized slot injection parameters and Reynolds number to approximate the film cooling effectiveness as a function of linear distance. The correlations agreed well with subsonic experimental data, but proved inaccurate near the film injection region [55]. The inaccuracy near the film injection region was investigated throughout the 1970s and was addressed in 1986 by Simon [56].

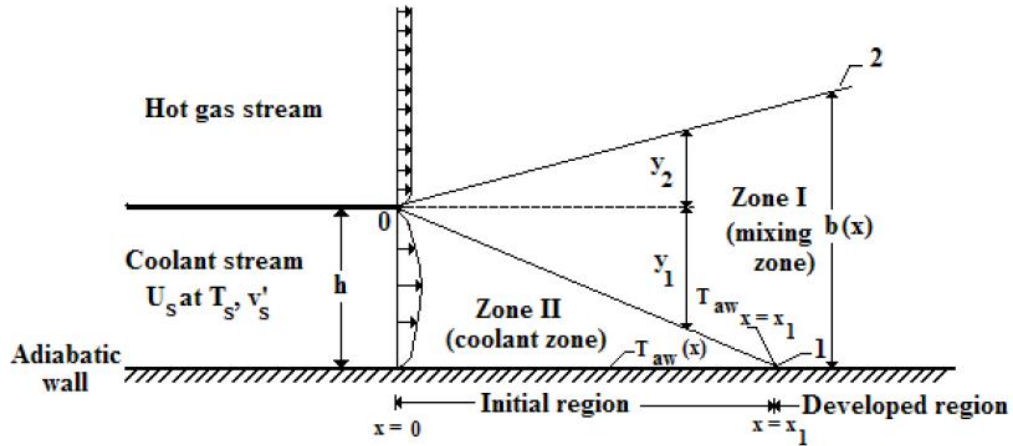


Figure 9: 2D film cooling schematic utilized by Simon to predict film cooling effectiveness [32].

In 1986 Simon realized that the region near the film injection site was characterized by relatively low mixing. Simon modeled the turbulence effects in a piecewise manner in order to account for the unique flow properties adjacent to and downstream from the injection region [56]. His model, which is only accurate for incompressible flows, was found to agree with experimental data within $\pm 4\%$ for turbulence intensities less than 24%. Analytical work focused on compressibility effects were under investigation throughout the 1960s as well.

Analytical compressible film models tend to focus on entrainment and mixing layer growth rates [32]. In 1963 Channapragada developed a compressible jet formulation for mixing flow analysis. While Channapragada's work focused on a general mixing analysis, the correlations agreed well with film cooling experimental data below Mach 2 [57]. A number of other researchers who conducted both analytical and experimental work relating to film cooling compressibility effects have presented mixed conclusions.

Research conducted by Volchkov et al., and Repukhov have indicated that compressibility does not greatly effect film cooling effectiveness [58,59]. Conversely, Pedersen et al. and Hansmann et al. have conducted both analytical and experimental work

that suggests compressibility effects do affect film cooling characteristics [60,61]. Similar disagreements with respect to density, pressure, and thermal gradients have surfaced in literature as well [32]. As mentioned previously, these dissimilarities arise from the inherent complexity of mixing layer flows, turbulence, and, compressibility, and shear layers.

2.3.2 Experimental Work

In the late-1950s, Papell et. al. performed a series of subsonic film cooling experiments to study slot film injection methods [62]. This work was shortly followed by discrete film injection experiments conducted by Hartnett et al. which focused on temperature and boundary layer profile mapping [63]. Similar experimentation was conducted throughout the 1960s in which the majority of work focused on the geometric injection parameters such as slot and hole shape, orientation, and size. Throughout the 1970s and early 1980s, film cooling research began to focus on turbulent effects. One of the earliest film cooling experiments focused on turbulence was conducted by Juhasz et. al.

Juhasz et. al. conducted a number of experimental trials focused on studying film cooling effectiveness in combustion chamber liners. The results indicated that turbulence played a significant role with regards to film stability and mixing characteristics [64]. This work was further verified in 1991 when Lebedev et. al. performed a series of turbulent film cooling experiments [65]. There are numerous experimental results that are readily available to the public, but the experimental data of most importance to this work was performed in 1994 by Juhany et. al [66]. The details of the experiment are detailed in section 4.2.1.

2.3.3 Numerical Work

In the mid-1960s Lessen et. al. performed a series of numerical studies to investigate compressible free shear-layer flows [67]. The results of these experiments concluded that

compressibility effects were beneficial to film cooling effectiveness due to the reduced mixing layer growth rate. Apart from the work conducted by Lessen et. al, the bulk of the film cooling numerical work was conducted in the late 1980s and was a strong area of research in the mid-1990s.

In 1996 Vreman et al. used numerical techniques to investigate compressible shear layer growth as well as mixing phenomena. Compressibility effects and mixing characteristics at moderate supersonic velocities were further explored by Chalot et. al, Sandham et. al, Sarkar et. al, and throughout the 1990s [68-70].

2.3.4 Film Cooling Reviews

Since the 1960s film cooling has been the focus of numerous papers, dissertations, journal papers, and research. The investigations discussed in sections 2.3.1-2.3.3 provide a small fraction of the film cooling literature available. However, there are a number of reviews that explore the field of film cooling in depth. One of the earliest and most revered film cooling reviews was authored by Goldstein in the early 1970s which focuses on the research conducted prior to 1970 [39]. Other notable film cooling reviews have been assembled by Birch et al. and Vreman [51, 52].

Chapter 3: Methodology

3.1 Introduction

In the past, NASA, DARPA, and the vast majority of well-organized research institutes have established a series of phases that must be undertaken in a chronological manner that, upon completion, validate or prove a specific concept. Proving the effectiveness of the proposed biased supersonic film cooling (BSSFC) method required similar phases to be completed in a methodical fashion. Industry standards outlined in the third chapter of the *Military Project Management Handbook* were used as an inspiration for the organization of research provided throughout the following sections [71].

3.2 Phase I: Preliminary Steps

The first phase of research consisted of a number of smaller steps that established the best film cooling modeling techniques, selected an appropriate benchmark engine platform for analysis, and define the parameters of both the conventional and biased film cooling methods. The objective of the first phase of research was to develop the techniques and gather the information necessary to simulate both the conventional and biased supersonic film cooling methods. Phase I can be thought of as the foundation of the research.

3.3 Phase II: Computational Gas Modeling

Phase II of the research focused on creating a computational gas model that reproduced the gas characteristics of the core-flow and film injection gases to be used in the numerical models. The goal of the second phase was to develop a modeling strategy to simulate the gas characteristics within the engine and of the film gases without exorbitant computational requirements. To accomplish this task, a series of non-reacting, temperature-

dependent gas mixtures were developed with the aid of information supplied in NASA TM 4513 and NASA TM 4647. Without the completion of Phase II, the gas modeling of the film cooling methods could not be performed in a time efficient and accurate manner.

3.4 Phase III: Biased Flat Plate Models

The gas mixtures, techniques, and flat plate models developed in Phase I and Phase II were used to verify the biased supersonic film cooling concept. The conventional film cooling method of injecting a mixture of hydrogen and water-vapor was applied to ten flat plates with slot-averaged Mach numbers ranging from 1.1 to 3.0. The same ten models were then subjected to the biased supersonic film cooling method in which a stream of hydrogen half the thickness of the slot height was injected along the wall. In order to ensure that the trials were comparable, the slot-averaged blowing ratio was matched for each trial pair and the static injection temperature and pressure were maintained for all trials. The objective of the third research phase was to ensure that the BSSFC method worked on a simple flat plate model prior to applying the technique to a full-scale engine.

3.5 Phase IV: Implementation

Phase IV utilized the knowledge gained from the previous steps to test the biased supersonic film cooling technique on four film cooled nozzles. Each film cooled nozzle was geometrically identical apart from the location of the injection slot. Altering the film injection location ensured that the BSSFC method could be parametrically tested as a function of location. Aside from using four different models to test the effect of slot location, the verification method of Phase IV closely matched that of Phase III.

Similar to the biased flat plate analysis, a series of ten conventional SSFC trials with slot Mach numbers ranging from 1.1 to 3.0 were simulated on each nozzle. The same models

were then altered to inject a hydrogen film half the thickness of the slot height along the nozzle wall. The hot-side film stream was comprised of excess hydrogen gas and water-vapor. Again, the blowing ratio for each trial pair was matched and the injection static temperature and pressure were held constant. These efforts produced eighty film cooling models that parametrically tested slot Mach number, injection location, and cooling strategy to access the film cooling effectiveness of the BSSFC method.

Chapter 4: Phase I: Preliminary Steps

4.1 Introduction

Prior to beginning the film cooling numerical analysis, a number of key preliminary steps were undertaken to obtain insight and information regarding film cooling, review film cooling experiments, and select an existing engine platform for modification.

4.2 Flat Plate Analysis

From an academic standpoint, the simplest case of a phenomenon offers a great deal of insight. In the case of film-cooling, the flat plate model is the simplest and provides a test bench to conduct experiments with the fewest number of variables. These characteristics have made flat plate models appealing to experimentalists and analysts alike. The flat plate model was therefore a logical place to begin an investigation and validate model parameters.

4.2.1 CAL-Tech Experiments

A number of existing flat plate experiments were investigated and considered for numerical validation via a computational model. Existing experimental data was of interest due to the ability to correlate numerical results with real-world tests to evaluate model accuracy. Upon investigating numerous experimental tests, a flat plate experiment conducted by CAL-Tech in 1994 was selected due to the quality of the experiment, well documented parameters, and availability of experimental data [66].

In 1994, Juhany et. al. conducted a series of experiments in the CAL-Tech Graduate Aeronautical Laboratory (GALCIT) using the continuous supersonic wind tunnel [66]. The experiment used a half-nozzle plane to accelerate air to a Mach of 2.44 ± 0.02 . A secondary stream of precooled air or helium, depending on the trial, was injected through a slot along an instrumented Hastelloy-X plate. The sensors embedded in the plate recorded relevant

temperature data which was ultimately compared to results obtained by Goldstein et. al., Cary and Hefner, and Rousar and Ewen [72-75]. A schematic of the experimental set-up has been provided in Fig. 10 below.

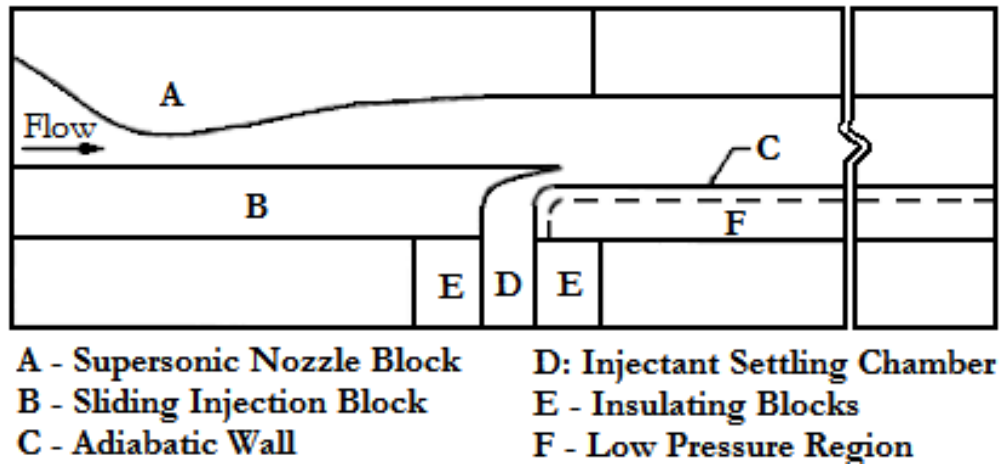


Figure 10: CAL-Tech experimental set-up [65].

The data obtained from the CAL-Tech film cooling experiments was provided via a semi-log plot in the publication outlining the team’s findings. To investigate the CAL-Tech experimental results in detail, a graphical digitization software known as ‘GetData’ was used to extract the film cooling information from the documentation [76]. The Fig. 11 on the following page outlines the experimental results extracted from the three CAL-Tech pre-cooled air trials.

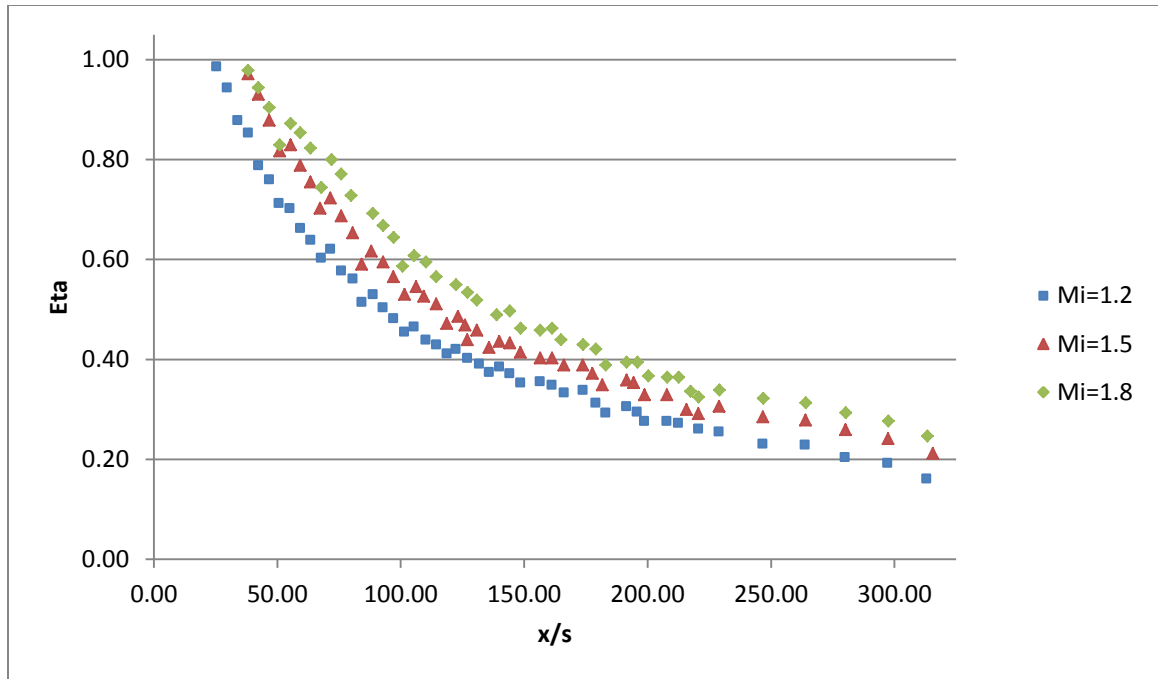


Figure 11: CAL-Tech experimental film cooling values extracted from documentation [65].

4.2.2 CFD Flat Plate Modeling

Developing computational models that match experimental data is a step that must be under taken in order to ensure the validity of future models. For the purposes of this work, a series of two-dimensional, planar models were generated to mimic the characteristics of the CAL-Tech experiment. The congruency of the model parameters was ensured by matching the geometric and boundary condition parameters with the CAL-Tech documentation. Conversely, the geometry was altered slightly to simplify the numerical model. Fig. 12 below outlines the geometry used to approximate the CAL-Tech experimental set-up.

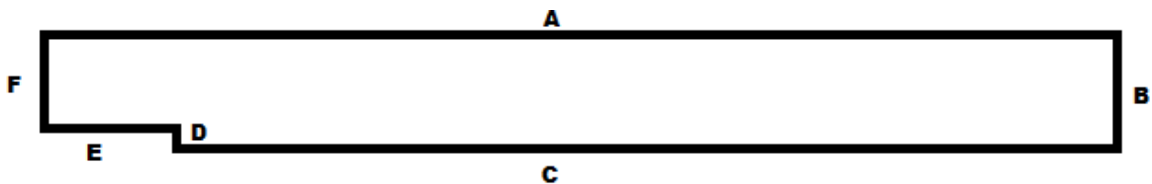


Figure 12: 2-D flat-plate model configuration (side-view).

The geometry presented in Fig. 12 on the previous page is slightly different from the experimental set-up in two distinct ways. To simplify the model geometry, the slot inlet was reduced from a beveled-wedge to a vertical face. The injection parameters were adjusted to match this alteration. The second difference between the model and experiment manifests itself in the total length of the test section.

The length of the test section was increased for the numerical simulation in order to avoid possible exit-plane boundary condition interactions with the area of interest. The experimental documentation outlined the majority of the flow parameters well, but did not provide a great deal of information concerning the exit geometry and pressure. The conditions at the exit-plane were therefore approximated using the ambient conditions provided in the documentation. The potential differences in exit boundary conditions can distort the temperature and velocity profiles near the exit plane of the test section. By lengthening the model, the influence of the exit plane was mitigated. The remaining boundary conditions were coordinated with the experimental set-up and have been listed in Table 1 below.

Table 1: Flat-plate model boundary conditions (Sections correspond to Fig. 12)

Section	Name	Pressure [Pa]	Temperature [K]	Velocity [m/s]
A	Top Wall	N/a	Adiabatic	No Slip
B	Outlet Plane	90,000	N/a	N/a
C	Flat Plate	N/a	Adiabatic	No Slip
D	Injection Inlet (Slot)	98,285	295	840.05
E	Step Wall	N/a	Adiabatic	No Slip
F	Core-Flow Inlet	80,525	215	352.7

4.2.3 Turbulence Model Selection

Selecting an appropriate turbulence model is vital due to the potential impact on the boundary layer, shear layer, and mixing sub-layer accuracy. To ensure the validity of the numerical simulations, a number of common turbulence models were investigated and compared to the experimental results. The investigated turbulence models have been provided with their respective descriptions in Table 2 below.

Table 2: Investigated turbulence model descriptions [77].

Model	Description
K-Epsilon (RNG)	Statistical/ analytical turbulence model following the renormalization group (RNG) methodology. Similar to the standard $k - \epsilon$ model with additional terms to account for swirl and rapidly strained fluid elements.
K-Epsilon (Standard)	Model that independently solves the turbulent viscosity and length scales for the flow. Typically used for general engineering purposes and flow analysis.
K-Omega SST	Blends the near-wall accuracy of the standard $k - \omega$ model with the free stream effectiveness of the $k - \epsilon$ model via a wall scaling function.
K-Omega (Standard)	Modified version of the Wilcox $k - \omega$ model with additional correction factors for compressibility, Reynolds number, and shearing effects.
Reynold Shear Stress	Relatively intricate model that solves the dissipative rate and transport Reynolds shear stresses. Useful when predicting ‘streamline curvature, swirl, rotation and rapid strain rate changes’. Incorrect pressure-strain and dissipation-rate terms can lead to large inaccuracies.
Spalart Allmaras	One equation model used to predict the turbulent viscosity of wall-bounded flows.

The turbulence models were individually enabled on a series of flat plate models with a film injection Mach of 1.2 in an effort to reproduce the CAL-Tech experimental results. The film cooling effectiveness values obtained from these numerical investigations were compared to the experimental results extracted from the Cal-Tech documentation described in section 4.2.1. Fig 13 and Fig. 14 have been provided on the following page to illustrate the film cooling effectiveness comparisons.

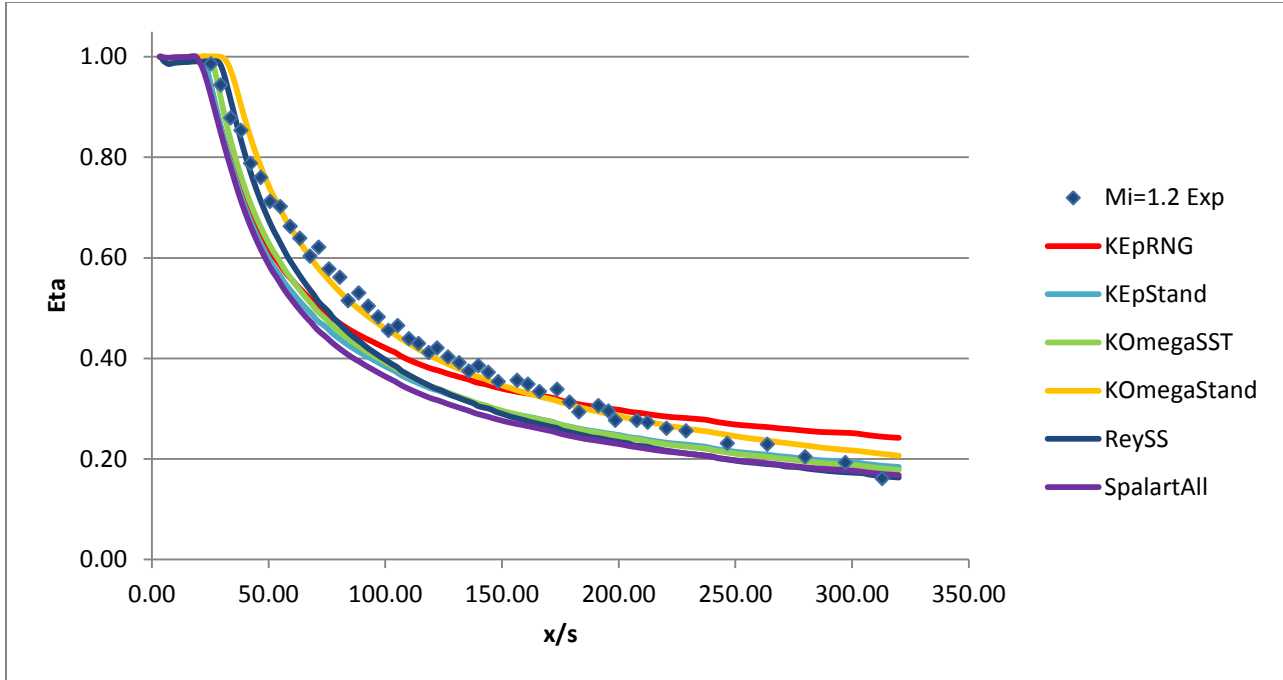


Figure 13: Laminar film cooling effectiveness values for various turbulence models.

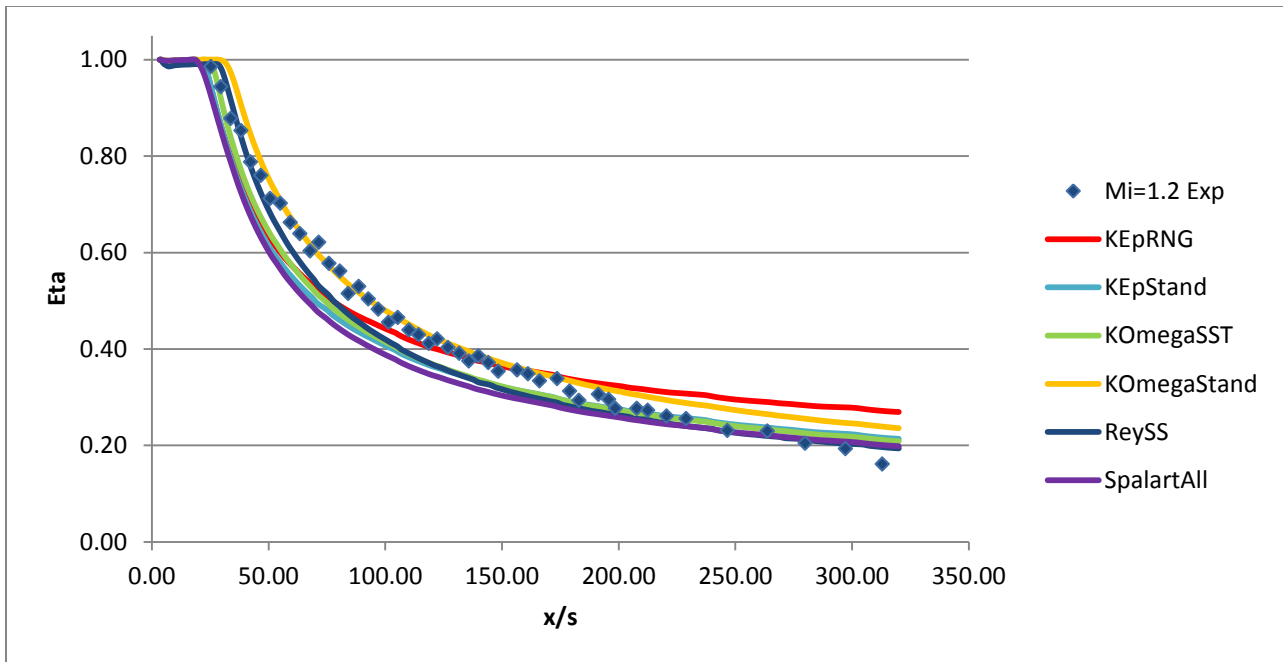


Figure 14: Turbulent film cooling effectiveness values for various turbulence models.

The film cooling effectiveness plots provided in the previous figures indicate that the turbulence models follow the same trends, but do not produce the same results. In general

terms the turbulence models produce reasonable results, but the standard K-Omega turbulence model with an enabled compressible correction factor produced the best agreement with the CAL-Tech experimental data. It was therefore decided to utilize the standard K-Omega turbulence model for all film cooling simulations.

4.3 Engine Selection

During the initial stages of the research, it became evident that modifying an existing engine platform with the proposed biased supersonic film cooling was desirable. Utilizing an existing SSFC engine provides both baseline cooling characteristics as well as numerous engine parameters such as combustion chamber characteristics, approximate mass flow rates, and nozzle geometry. However, the relatively recent introduction of supersonic film cooling limited the number of existing engines to a small quantity.

The small number of SSFC was further reduced by eliminating engines currently under development. This included the upper stage J2-X engine being tested at NASA's Marshal Space-Flight Center [30]. Of the remaining SSFC engines, the Vulcain II engine produced by Snecma and Astrium was the most appropriate.

The Vulcain family of engines designed by Snecma motors has been under development since the late 1980s as a part of the Ariane-5 launch vehicle program [78]. Apart from a number of difficulties experienced with the introduction of the Ariane-5 in the mid-1990s and the ill-fated flight 501, the Vulcain family of engines has had a proven track record of reliability [79]. This reliability, coupled with the vast amount of documentation outlining numerous engine parameters, made the Vulcain II the best option to test the biased supersonic film cooling strategy.



Figure 15: Vulcain II engine developed by Snecma Motors of Safran Defense Group [80].

4.3.1 Vulcain II Parameters

Snecma Motors of France, the primary contractor for the Vulcain II engine, has made a series of documents outlining the engine’s capabilities and characteristics publically available [81-84]. Additionally, a series of tests carried out at the Institute of Space Propulsion at the German Aerospace Center (DLR) have also been made publically available [85]. The documentation outline many engine parameters including area ratios, mass flow rates, fuel to oxidizer ratios, and other important factors. A summarized account of the Vulcain II engine parameters has been provided in Tables 2-5 below and on the following page.

Table 3: Vulcain II combustion chamber characteristics [81].

Parameter	Value
Fuel	Hydrogen
Oxidizer	LOx
Fuel/ Oxidizer Ratio	6.74
Fuel Mass Flow Rate [kg/s]	40.4
Oxidizer Flow Rate [kg/s]	272.6
Pressure [Bar]	117.3
Temperature [K]	3,525

Table 4: Vulcain II nozzle characteristics [81].

Parameter	Value
Area Ratio	58.2
Exit Diameter [m]	2.094
Throat Diameter [m]	0.2745
Axial Throat to Exit Distance [m]	4.49

Table 5: Vulcain II gas-generator characteristics [81].

Parameter	Value
Fuel	Hydrogen
Oxidizer	LOx
Fuel/ Oxidizer	0.9
Fuel Mass Flow Rate [kg/s]	4.6
Oxidizer Mass Flow Rate [kg/s]	5.1
Internal Temperature [K]	875
Turbine Exit Pressure [Bar]	4.0-7.0

Table 6: Vulcain II engine characteristics [81].

Parameter	Value
Isp (s)	429
Vacuum Thrust [Kn]	1,359
Height [m]	3.44

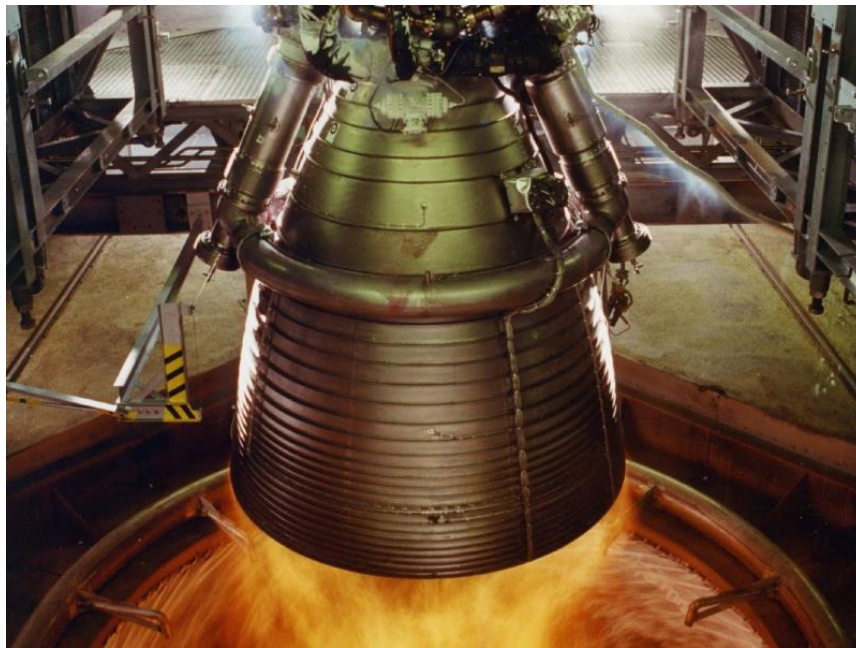


Figure 16: Vulcain II hot-fire test [81].

4.4 Nozzle Contour

One of the goals of Phase I was to obtain, calculate, or approximate the inner wall geometry of the Vulcain II engine. The geometry of the engine was of particular importance due to the need to supply the commercial meshing software with contour data for meshing purposes. Attempts to locate accurate engine wall coordinates were unsuccessful, and the use of method of characteristic codes proved ineffective. Therefore, an image processing technique was developed to approximate the wall contour of the Vulcain II engine. The following subsections outline the steps undertaken to generate the engine geometry.

4.4.1 Phase I: Nozzle Extension

The geometry of the nozzle extension was approximated using a number of techniques that were combined in order to produce the final dimensions. The nozzle geometry was originally approximated with the aid of an open-source method of characteristics (MOC) code that was developed by a Ph.D candidate by the name of Britton Olson at Stanford University [86]. However, it was discovered that the MOC relied on ‘frozen-equilibrium’ calculations, which assume constant gas properties, to approximate the nozzle wall which resulted in an inadequate nozzle contour. Fig. 17 on the following page highlights the differences between the MOC nozzle contour and the actual engine geometry.

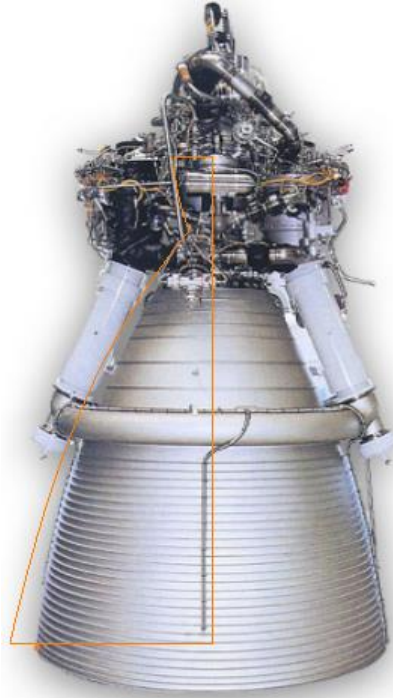


Figure 17: Scaled Vulcain II image overlaid with a MOC nozzle contour (orange) [87].

The orange contour provided in Fig. 17 above was created by truncating the nozzle geometry generated by the MOC code. The wall divergence angle and exit area were found to be inaccurate when compared to Vulcain II. Additional open-source MOC codes performed in a similar fashion. Therefore, an image processing method was chosen to approximate the engine contour.

A large number of images of the Vulcain II nozzle extension were extracted from Astrium and Snecma documentation as well as from various sources online [88-95]. These images were compiled into an image database and prioritized based on the sharpness and orthogonality of the image. The images were edited in such a manner to set the engines on a single-tone background. Once the files were edited, the images were analyzed via Matlab's image processing functions and imported CATIA's immersive sketch workbench. These

efforts produced a series of points that followed the contour of the nozzle extension. A truncated list of the nozzle points has been provided in the appendix.

4.4.2 Phase II: Combustion Chamber

The combustion chamber geometry was handled in a slightly different manner than the nozzle extension. A number of combustion chamber characteristics and dimensions were found via public documentation provided by Astrium and the Safran defense contractor [81-85]. This information was used to generate a rough combustion chamber design that was later refined with additional information obtained from post-process results produced by Astrium of the actual Vulcain II thrust chamber [96]. The last phase that was conducted to generate the engine geometry was the throat region of the engine.

4.4.3 Phase III: Throat Region

The geometry near the throat of the engine was particularly important as a smooth throat contour is essential to engine performance and flow health [97]. To approximate the throat geometry, a number of images were obtained of various images of the Vulcain II thrust chamber without the nozzle extension or exterior hardware. The images were loaded into CATIA's immersive sketch workbench and scaled to ensure the throat diameter measurements were correct. With the images correctly scaled and orthogonal, a series of splines were overlaid to approximate the wall contour. A sample image of the combustion chamber used for the immersive sketch has been provided in Fig. 18 on the following page.

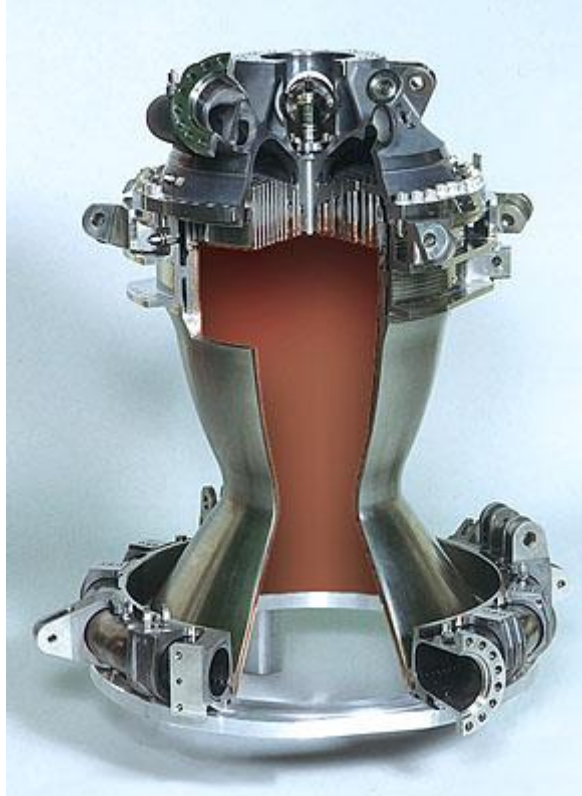


Figure 18: Vulcain II thrust chamber and throat region used for immersive sketching [98].

The throat region of the engine also served as a means to blend the combustion chamber and nozzle extension together. To achieve this blending effect, the splines used to approximate the throat region were adjusted as needed until the engine wall contours flowed together into one contour. The blended contours were ultimately curve-fit in a piece-wise fashion with high-order polynomials.

4.4.4 'Default' Engine Geometry

To illustrate the accuracy of the image-processing method, a scaled image of the Vulcain II engine was overlaid with the geometry information obtained from sections 4.4.1-4.4.3. The contour aft of the turbine exhaust manifold has a slightly smaller diameter than that of the actual image. This was done in order to insert the film injection in a more accurate manner which is discussed in section 7.2.



Figure 19: Scaled Vulcain II image overlaid with the image-processing contour (orange) [87].

The geometry highlighted in orange in Fig. 19 above represents what will be referred to as the ‘Default Engine Geometry’ which does not include a film injection slot along the nozzle wall. This geometry was utilized to generate numerical models for thermal predictions without the use of film cooling and to serve as a coordinate database for later manipulation. A series of engine contour coordinates have been tabulated and provided in the appendix. Fig. 20 on the following page has also been provided to demonstrate the size and shape of the engine contour.

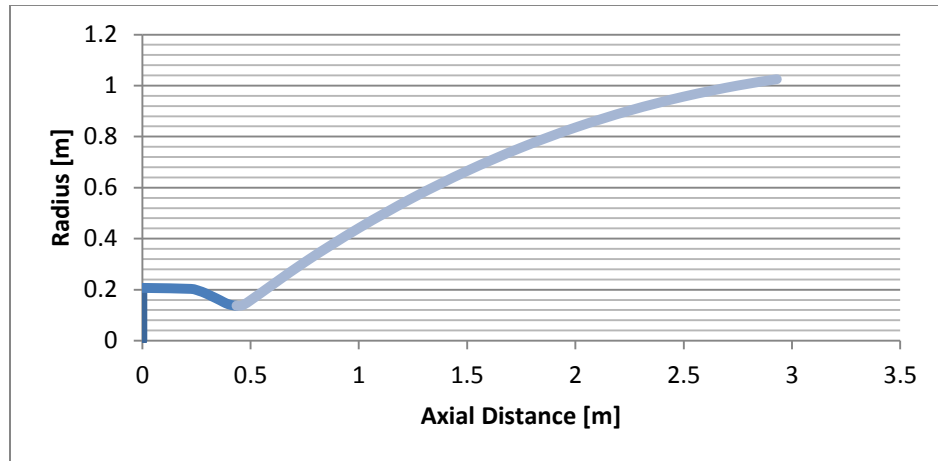


Figure 20: Vulcain II approximate geometry.

The geometry outlined in Fig. 20 above was used to generate a database of points to define the ‘default’ nozzle contour. The database was imported into a Matlab routine that generated four different film cooled nozzles with various slot injection locations. Section 7.2 highlights the manner in which the rearward facing slots were inserted along the nozzle wall.

4.5 Conventional and Biased Supersonic Film Cooling Definitions

Perhaps one of the most important steps undertaken in Phase I of the research was the definition of the cooling methods to be tested and the trial parameters. This step was of importance due to the vast array of film cooling classifications and parameters available. In general terms, both the conventional and biased film cooling methods mimicked the injection characteristics of the Vulcain II engine. However, there were a number of alterations made to ensure the focus of the thesis remained centered on film cooling.

The vast majority of rocket engines combine several cooling methods to ensure the engine remains within the allowable temperature range. In the case of the Vulcain II engine, the supersonic film cooling is combined with a dump cooling scheme supplied with additional hydrogen from the regenerative cooling lines. Fig. 21 on the following page provides a simplified schematic of the Vulcain II cooling system.

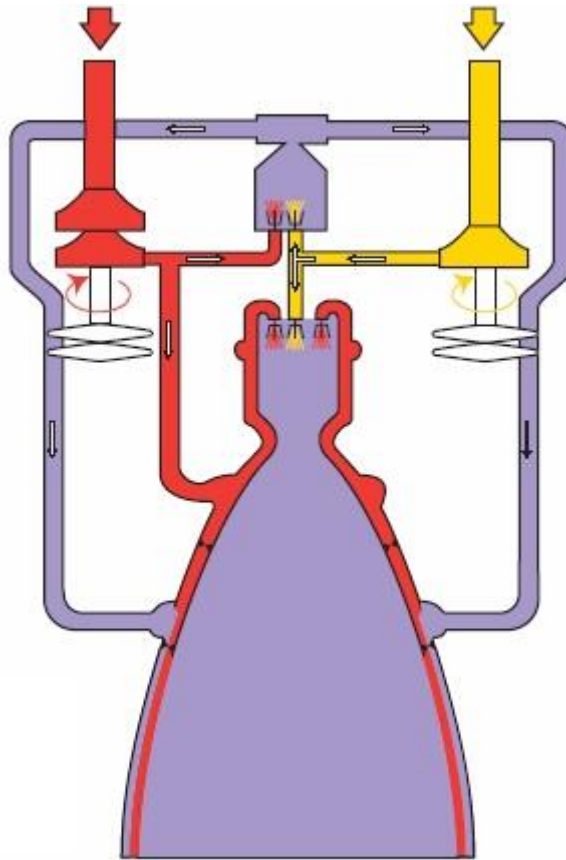


Figure 21: Simplified Vulcain II cooling system schematic [85].

Fig. 21 above details the general flow path the fuel, oxidizer, TEG, and core-flow within the engine. The hydrogen fuel, highlighted in red, is circulated throughout the engine in an effort to regeneratively cool the combustion chamber and throat region of the engine. A percentage of hydrogen is also expelled alongside the supersonic gases provided by the turbine exhaust manifold. While this combination works well on the actual engine, dump cooling is beyond the scope of the present research and was therefore neglected in the numerical simulations.

In an effort to focus on supersonic film cooling, the excess hydrogen from the regenerative cooling system dumped alongside the film gases was neglected. This decision ensured that the film cooling effectiveness values were not subject to the influence of hydrogen entrainment. The flow injection simplification also led to the definition of what

has been deemed the conventional and biased supersonic film cooling methods throughout the present thesis.

The conventional film cooling method, which serves as the benchmark for the numerical trials, was defined as the injection of a mixture of hydrogen and water-vapor at supersonic velocities along the nozzle wall. The biased supersonic film cooling definition follows the same form as the conventional, but includes extracting hydrogen from the TEG to form a wall-biased stream half the thickness of the slot height. Fig. 22 and Fig. 23 have been provided below and on the following page to highlight the injection of TEG (yellow) and hydrogen (blue) for both the conventional and biased methods.

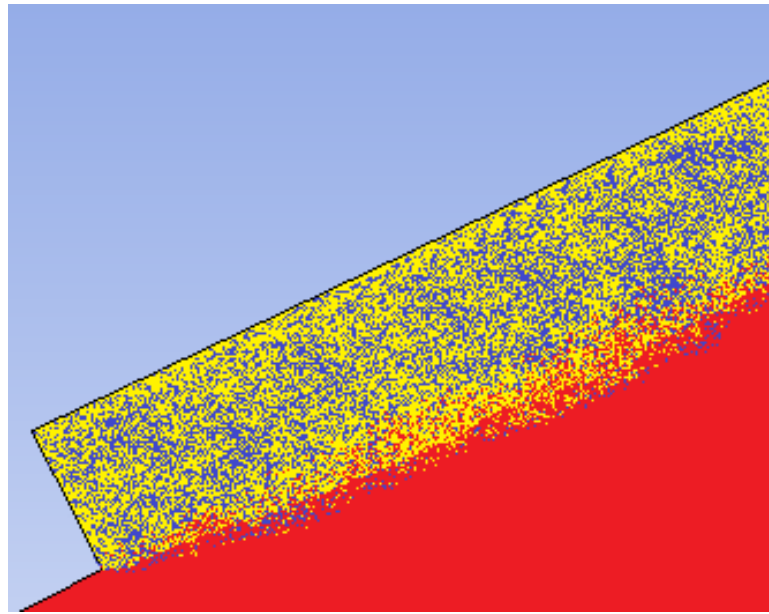


Figure 22: Conventional supersonic film cooling method with mixed TEG injection.

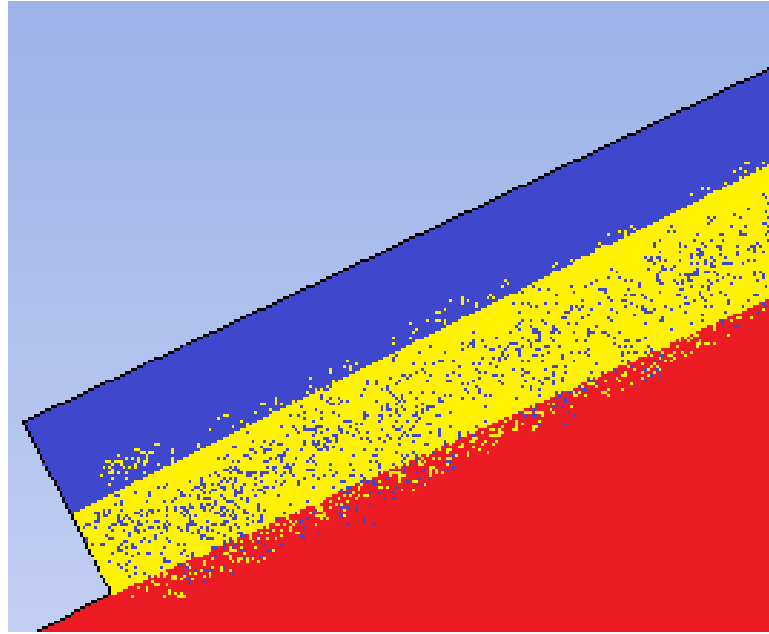


Figure 23: Biased supersonic film cooling method with separated TEG injection.

Fig. 22 and Fig. 23 demonstrate the injection process for both the conventional and biased film cooling methods. Creating numerical models of each method can be readily accomplished, but certain parameters must be matched in order to ensure that the results of each trial are comparable.

The parameters associated with film cooling include the velocity ratio, temperature ratio, blowing ratio, pressure ratio, density ratio, and specific heat ratio. Each of these ratios normalizes a slot parameter by a reference value. Matching the various ratios between the conventional and biased supersonic film cooling methods allows for comparisons between the subsequent results. The ratio matching process is discussed in further detail in section 7.4.

Chapter 5: Phase II: Computational Gas Model

5.1 Introduction

High-fidelity combustion simulations of rocket engines require the use of an elaborate large eddy simulation (LES) in conjunction with a dedicated combustion solver to handle the added molecular-kinetic calculations [99]. These simulations provide a great deal of insight into the inner workings of the combustion chamber, but come at the cost of additional computational requirements. While the combustion process within the thrust chamber is of importance, it does not have a major impact on nozzle extension film cooling apart from downstream turbulence effects. Therefore, it was decided to investigate alternative modeling methods to approximate the core-flow properties of the Vulcain II engine.

5.2 Alternatives Gas Models

Simulating the combustion process within the Vulcain II combustion chamber presented three drawbacks: added model complexity, greater computational allocation, and longer simulation times. To avoid these problems, alternative modeling techniques were explored.

An initial investigation of modeling alternatives produced a number of different approaches that ranged from a reduced chemical kinetic combustion model to approximating the core-flow as pure water-vapor. The reaction model, while simplified, required more computational assets than desired. On the contrary, modeling the core-flow as pure water-vapor was an oversimplification due to the fuel-rich combustion process. In short, a gas model that captured the behavior of the combustion products within the nozzle extension was required.

Striking a balance between a sophisticated combustion simulation and an oversimplified model can be accomplished by modeling the combustion product interactions. By focusing on the combustion constituents, the majority of the engine can be modeled accurately in a time-effective manner. In essence, the core-flow can be approximated as a gas mixture of constant composition that reproduces the transport properties found in the actual engine. While this approach is appealing, it can only be implemented if the combustion process approaches completion within the thrust chamber. To verify the nature of the Vulcain II combustion process, a specialty code developed by NASA known as 'Chemical Equilibrium with Application' (CEA) was utilized.

CEA is a program that 'calculates chemical equilibrium product concentrations from any set of reactants and determines thermodynamic and transport properties for the product mixture' [100]. The combustion code also incorporates subroutines for specific problems. One such subroutine calculates chemical compositions at various positions within a user-defined rocket engine. This particular subroutine was provided with data outlined in section 4.3 to generate information regarding transport properties, mixture composition, and intensive properties at various area ratios. Fig. 24 and Fig. 25 have been provided on the following page to demonstrate the species' variation within the core-flow as calculated by CEA.

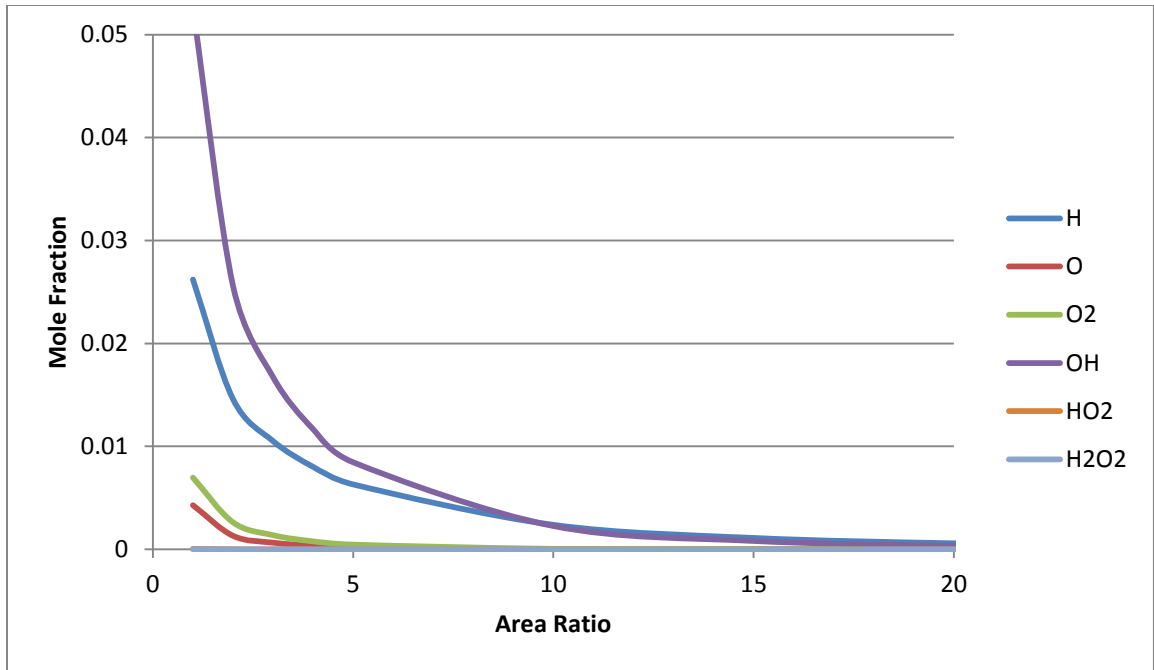


Figure 24: Combustion product mole fraction variation.

A number of gas constituents from the combustion process are not clearly visible in Fig. 24 above due to the near-zero mole fraction. The hydrogen and water-vapor constituents have been provided in the following plot due to the large percentages found in the combustion process.

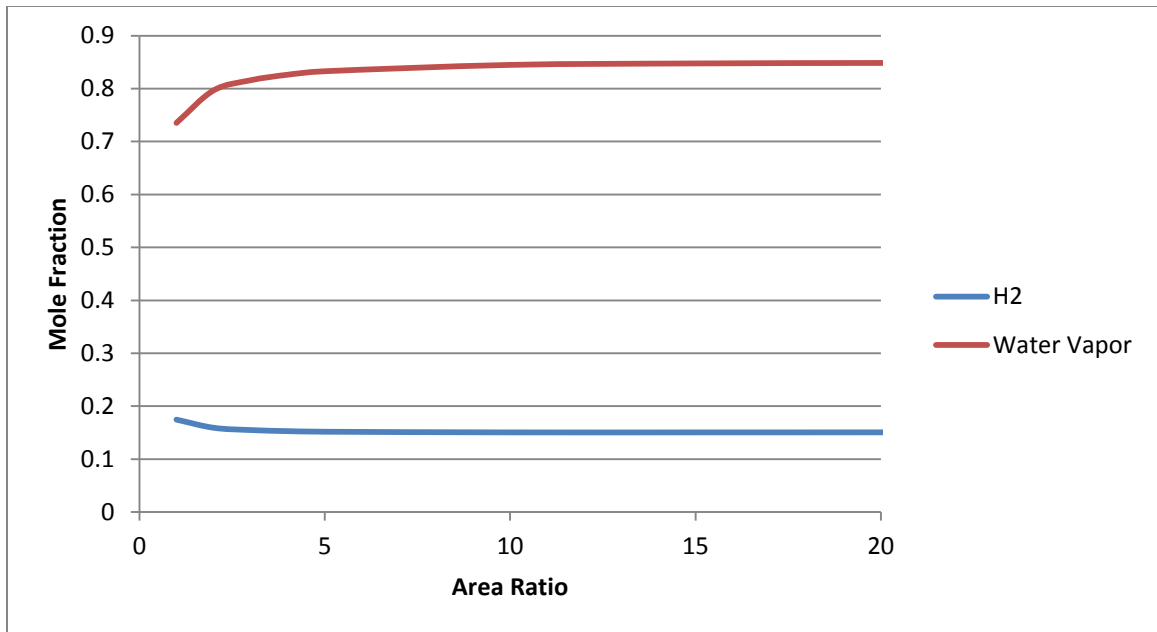


Figure 25: Hydrogen and water-vapor mole fraction variation.

Fig. 24 and Fig. 25 indicate that the chemical composition of the gas mixture stabilize after an area ratio of ten. This suggests that the nozzle extension is exposed to a non-reacting gaseous mixture comprised of water-vapor, hydrogen gas, and smaller percentages of the remaining combustion products. Astrium and Snecma have indicated that the newly designed thrust chamber for the Vulcain II achieves ‘reliable combustion efficiencies greater than 99%’ in the combustion chamber [81]. The CEA analysis coupled with the Astrium documentation regarding the combustion process of the Vulcain II suggests that the combustion process has reached completion by the time the gases exit the thrust chamber. While a small percentage of gases still undergo molecular changes within the nozzle, the gas constituent percentages remain largely unchanged aft of the throat region. Therefore, the core-flow of the engine was modeled with a non-reacting gas mixture of constant composition.

5.3 Core-Flow Composition

By definition a gas mixture is a collection of two or more constituent gases that contribute certain characteristics to the behavior of the mixture. The gas characteristics and transport properties of the gas mixture are largely dependent on mole fractions, mass fractions, and molecular interactions between the gas constituents [101]. According to the CEA analysis, the gas composition in the midsection of the nozzle, which is the primary location of the film injection, has the mole and mass fractions outlined in Table 7.

Table 7: Mole and mass fraction of core-flow gas mixture.

Core-Flow Mole Fractions		Core-Flow Mass Fractions	
Element	Mole Fraction	Element	Mole Fraction
Hydrogen (H)	0.00238	Hydrogen (H)	0.000154128
Hydrogen (H2)	0.15049	Hydrogen (H2)	0.019491414
Oxygen (O)	0.00002	Oxygen (O)	2.05574E-05
Oxygen (O2)	0.00005	Oxygen (O2)	0.000102787
Hydroxyl (OH)	0.00227	Hydroxyl (OH)	0.002480269
Water Vapor (H2O)	0.84479	Water Vapor (H2O)	0.977750845
Hydro-Peroxyl (HO2)	0	Hydro-Peroxyl (HO2)	0
Hydrogen-Peroxide (H2O2)	0	Hydrogen-Peroxide (H2O2)	0

The mole and mass fractions provided in Table 7 above were used to determine the specific heat, transport properties, and intermolecular parameters for the core-flow gas mixture. The following subsections detail the steps undertaken to calculate the gas characteristics of the core-flow.

5.4 Core-Flow Specific Heat Approximation

The specific-heat of the core-flow gas mixture was approximated with the use of a mass-weighted average of the constituent specific heats. In the case of a gas mixture that is exposed to a wide range of temperatures, the specific heat must be further modeled as a function of temperature due to non-linear behavior at high temperatures. These considerations have been mathematically modeled with the equation below.

$$C_{p_{mix}}(T) = \sum_{i=1}^N y_i C_{p_i}(T) \quad (7)$$

The equation above requires two pieces of information for each constituent to be known: the mass fraction and the temperature-dependent specific. The mass fractions were determined with the aid of CEA and have been provided in Table 7 on the previous page. The specific heat variation for each combustion product was determined with the aid of NASA Technical Memorandum 4513 [102].

NASA Technical Memorandum 4513 contains experimentally obtained curve-fits for the specific heat of various gases. The curve-fits are tabulated in a numerical format comprised of high-order coefficients that correspond to the following equation.

$$C_p(T) = C_{p_0} + C_{p_1}T + C_{p_2}T^2 + C_{p_3}T^3 + C_{p_4}T^4 \quad (8)$$

Substituting the above relation into the gas mixture specific heat expression yields the following result.

$$C_{p_{mix}}(T) = \sum_{i=1}^N y_i (C_{p_0} + C_{p_1}T + C_{p_2}T^2 + C_{p_3}T^3 + C_{p_4}T^4)_i \quad (9)$$

The process of calculating the specific heat of a gas mixture requires the use of high order coefficients and algebraic simplifications that are not quickly accomplished by hand. Therefore, a series of computer programs were established to automate the gas mixture specific heat calculations.

The specific heat of the core-flow was originally estimated with the aid of a Matlab script file. The various mole fractions and polynomial coefficients obtained from the CEA analysis and NASA TM 4513 were imported into a Matlab script for analysis, but the resolution of the machine epsilon could not capture the higher order coefficients. In short, the script file, while mathematically sound, required greater accuracy than Matlab could replicate. To eliminate the machine epsilon issues, a Microsoft Excel file was created to calculate the specific heat polynomial for the core-flow. Fig. 26 on the following page provides a plot of the core-flow specific heat over a range of temperature values. A polynomial representing the temperature-dependent specific heat of water-vapor has also been included for comparison purposes.

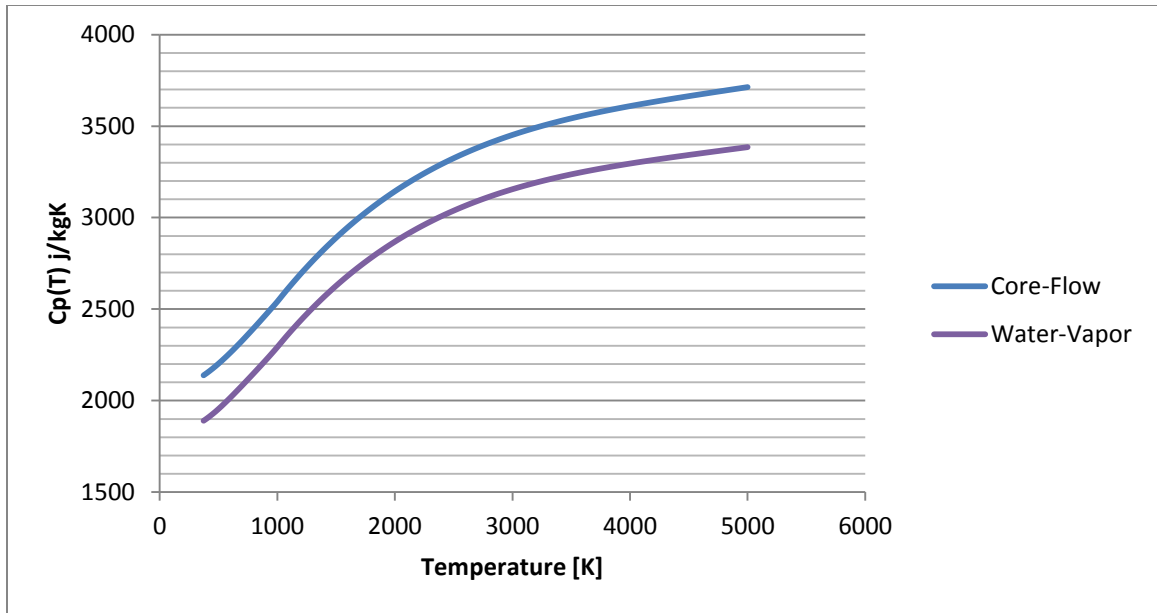


Figure 26: Core-flow and water-vapor specific heat variation.

The core-flow specific heat temperature variation, located in Fig. 26 above, was curve-fit with a high order, piece-wise polynomial. The resulting curve-fit coefficients have been provided in the appendix. The piece-wise polynomial coefficients were ultimately used to generate a material definition for the core-flow in the CFD solver.

5.5 Core-Flow Transport Properties

Unlike the methodology used to determine the specific heat variation of the core-flow, the viscosity and thermal conductivity of the mixture is a function of not only temperature and composition, but constituent molecular interaction as well. To model the interactions, the approach suggested by Gorden et. al (1984) was utilized [103]. This approach requires the following calculations.

$$\phi_{ij} = \frac{1}{4} \left[1 + \sqrt{\frac{\mu_i(T)}{\mu_j(T)} \left(\frac{M_j}{M_i} \right)^{\frac{1}{4}}} \right]^2 \sqrt{\frac{2M_j}{M_i+M_j}} \quad (10)$$

$$\psi_{ij} = \phi_{ij} \left[1 + \frac{2.41(M_i-M_j)(M_i-0.412M_j)}{(M_i+M_j)^2} \right] \quad (11)$$

$$\mu_{mix} = \sum_{i=1}^N \frac{x_i \mu_i(T)}{x_i + \sum_{\substack{j=1 \\ j \neq i}}^{NM} x_j \phi_{ij}} \quad (12)$$

$$k_{mix} = \sum_{i=1}^N \frac{x_i k_i(T)}{x_i + \sum_{\substack{j=1 \\ j \neq i}}^{NM} x_j \psi_{ij}} \quad (13)$$

Utilizing the equations above in conjunction with transport property data obtained from NASA TM 4647, the temperature-dependent polynomials were developed for the viscosity and thermal conductivity of the core-flow [104]. The resulting polynomials were curve-fit in a piece-wise fashion to finalize the material definition of the core-flow.

5.6 Turbine Exhaust Gas Composition and Properties

The turbine exhaust gas mixture used for film injection is comprised of only hydrogen and water-vapor. The intense mixing and relatively long duration of time spent within the gas-generator allows for a complete combustion to form water-vapor and excess

hydrogen gas. A combustion analysis using the CEA code was undertaken to verify this completion. A series of tabulated CEA results for various area ratios have been provided in the appendix. Table 8 below provides the resulting mole and mass fractions of the turbine exhaust gas.

Table 8: TEG mole and mass fractions.

TEG Mole Fractions		TEG Mass Fractions	
Element	Mole Fraction	Element	Mass Fraction
Hydrogen (H)	0.000000E+00	Hydrogen (H)	0.000000E+00
Hydrogen (H2)	8.866000E-01	Hydrogen (H2)	4.666454E-01
Oxygen (O)	0.000000E+00	Oxygen (O)	0.000000E+00
Oxygen (O2)	0.000000E+00	Oxygen (O2)	0.000000E+00
Hydroxyl (OH)	0.000000E+00	Hydroxyl (OH)	0.000000E+00
Water Vapor (H2O)	1.134000E-01	Water Vapor (H2O)	5.333546E-01
Hydro-Peroxyl (HO2)	0.000000E+00	Hydro-Peroxyl (HO2)	0.000000E+00
Hydrogen-Peroxide (H2O2)	0.000000E+00	Hydrogen-Peroxide (H2O2)	0.000000E+00

The information provided in the table above was used to predict the gas properties of the turbine exhaust gases via a process identical to that described in sections 5.4-5.5

5.7 Lennard-Jones Parameters

Injecting two or more gases into a computational domain requires a series of mixing laws to account for the interaction of the various gases. The mixing laws account for the intensive properties, molecular composition, and transport properties at each node. The majority of the mixing laws follow a weighted averaging methodology; however, the transport properties at nodes containing two or more gases were calculated with the aid of kinetic theory. The use of the kinetic theory weighting laws requires both the Lennard-Jones parameter as well as the average molecular diameter of each constituent to be provided.

The Lennard-Jones (L-J) parameter and average molecular diameter are used to calculate the transport properties at nodes where two or more gases are present. The L-J

parameters for the various gas constituents were obtained from *Hypersonic Aerodynamics and High Temperature Gas Dynamics* and the Fluent material database [105]. The characteristic length of the gas mixtures and the L-J parameter were determined with a molar weighted average. The L-J and characteristic lengths have been provided in Table 9 and Table 10 below.

Table 9: L-J Characteristic length parameters and weighted values.

Element	Sigma [Angstroms]	Core-Flow Weighted Sigma [Angstroms]	TEG Weighted Sigma [Angstroms]
Hydrogen (H)	2.05	0.00	0.00
Hydrogen (H ₂)	2.92	0.44	2.589
Oxygen (O)	2.75	0.00	0.00
Oxygen (O ₂)	3.433	0.00	0.00
Hydroxyl (OH)	2.75	0.01	0.00
Water Vapor (H ₂ O)	3.198	2.70	0.36264
Hydro-Peroxyl (HO ₂)	3.44	0.00	0.00
Hydrogen-Peroxide (H ₂ O ₂)	3.458	0.00	0.00
Weighted Sum	-	3.152	2.952

Table 10: Lennard-Jones parameters and weighted values.

Element	L-J Parameter [K]	Core-Flow Weighted L-J Parameter [K]	TEG Weighted L-J Parameter [K]
Hydrogen (H)	145.00	0.345	0.000
Hydrogen (H ₂)	38.00	5.719	33.691
Oxygen (O)	80.00	0.002	0.000
Oxygen (O ₂)	113.00	0.006	0.000
Hydroxyl (OH)	80.00	0.182	0.000
Water Vapor (H ₂ O)	572.40	483.558	64.910
Hydro-Peroxyl (HO ₂)	3.45	0.000	0.000
Hydrogen-Peroxide (H ₂ O ₂)	107.40	0.000	0.000
Weighted Sum	-	489.81	98.601

The values provided in the above tables were obtained from a number of sources [105]. However, literature does not provide a universally accepted value for the characteristic length for water-vapor. To address these discrepancies a number of water models were studied [106]. This investigation yielded a number of characteristic lengths which have been

provided in the appendix. Averaging the results of the water model investigation yielded a characteristic length of 3.198 angstroms. The Lennard-Jones and characteristic length information was used to generate plots of the Lennard-Jones potential variation provided in Fig. 27 below and Fig. 28 on the following page.

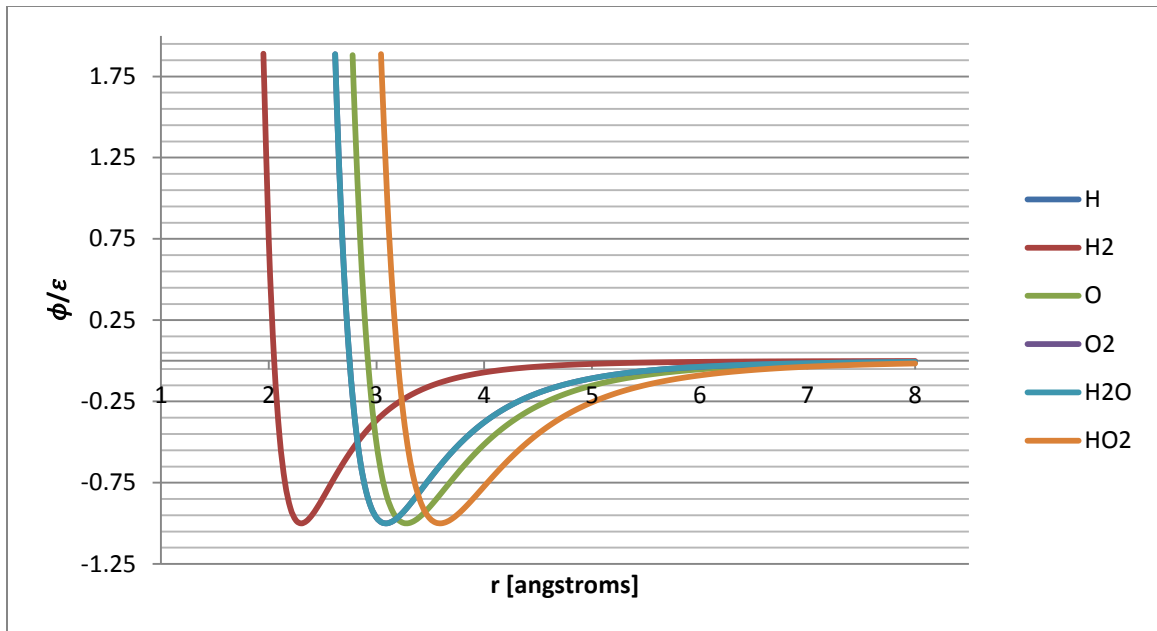


Figure 27: Lennard-Jones parameters for core-flow constituent gases.

Due to the equal characteristic lengths, a number of constituents share the same Lennard-Jones curve.

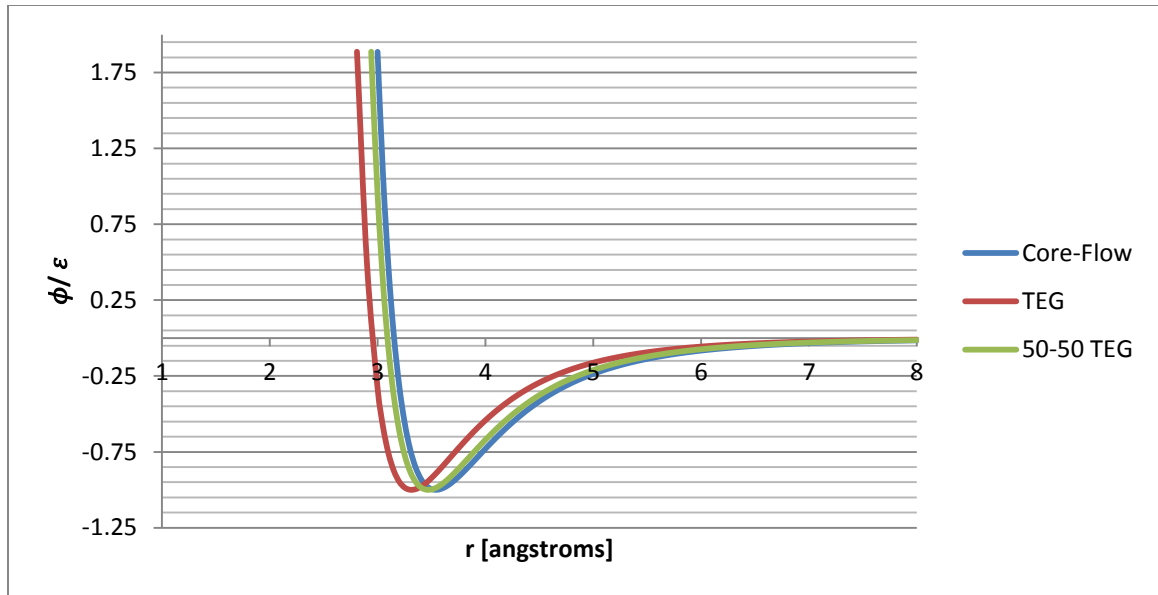


Figure 28: Lennard-Jones parameters for core-flow and turbine exhaust gas mixtures.

5.8 Film Mole Fraction Adjustment

Dividing the TEG into a stream of pure hydrogen and a secondary stream of excess hydrogen and water-vapor alters the gas composition within the two streams. In other words, the extraction of hydrogen atoms from the TEG to form the hydrogen layer affects the gas properties of the remaining gas. Fortunately, the amount of atoms extracted from the turbine exhaust gas is directly proportional to the thickness of the hydrogen film. This fact was used to predict the constituents of the turbine exhaust gas as a function of hydrogen film thickness.

Extracting hydrogen atoms to form a film layer comprised of pure hydrogen alters the constituent percentages within the turbine exhaust gas. A relation between the various parameters can be defined in two ways: mass balances or an atom-count relation. While both methods can be used to relate the various parameters of interest, the atom-count method was utilized due to its simplicity.

The atom-count relationship utilizes the fact that the number of hydrogen atoms and water-vapor atoms injected is constant per unit time. By relating the hydrogen film thickness

to the volumetric atom density, a relation between hydrogen film thickness and mole fractions was obtained. The mole fractions of hydrogen and water-vapor were plotted against the hydrogen film thickness and have been provided in Fig. 29 below.

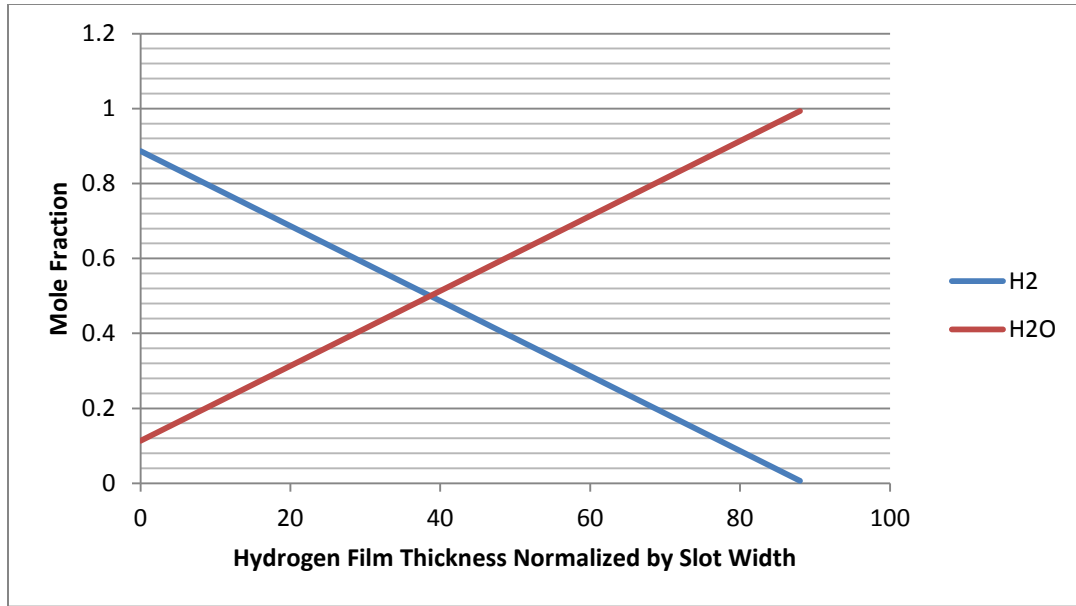


Figure 29: Atom-count relations between normalized film thickness and mole fraction.

The figure above indicates that the maximum thickness of the hydrogen film is related to the amount of hydrogen atoms present in the turbine exhaust gas. The relation between film thickness and constituent percentages was used to adjust the turbine exhaust gas properties. The properties of the adjusted exhaust gases were calculated in the same manner described in sections 5.3-5.4 using different mole and mass fractions.

Injecting the different gases can be achieved with one of two approaches: adjust the turbine exhaust gases with new polynomials to account for the adjusted gas properties or inject an appropriate amount of hydrogen gas and water-vapor at the appropriate boundary conditions. Both methods work well and have their advantages and disadvantages. For example, tailoring the turbine exhaust gases prior to injection saves a reasonable amount of

time with respect to data entry. On the contrary, injecting a hydrogen and water-vapor mixture allows for tracking of individual gas constituents within the post processor. Due to the existing files dedicated to gas property calculation, the turbine exhaust gases were adjusted prior to injection. While the atom count relation is sufficient for the current analysis, it is not without disadvantages.

The thickness of the hydrogen gas is also a function of the density of the gases being injected. For the purposes of this thesis, the density of the two gases was averaged out to generate a constituent function based entirely on hydrogen film thickness. An in depth analysis of density gradient affects has been presented by Kiran Dellimore in his Doctoral thesis 'Modeling and Simulation of Mixing Layer Flows for Rocket Engine Film Cooling' [32].

5.9 Temperature-Dependent Gas Property Plots

Sections 5.1-5.8 discuss the process used to calculate the gas property characteristics of the core-flow and turbine exhaust gases. The specific heat and transport property piece-wise curve-fit coefficients have been provided in the appendix. While this material is of use, plots of the temperature-dependent gas characteristics offer visual information that tabulated data lacks. Therefore, a series of plots highlighting the numerous gas characteristic of both the constituent gases as well as the gas mixtures has been provided in section 5.9.1 and 5.9.2.

5.9.1 Constituent Temperature-Dependent Plots

To illustrate the temperature-dependent nature of the various gas properties, the following plots have been provided. The constituent temperature-variations were determined with the information provided in NASA TM 4513 and NASA TM 4647 following the calculations provided in sections 5.4 and 5.5.

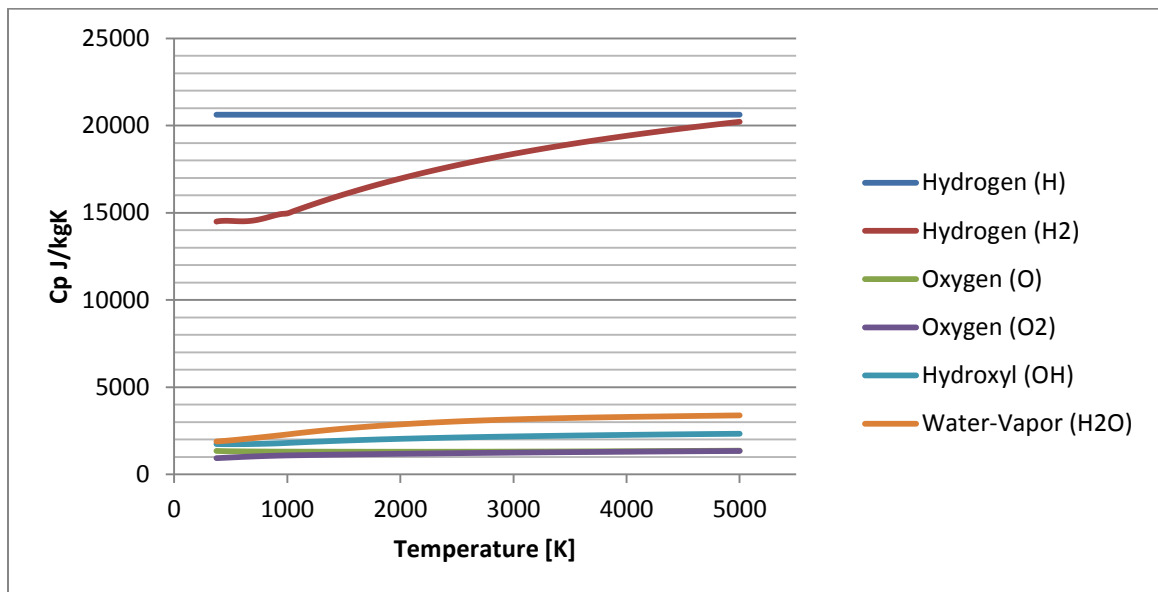


Figure 30: Temperature-dependent constituent specific heat.

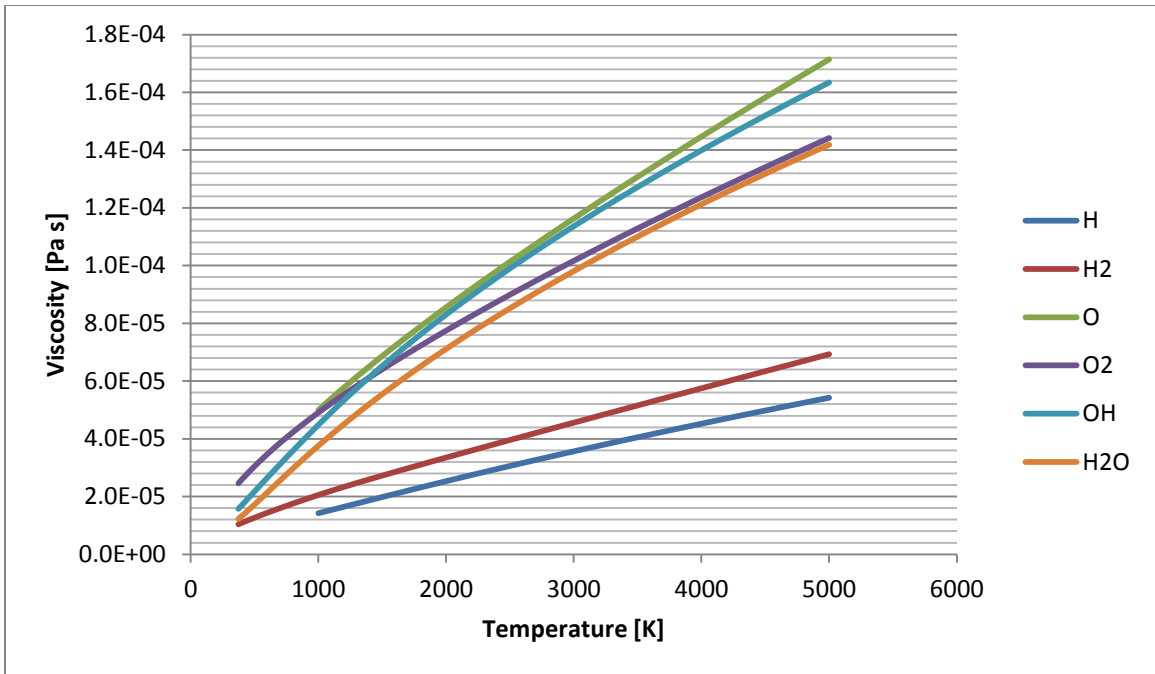


Figure 31: Temperature-dependent constituent viscosity variation.

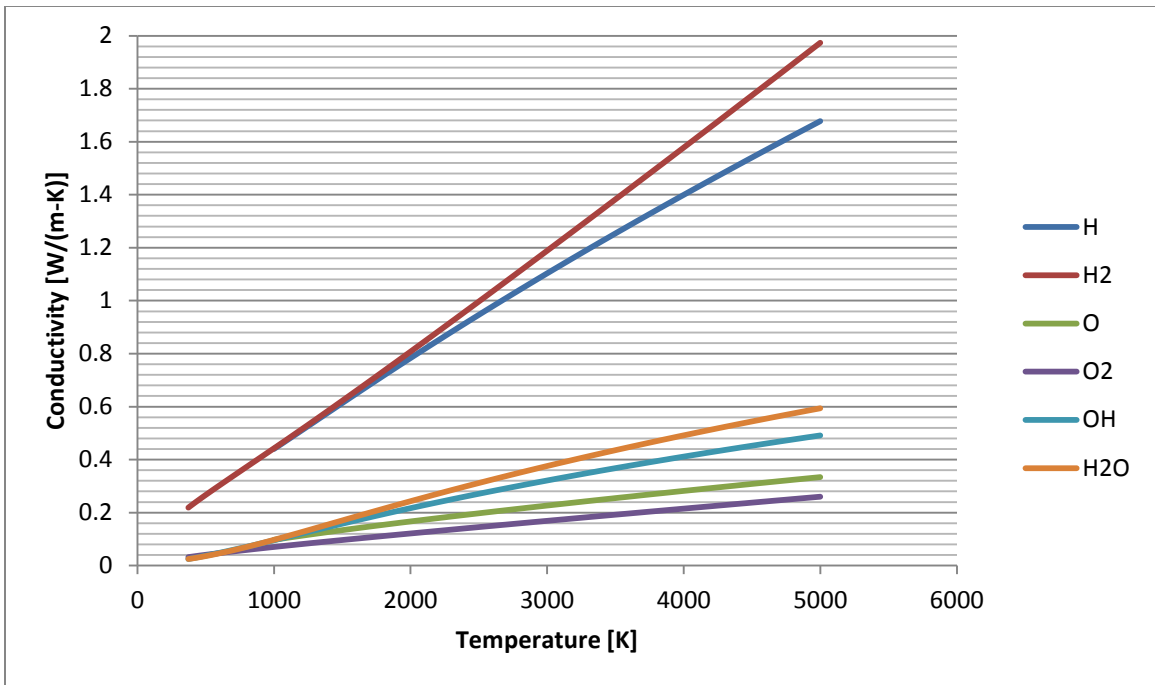


Figure 32: Temperature-dependent conductivity variation.

5.9.2 Gas Mixture Temperature Dependent Plots

The following figures outline the gas mixture temperature dependent variations. The curves denoted by the title 'TEG' refer to the gas properties of the conventional injection process. Conversely, the curves titled '50-50 TEG' refer to the TEG gases after the hydrogen atoms have been extracted to form the wall-biased film.

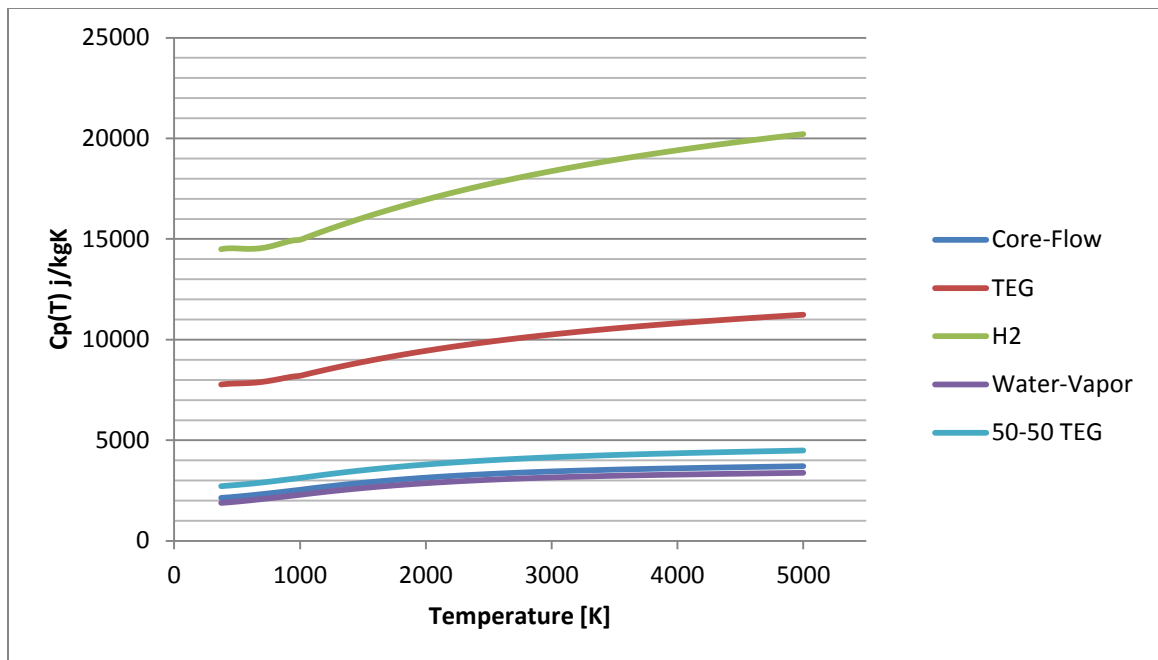


Figure 33: Temperature-dependent gas mixture specific heat variation.

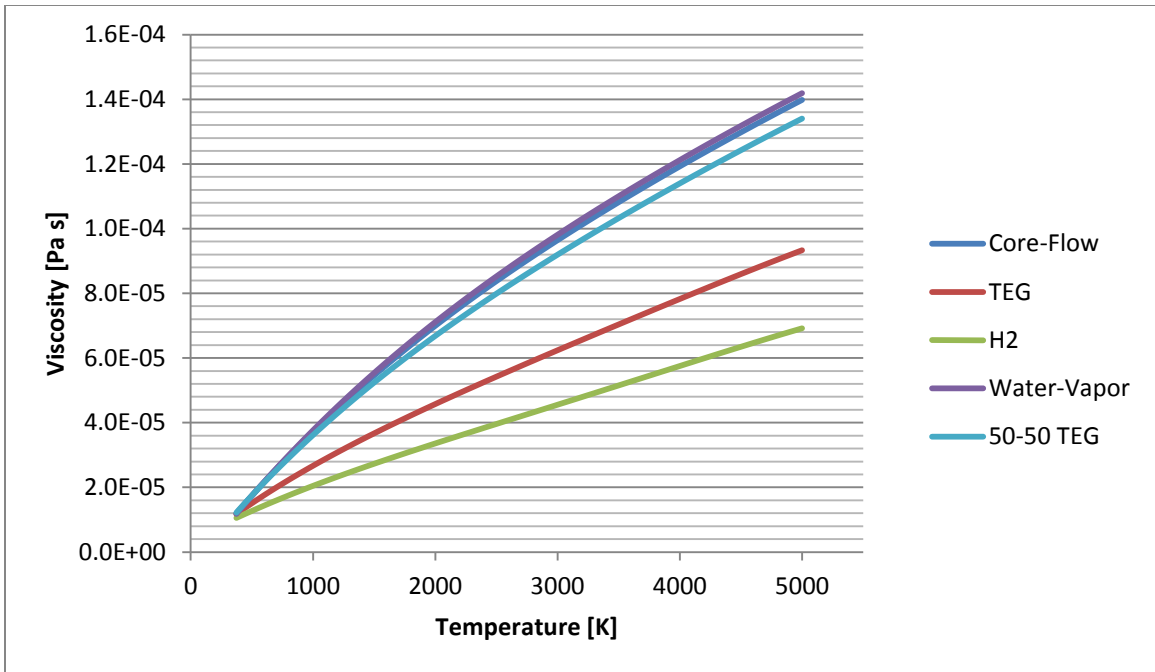


Figure 34: Temperature-dependent gas mixture viscosity variation.

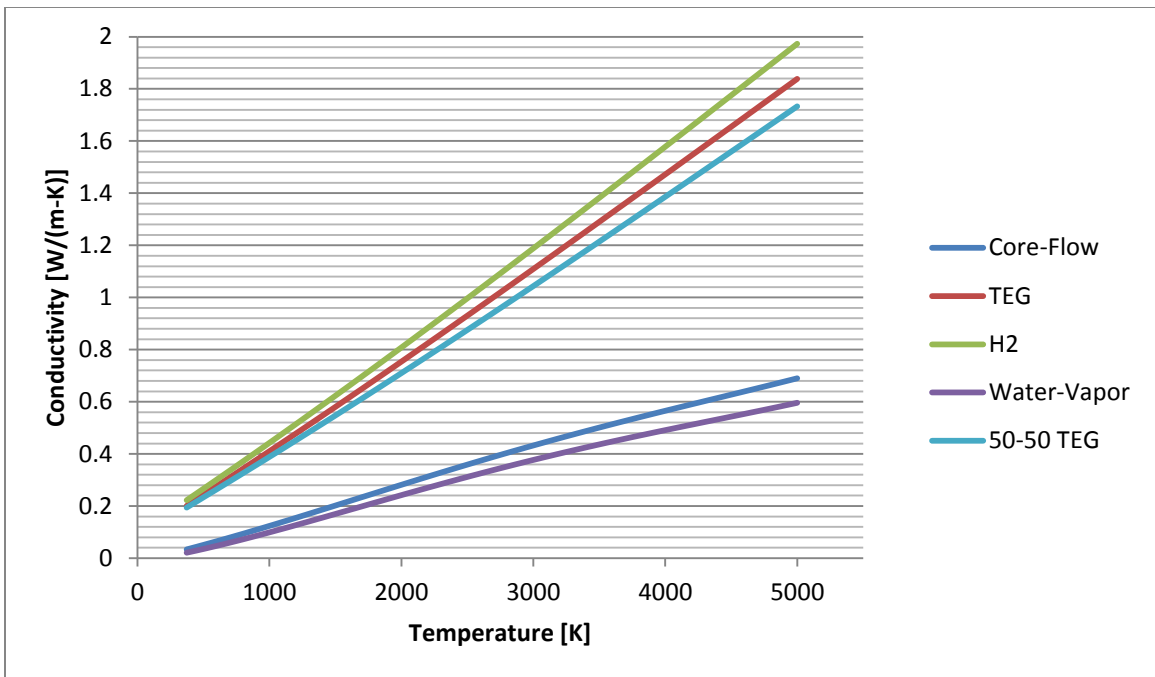


Figure 35: Temperature-dependent gas mixture conductivity variation.

Chapter 6: Phase III: Biased Flat Plate Analysis

6.1 Introduction

Prior to testing the proposed cooling method on a full-scale model of the modified Vulcain II engine, a series of flat plate models were investigated.

6.2 Model Parameters

To reduce the amount of redundant models, the flat plate models used for the verification of the CAL-Tech experiments were repropose for this analysis. Therefore, the geometry and mesh characteristics for the biased flat plate models were identical to the models outlined in section 4.2. However, there were a number of alterations made to the models to better approximate the conditions experienced within a nozzle extension.

The original CAL-Tech flat plate models utilized air as both the mainstream and film gases. To subject the biased supersonic film cooling method to an environment similar to that of a nozzle extension, the mainstream and film gases were altered to mimic the properties of the core-flow and turbine exhaust gases discussed in sections 5.4-5.8. Additionally, the slot-averaged Mach number was varied from 1.1 to 3.0 with a constant static temperature of 500 Kelvin while the mainstream Mach was maintained at 2.5 with an injection static temperature of 1,500 Kelvin. Additional model parameters have been provided in Table 11 below.

Table 11: Biased flat plate boundary condition parameters.

Boundary Condition	Type	Velocity [m/s]	Pressure [Pa]	Temperature [K]
Main Inlet	Velocity Inlet	2,575.28	101,325	1,500
Film Inlet	Velocity Inlet	Variable	105,000	500
Walls	Adiabatic Walls	0	N/a	Adiabatic
Outlet	Pressure Outlet	N/a	90,000	N/a

6.3 Proof of Concept

The biased flat plate simulations produced temperature, velocity, and mass fraction information that was extracted via the ANSYS post processor 'CFD-Post'. The post-process data was analyzed with the aid of Microsoft Excel and Matlab to generate both temperature ratio and film cooling effectiveness plots. The following plots highlight the thermal improvements awarded by the BSSFC method. A more detailed account of the biased flat plate results has been provided in section 8.1.

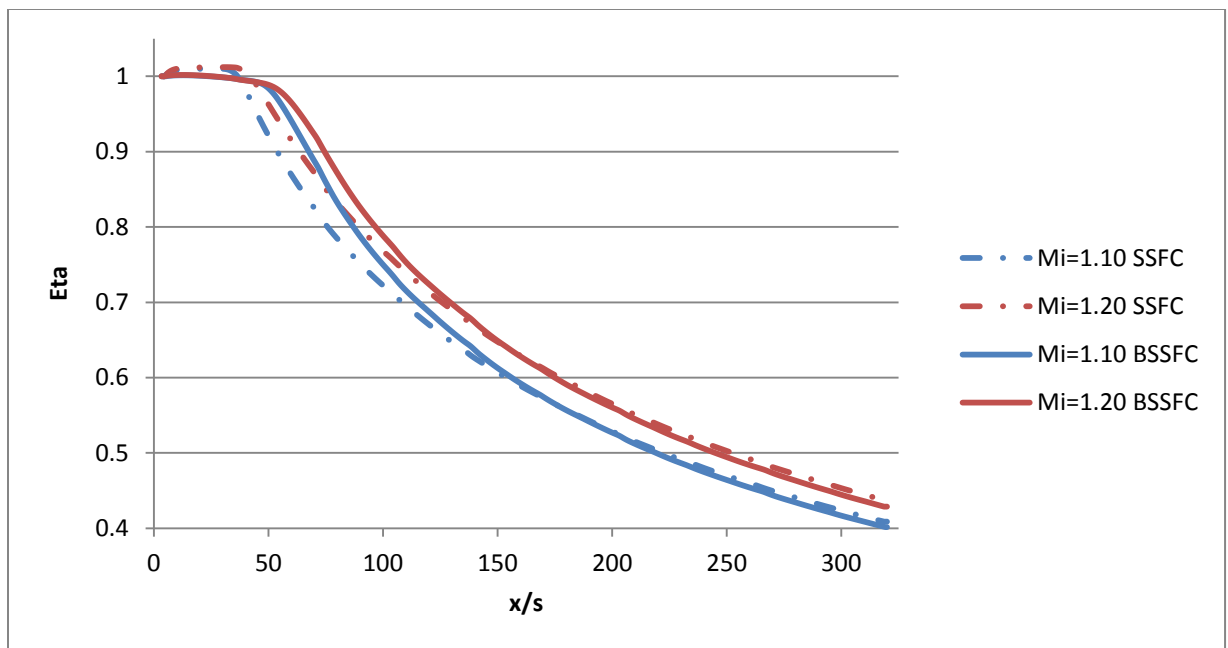


Figure 36: Biased flat plate film cooling effectiveness.

To demonstrate the effect BSSFC has on the nozzle wall temperatures, a series of calculations were performed. The analysis compared the CSSFC and BSSFC methods via wall temperature reduction percentage calculations for two different injection Machs. A plot of the reduced wall temperature percentage has been provided in Fig. 37 on the following page.

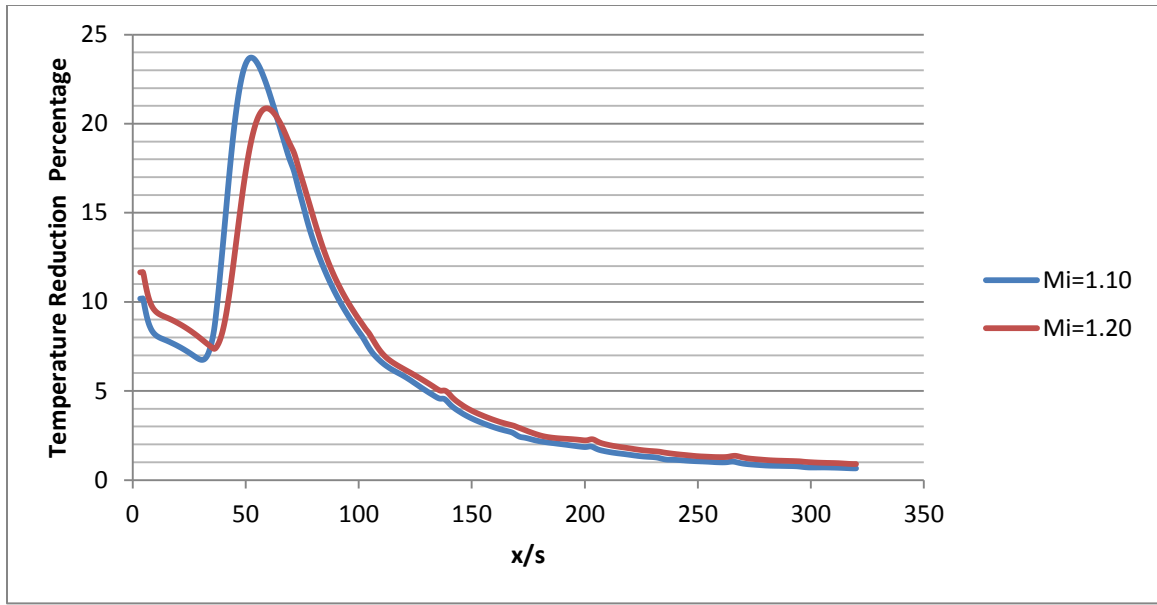


Figure 37: BSSFC wall temperature reduction.

The film cooling effectiveness and wall temperature reduction plots found in Fig. 36 and Fig. 37 indicate that the BSSFC method produces favorable results when compared the conventional method. However, the film cooling effectiveness improvements were not as high as expected. It is believed that reflected shocks emanating from the shock-lip expansion fan induced additional mixing due to shock-boundary-layer interactions. While the increased mixing reduced overall cooling effectiveness, the results provided an initial proof-of-concept for the BSSFC method and Phase III was declared successful.

Chapter 7: Phase IV: Modified Vulcain II

7.1 Introduction

The verification of the biased supersonic film cooling method fulfilled the objective of the third phase of research. The flat plate analysis indicated that the BSSFC method increased the film cooling effectiveness. However, the flat plate models did not demonstrate the viability of the proposed method on a large rocket engine. The various pressure, temperature, velocity, and density gradients experienced in a rocket engine are not accounted for in the biased flat plate analysis. Therefore, the final phase of research was conducted with the intent of applying the BSSFC method to the modified Vulcain II engine described in section 4.3.

7.2 Geometry and Slot Injector

The geometry of the Vulcain II engine was approximated by utilizing image processing techniques in CATIA and Matlab. The steps undertaken to perform the image processing have been detailed in section 4.4.

In order to generate a series of models with different film injection locations, the default nozzle contour was altered with the aid of a Matlab script. The script utilized a database containing several hundred points from the default engine contour. These points contained axial coordinates and the corresponding wall radii of the nozzle contour. The engine coordinates were read into Matlab and subjected to a series of commands that altered the coordinates to include a film injection slot at a specified location.

The points aft of the injection location were altered with the aid of a mass-balance equation such that the gas-side of the film produced the same contour as the default nozzle contour. The script file was also able to position the film slot such that the film was injected parallel to the nozzle wall adjacent to the injection site. Once the coordinate alterations had

been completed, the script wrote new engine coordinates to an excel file for plotting and visual inspection. A sample of the slot injection geometry has been provided in the following figure.

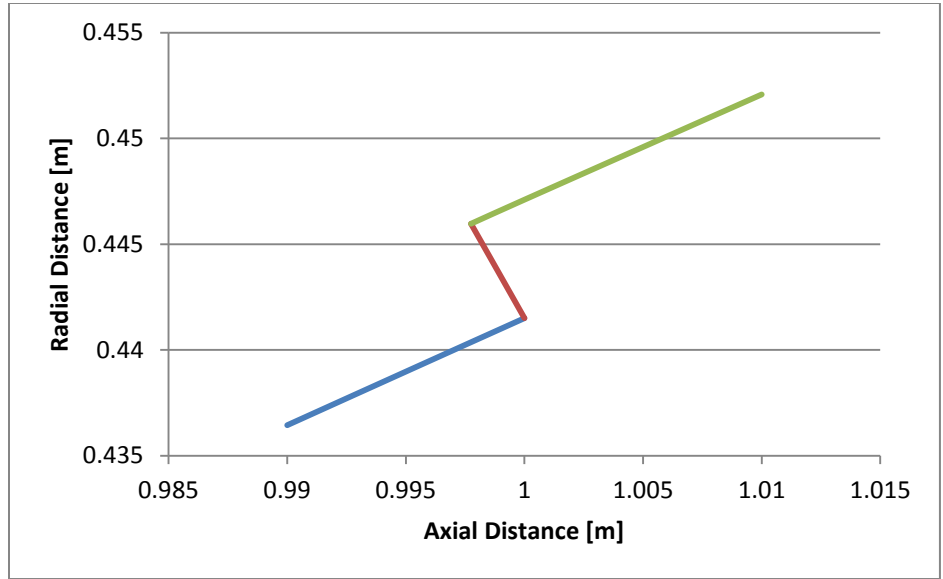


Figure 38: Sample injection geometry produced by Matlab film-injection script.

Table 12 has been provided below to detail the slot location of each Model. The distances were selected based on the approximate turbine exhaust manifold location of engines currently in service. In general terms, the turbine exhaust manifold is located approximately halfway between the exit plane of the engine and the throat. This information was used to produce four different film cooled engines. Approximate engine geometry for each engine has been provided in the appendix.

Table 12: Film cooled nozzle slot locations.

Model	Distance from Shower Head [m]	Distance from Throat [m]
A	0.75	0.315
B	1.00	0.565
C	1.25	0.815
D	1.50	1.065

7.3 Meshing Process

The slot insertion process generated four different film cooled engines with unique rearward slot locations. Each model was meshed with a fine, 2D, structured grid that was refined with the aid of a mesh independence study.

7.3.1 Mesh Independence Study

The resolution of a mesh can have a significant impact on the validity of a simulation. In an ideal world, a mesh would be comprised of a near-infinite amount of cells to obtain the most accurate solution. However, the computational requirements to run such a model are astronomical. Therefore, a balance must be found between mesh size and solution accuracy. To investigate the relationship between the mesh size and solution accuracy, a mesh independence analysis was performed.

A mesh independence analysis focuses on the simulation of a particular model using various grids. By observing the results of each simulation, one can ascertain the minimum amount of cells required to capture the flow field accurately. For the purposes of this mesh independence analysis, a sample engine was selected, meshed numerous times, and analyzed for accuracy. Table 13 below provides the amount of cells used in each simulation.

Table 13: Mesh independence model mesh sizes.

Model	Mesh Size
A'	221K
B'	311K
C'	487K
D'	627K
E'	824K
F'	1.386 Mil

While the amount of cells in each mesh may appear arbitrary, there is significance behind the values chosen. Apart from the exit plane of the nozzle, each grid has a particular distribution that produces the most orthogonal cells with the lowest aspect ratio possible. This requirement was coupled with a general desire to change the cell distribution along segments in a linear fashion from one model to the next. In short, the mesh size of each model was dictated by the distributions used to obtain desirable cell characteristics. Once the models had been run to convergence, the results were compared to one another.

Comparing the results from one simulation to another can be accomplished in many ways; however, the importance of temperature made thermal comparisons a priority. Therefore, a series of splines were developed and inserted into the post-processor as a means to collect temperature values at several locations. Fig. 39 below highlights the inclusion of these splines in the flow field.

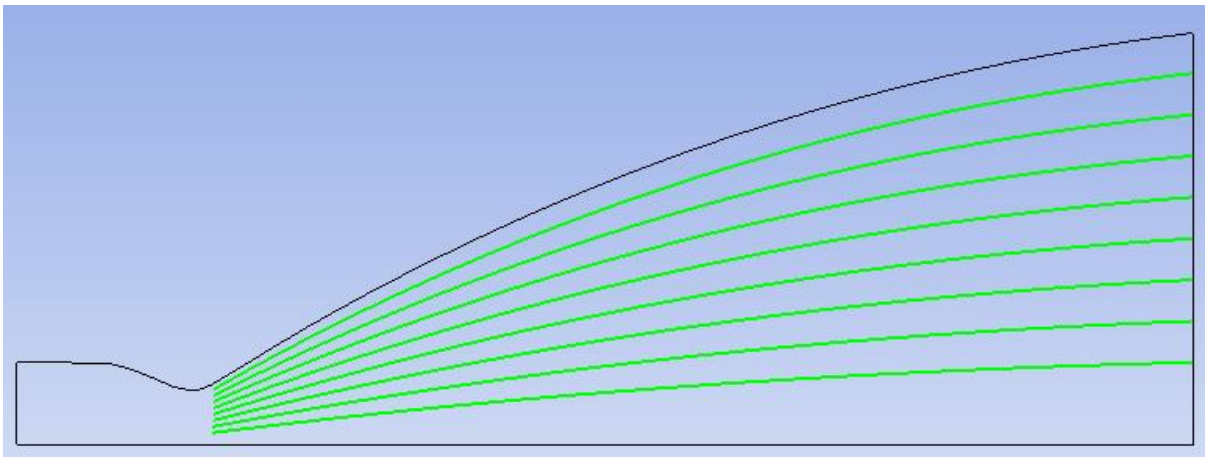


Figure 39: Default engine contour with splines for mesh independence analysis purposes.

As one can see from the figure above, the splines used to obtain temperature values were constructed to roughly match the streamlines of the engine. The temperature distribution along each spline was ultimately used to compare the influence of the mesh density for each solution. Fig. 40 and Fig. 41 on the following page represent the percent

difference of each model compared to the finest grid of 1.386 million cells for the near-center spline and outer spline respectively.

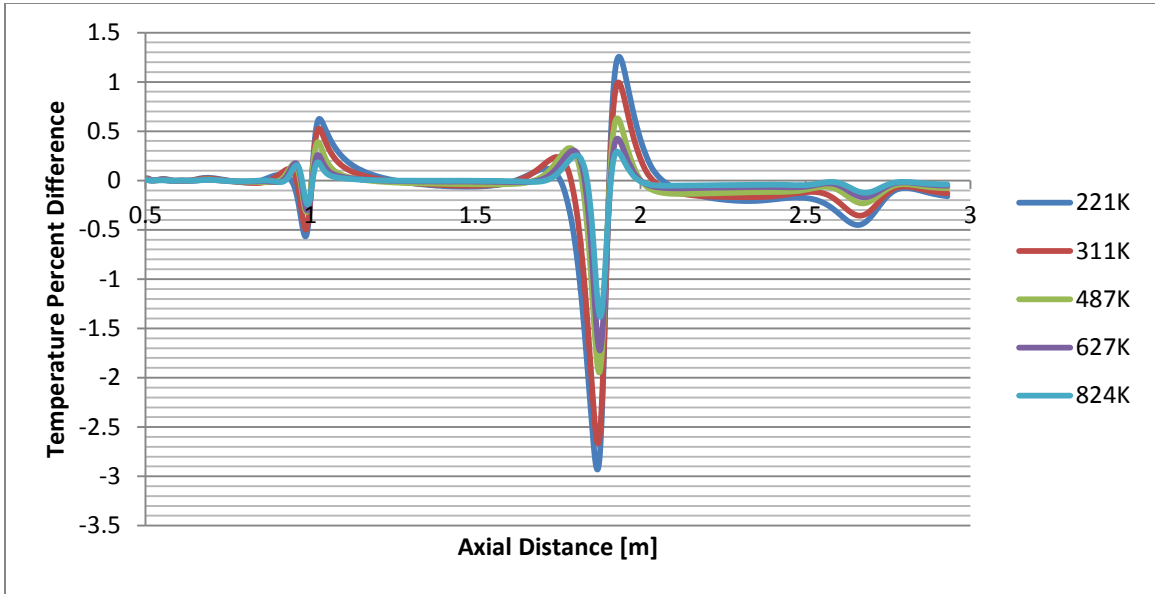


Figure 40: Mesh independence analysis: 'Near-Center Spline' temperature percent differences.

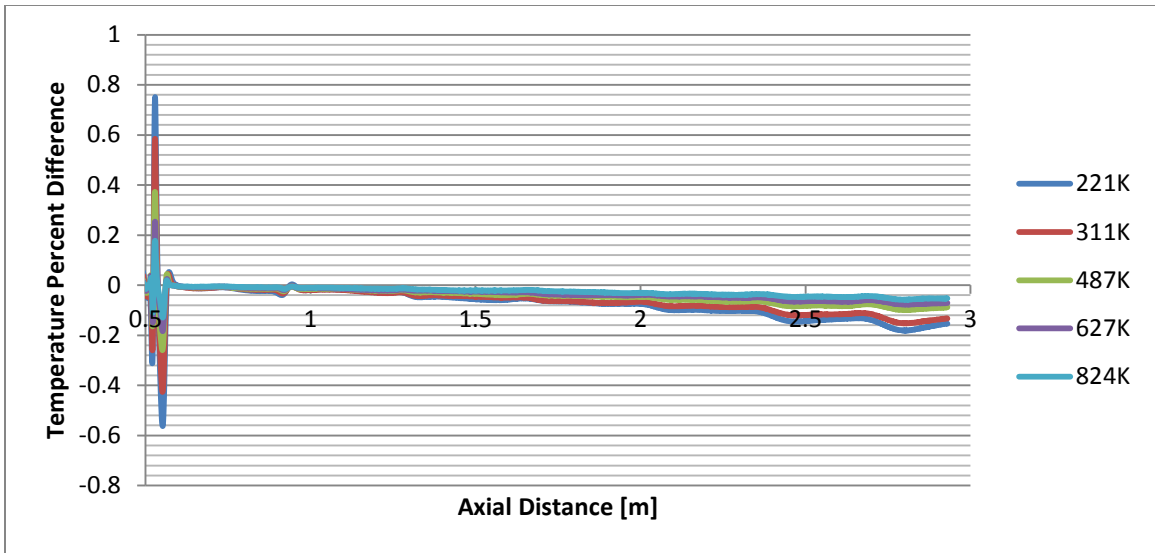


Figure 41: Mesh independence analysis: 'Near-Wall Spline' temperature percent differences.

The percent difference values presented in Fig. 40 and Fig. 41 above indicate that the overall solution does not vary greatly from one mesh to the next when compared to a

solution obtained from a 1.386 million cell grid. The largest percent differences, which have a maximum percent difference of 1%-3%, arise near the centerline of the model and near the throat region. In short, increasing the mesh fineness by a factor of four reduces the percent difference by half. The information obtained from this study was used to develop the final mesh of the film cooled nozzles.

7.3.2 Finalized Mesh

The information obtained from the mesh independence analysis was used to generate a series of two-dimensional, axisymmetric models of the modified Vulcain II engine. Each grid, while slightly different from one another, contained roughly 2 million cells. The large number of cells was preferred in order to ensure that the solutions were truly mesh independent.

7.4 Model Parameters

The boundary conditions of the film cooled engine simulations remain relatively unchanged from one model to the next. Each boundary condition was matched with the engine characteristics provided in section 4.3. The combustion chamber was supplied with a total pressure of 117.3 Bar and a total temperature of 3,525 Kelvin. These chamber conditions match those provided by the Snecma and Astrium documentation. Conversely, the exit pressure of the models was altered slightly.

The Vulcain II engine is designed for optimum operation in near vacuum conditions. Applying such a pressure to a commercial CFD solver is not practical due to the breakdown of the Navier-Stokes equations with the introduction of rarified gases [107]. To avoid such problems, the exit plane pressure was maintained at 5,000 Pascals. The pressure imposed on the exit boundary condition corresponds to an altitude of approximately 20.75 kilometers.

The parameters enforced on the film injection slot changed from model to model, but have been outlined in the following tables.

Table 14: Slot parameters for film cooled nozzle models.

Model	A	B	C	D
Static Slot Pressure [Pa]	522500	242899.8	143238.7	99418.88
Static Slot Temperature [K]	500	500	500	500
Slot-Averaged Density [kgm ³]	0.4304	0.4269	0.42426	0.422558

Table 15: Slot-averaged Mach and corresponding velocities.

Slot-averaged Mach	Velocity [m/s]
1.1	1347.807
1.15	1409.031
1.2	1470.247
1.25	1531.455
1.3	1592.653
1.5	1837.341
1.75	2142.923
2.0	2448.205
2.5	3058.394
3.0	3669.207

The injection static pressure was determined by performing a post process analysis of an initial series of biased film cooling models. The static pressure adjacent to the lip was extracted from the post-process results, increased by ten percent, and used for the final slot static pressures.

7.4.1 Parameter Ratio Matching Process

As stated previously, film cooling parameters follow the form of ratios of slot parameters normalized by reference parameters. For the purposes of this research, the reference parameters correspond to an inviscid, 2D, axisymmetric model of the ‘default’ Vulcain II engine generated in section 4.4. The wall parameters of the inviscid case roughly

approximate the parameters of boundary layer edge of the film cooled engines. These reference parameters were used to generate the various film cooling ratio parameters.

The static temperature and pressure values were maintained at the slot for each set of models. For example, every model ‘D’ slot pressure was maintained at 99,418.9 Pascals for both the conventional and biased film cooling trials. These constant values ensured that the temperature ratios remained the same for each trial pair. The following tables highlight the temperature and pressure ratios for the models.

Table 16: Initial film cooling reference parameters and corresponding ratios.

Model	A	B	C	D
Reference Temperature [K]	1994.86	1718.84	1545.93	1435.35
Reference Pressure [Pa]	387112	173637	100104	68829.7
Reference Density [kg/m ³]	0.34	0.18	0.11	0.08
Reference Velocity [m/s]	3215.65	3469.85	3614.59	3701.77
Temperature Ratio	0.25	0.29	0.32	0.35
Pressure Ratio	1.35	1.40	1.43	1.44
Slot-Averaged Density Ratio	1.26	2.40	3.72	5.01

The velocity and blowing ratios varied for each model pair due to the parameter nature of the trials. Tables 17-20 below detail the velocity and blowing ratio variation for each trial pair.

Table 17: Model ‘A’ film cooling velocity and blowing ratios.

Slot-Averaged Mach	Velocity Ratio	Slot-Averaged Blowing Ratio
1.1	0.419	0.528
1.15	0.438	0.552
1.2	0.457	0.576
1.25	0.476	0.600
1.3	0.495	0.624
1.5	0.571	0.720
1.75	0.666	0.840
2.0	0.761	0.960
2.5	0.951	1.199
3.0	1.141	1.438

Table 18: Model 'B' film cooling velocity and blowing ratios.

Slot-Averaged Mach	Velocity Ratio	Slot-Averaged Blowing Ratio
1.1	0.388	0.933
1.15	0.406	0.975
1.2	0.424	1.018
1.25	0.441	1.060
1.3	0.459	1.102
1.5	0.530	1.272
1.75	0.618	1.483
2	0.706	1.694
2.5	0.881	2.117
3	1.057	2.540

Table 19: Model 'C' film cooling velocity and blowing ratios.

Slot-Averaged Mach	Velocity Ratio	Slot-Averaged Blowing Ratio
1.1	0.373	1.388
1.15	0.390	1.451
1.2	0.407	1.515
1.25	0.424	1.578
1.3	0.441	1.641
1.5	0.508	1.893
1.75	0.593	2.207
2	0.677	2.522
2.5	0.846	3.151
3	1.015	3.780

Table 20: Model 'D' film cooling velocity and blowing ratios.

Slot-Averaged Mach	Velocity Ratio	Slot-Averaged Blowing Ratio
1.1	0.364	1.823
1.15	0.381	1.906
1.2	0.397	1.989
1.25	0.414	2.072
1.3	0.430	2.155
1.5	0.496	2.486
1.75	0.579	2.899
2	0.661	3.312
2.5	0.826	4.137
3	0.991	4.964

Chapter 8 Results

8.1 Biased Flat Plate Investigation

The biased flat plate investigation was conducted under Phase III of the BSSFC research. The goal of the biased flat plate models was to validate the effectiveness of the proposed cooling method. The validation process was conducted with a series of reproped flat plate models that simulated both the conventional SSFC method as well as the proposed BSSFC technique. The results of Phase III have been provided in section 8.1.1 and 8.1.2.

8.1.1 Biased Flat Plate Film Cooling Effectiveness

Equation (2), which defines the film cooling effectiveness for supersonic film cooling, was used in conjunction with the recovery temperatures calculated from the post-process results of the film cooled engines to generate the following plot.

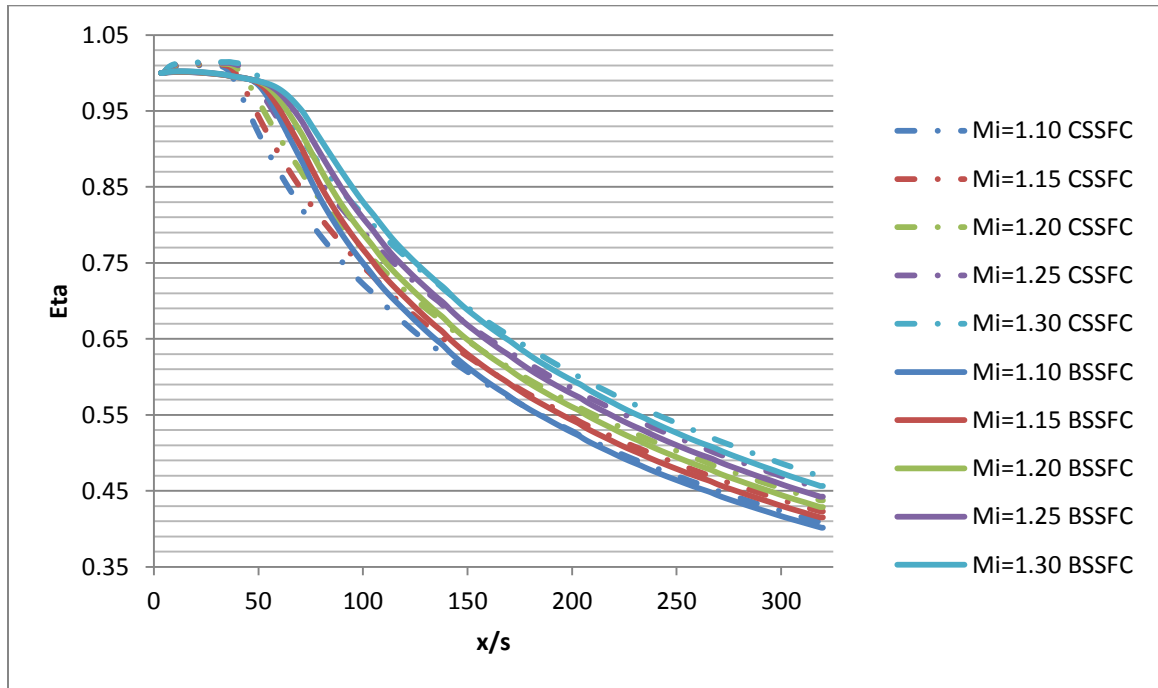


Figure 42: Biased flat plate film cooling effectiveness for CSSFC and BSSFC methods.

8.1.2 Biased Flat Plate Wall Temperature Reduction

Due to certain limitations of the film cooling effectiveness parameter, the temperature reduction analysis was conducted. The goal of the analysis was to demonstrate the change in wall temperature when the BSSFC method is implemented. The following plot was generated by calculating a wall temperature reduction in the form of a percentage via Microsoft Excel and the post-process wall temperature results.

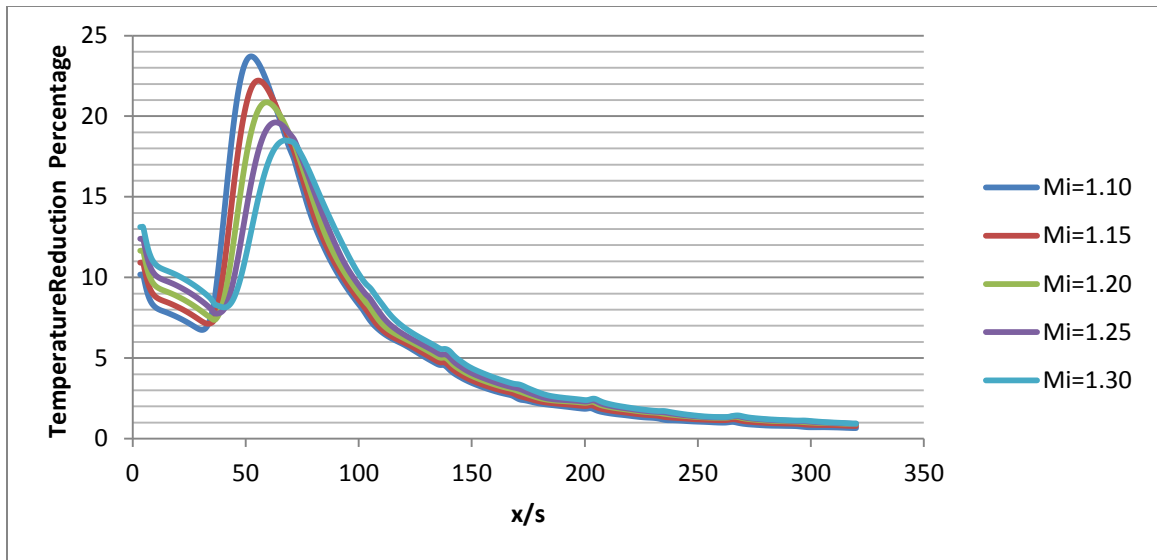


Figure 43: Biased flat plate wall temperature reduction percentage variation.

8.2 Modified Vulcain II Investigation

The modified Vulcain II film cooled nozzles, which are discussed in section 7.2, were subjected to both the CSSFC and BSSFC methods. The purpose of the numerical simulations was to obtain wall temperature data for each cooling method. The data was ultimately analyzed with the aid of Matlab and excel to produce temperature and film cooling plots for comparison purposes.

8.2.1 Modified Vulcain II Film Cooling Effectiveness

The film cooling plots provided in the following figures outline the conventional method, denoted by the dashed lines, and the biased film cooling method, highlighted by the solid curves. Each trial pair has been provided with identical colors to detail the BSSFC improvement over the CSSFC technique. For reference purposes, the model definitions were previously provided in Table 12.

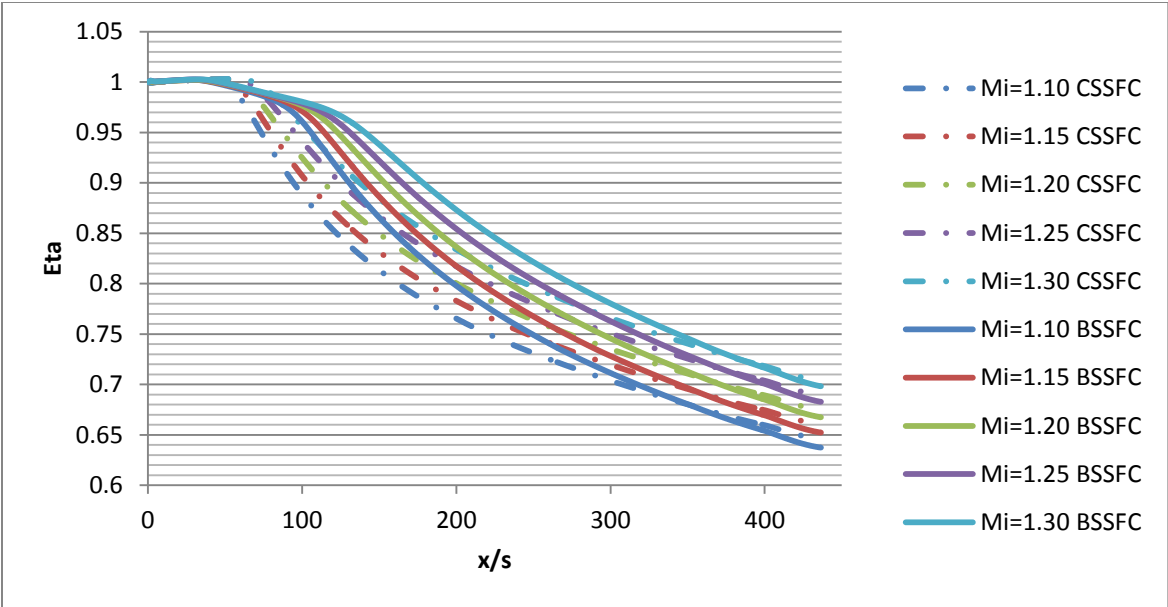


Figure 44: Model 'A' film cooling effectiveness comparisons.

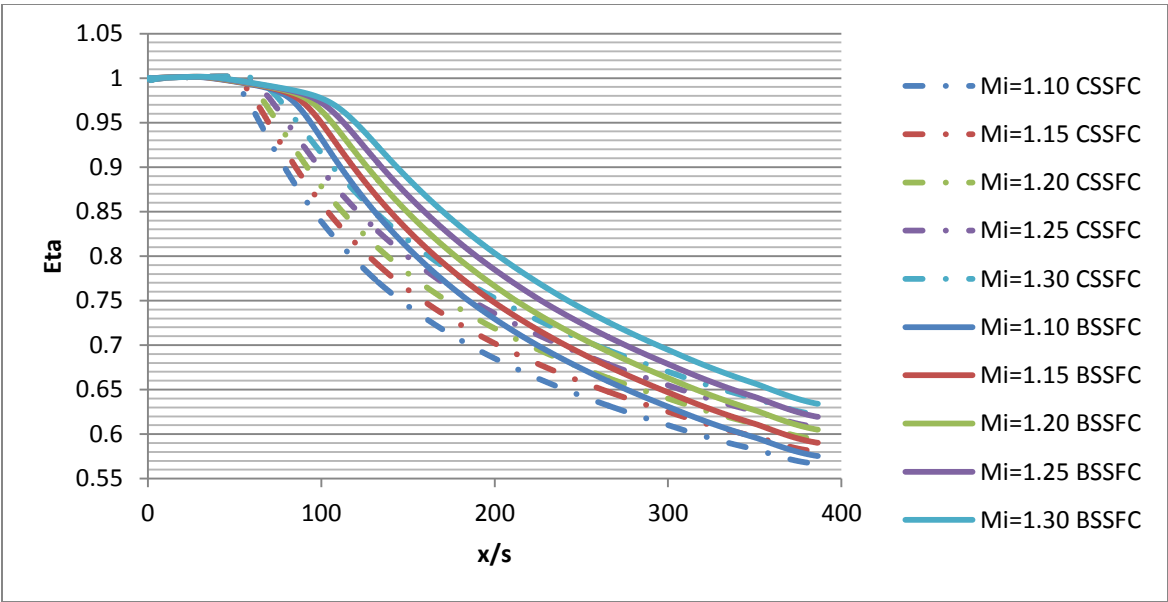


Figure 45: Model 'B' film cooling effectiveness comparisons.

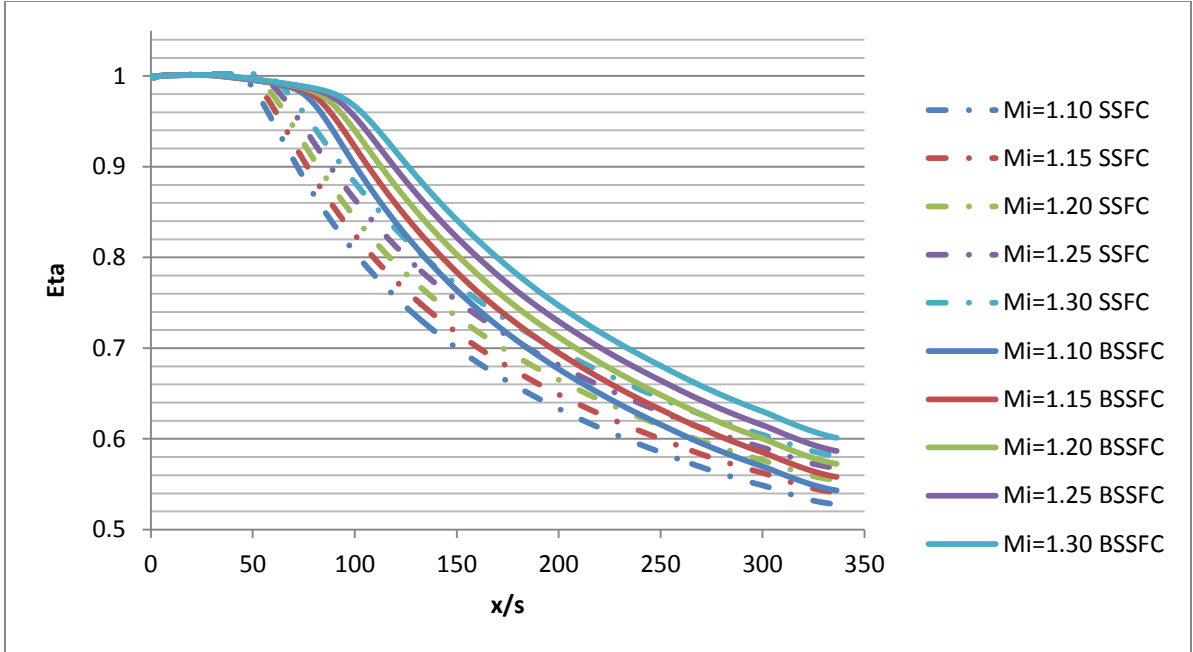


Figure 46: Model 'C' film cooling effectiveness comparisons.

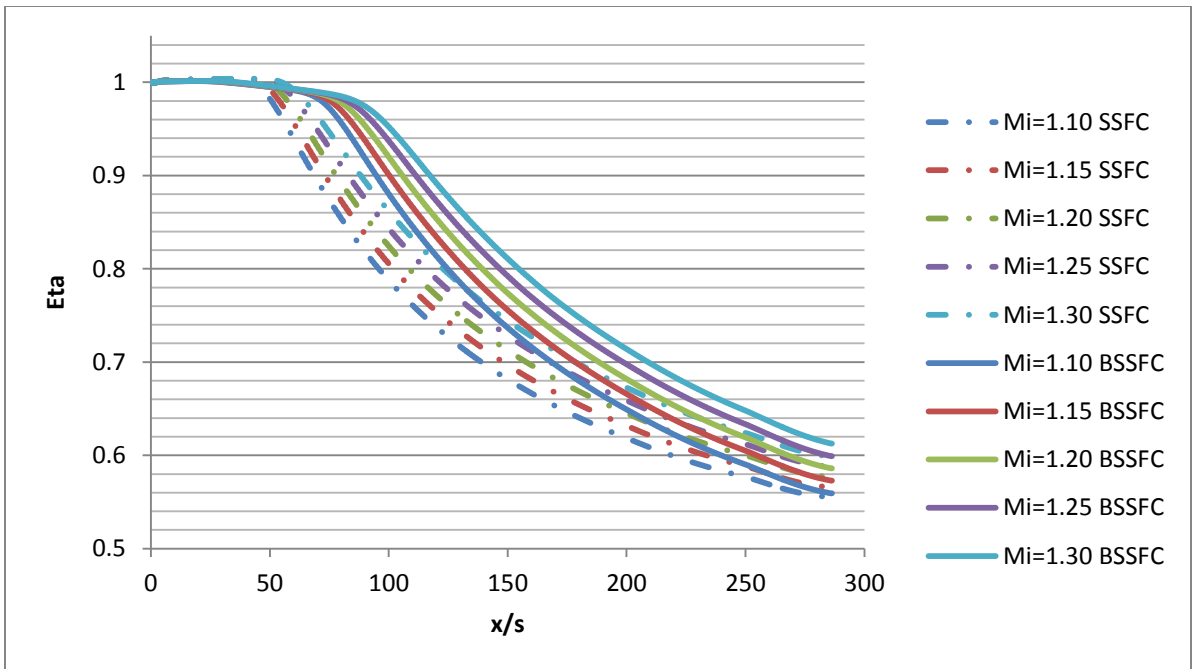


Figure 47: Model 'D' film cooling effectiveness comparisons.

8.2.2 Modified Vulcain II Wall Temperature Reduction

Due to the limitations of the film cooling effectiveness parameter, a series of temperature reduction plots were generated. These plots address the limitations of the film cooling effectiveness plots by demonstrating the reduction in wall temperature for the BSSFC method over the conventional technique as a percentage.

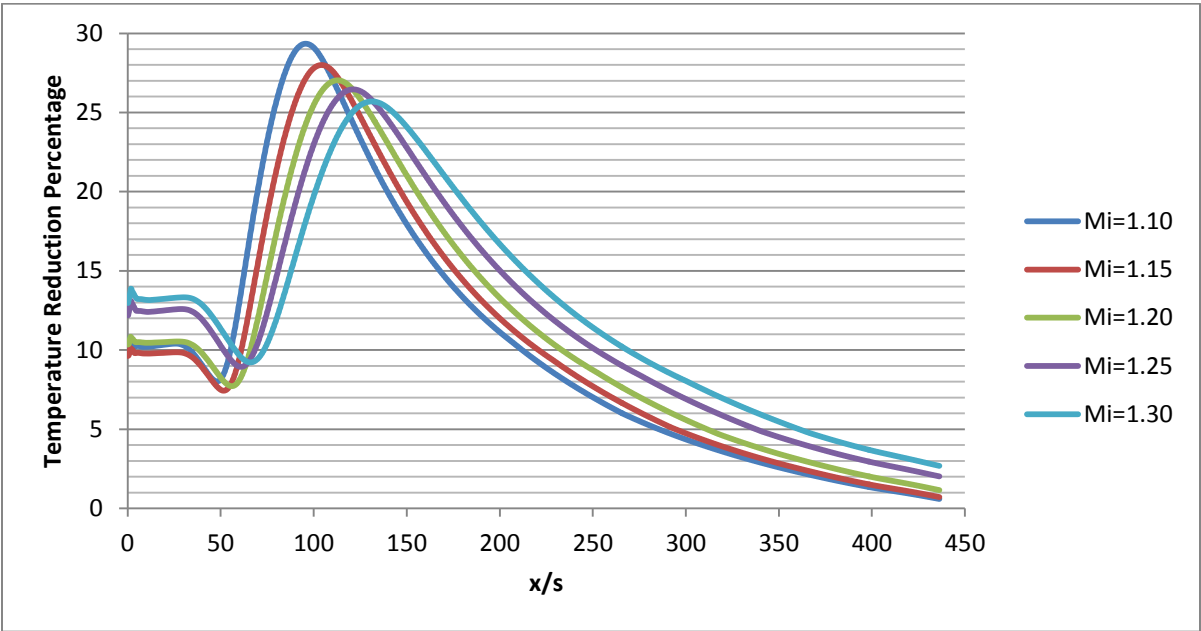


Figure 48: Model 'A' BSSFC wall temperature reduction.

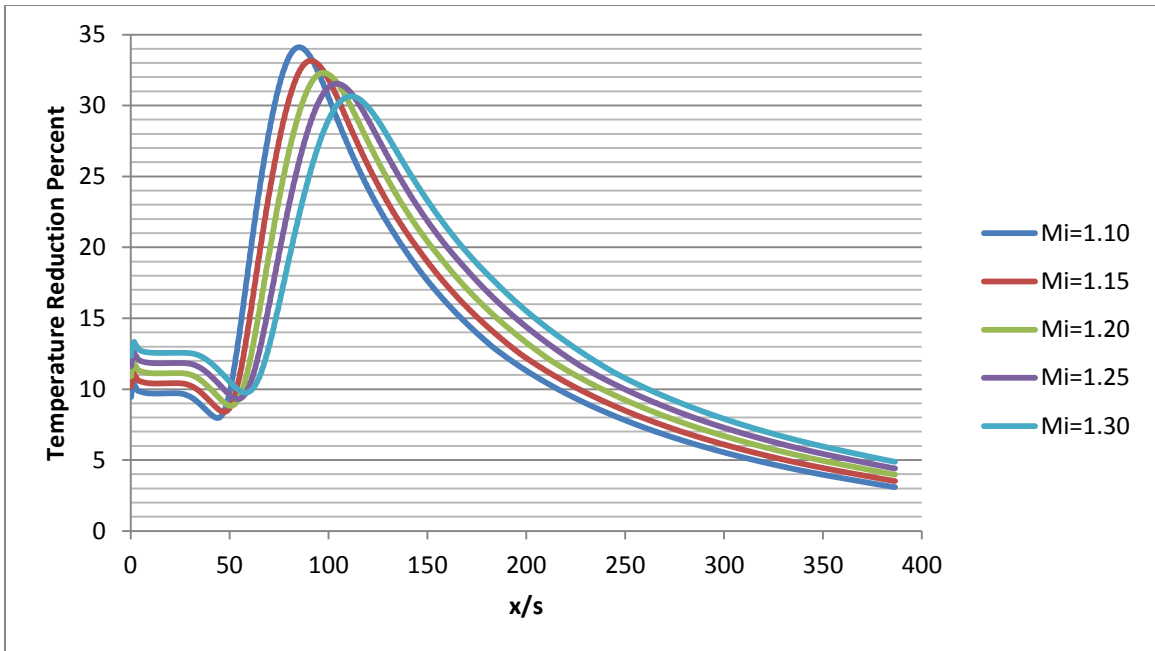


Figure 49: Model 'B' BSSFC wall temperature reduction.

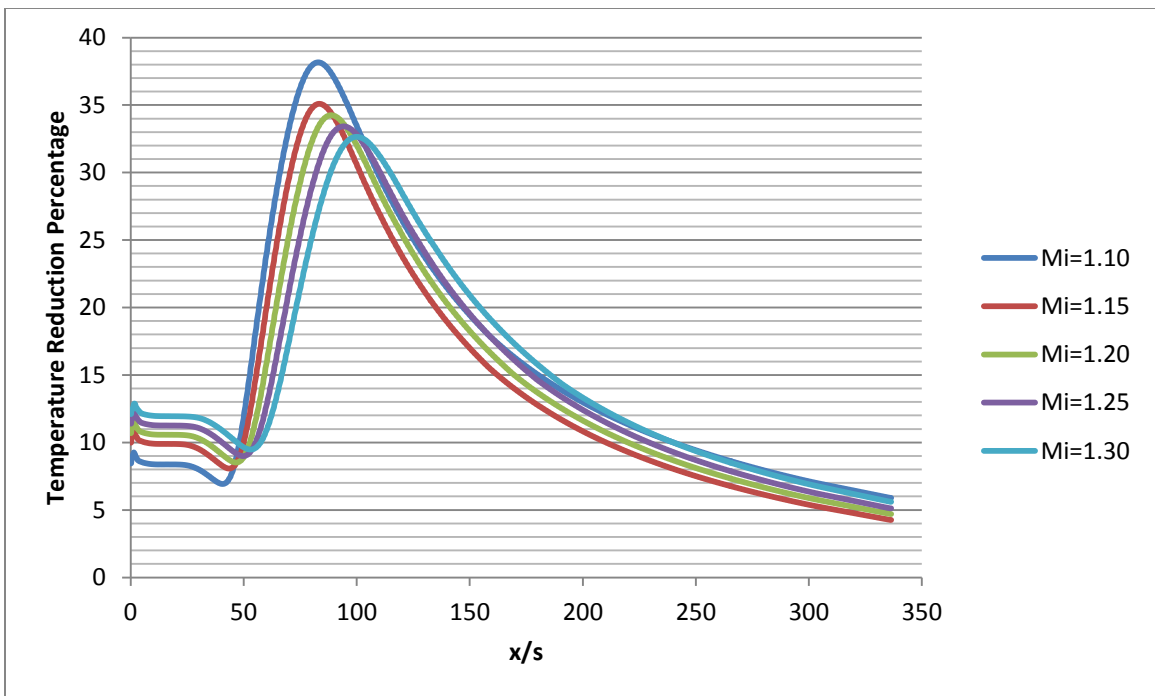


Figure 50: Model 'C' BSSFC wall temperature reduction.

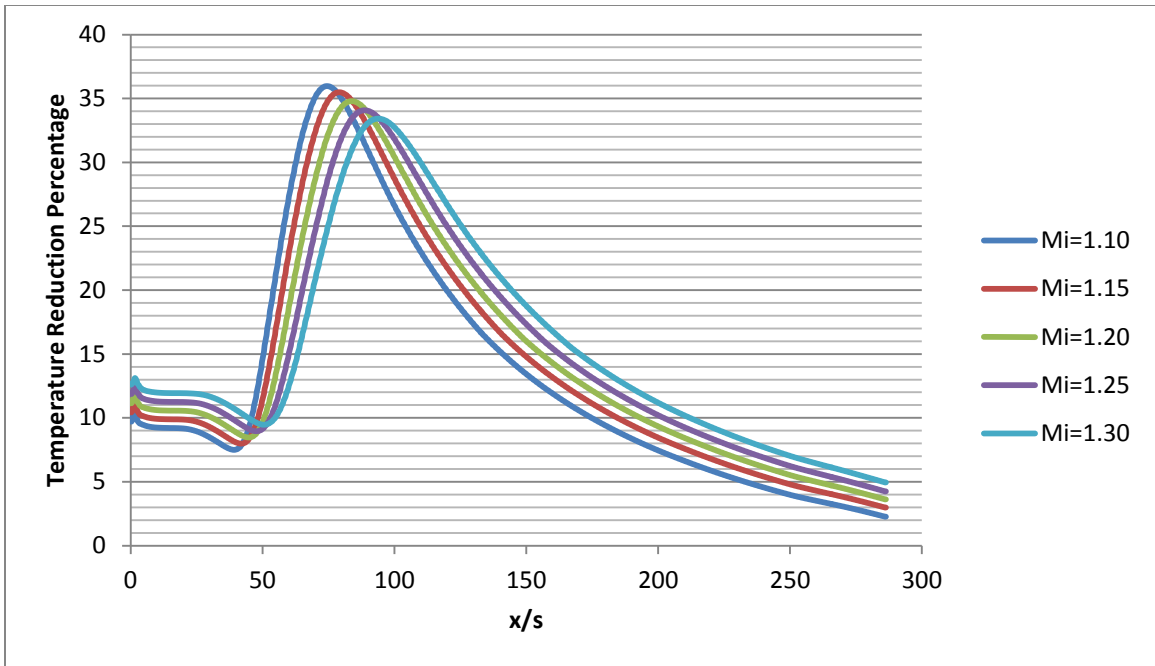


Figure 51: Model 'D' BSSFC wall temperature reduction.

Chapter 9: Discussion and Conclusion

9.1 Introduction

The following subsections explore the film cooling effectiveness data and wall temperature reductions obtained from the various simulations performed. The results were obtained from the ANSYS post processor, CFD-Post, and have been extracted and analyzed with the aid of Microsoft Excel and Matlab.

9.2 Film Cooling Effectiveness

The film cooling effectiveness was calculated for each model and used to evaluate the proposed cooling method. The 2D, axisymmetric, steady-state analysis of the two cooling methods indicates that there is a marked improvement in film cooling effectiveness when utilizing the BSSFC technique at slot-averaged Mach numbers ranging from 1.1 to 1.3. At higher slot Mach numbers, both film cooling methods begin to heat the boundary layer and do little to reduce wall temperatures. The reduced effect on wall temperature is not reflected in the film cooling effectiveness plots at high Mach numbers due to the manner in which the values are calculated.

The film cooling effectiveness parameter, η , is a function of the initial difference between the injection recovery temperature and the mainstream recovery temperature. This initial difference does not distinguish between heating or cooling effects. For example, a film that is approximately the same temperature as the mainstream will produce film cooling effectiveness values near unity along the wall. While the film effectiveness is high, the wall temperatures are affected little by the presence of the film. Conversely, if a film is injected at exceptionally low temperatures, the film cooling effectiveness values will rapidly diminish due to mixing yet the wall temperatures will be far lower than the mainstream temperatures. In short, the film cooling effectiveness parameter is a measure of the film's ability to

maintain the initial temperature difference and does not reflect the film's ability to alter the wall temperatures. This fact led to the development of the wall temperature reduction plots to ascertain the cooling characteristics of BSSFC method.

9.3 Wall Temperature Reduction

The reduction in wall temperature suggests that the BSSFC method cools the nozzle better than the conventional mixed injection process under the given parameters. At roughly seventy-five slot heights downstream of the film injection, the wall temperature reduction is significant with maximum values showing a 36% drop in wall temperature over the conventional method. On average, the BSSFC method reduces the wall temperatures by approximately 9%-15% depending on the model and injection Mach. In general, the results follow the same trends, but Model 'C' shows an above average spike in wall temperature reduction for a slot-averaged injection Mach of 1.1.

The Model 'C' trial of interest was run several times and the parameters of interest were double checked on multiple occasions. The reduction in wall temperature of 37% is far higher than the other trials for Model 'C'. It was reasoned that the film parameter ratios produced a favorable combination resulting in the reduction of the wall temperature by several additional percentage points.

9.4 Conclusion

An enhanced supersonic film cooling method for hydrogen-fueled, gas-generator cycle engines is proposed and investigated. The biased injection method leverages the high heat capacity and low viscosity of hydrogen to increase film cooling effectiveness and lower the wall temperatures in a nozzle extension. The BSSFC research was conducted in a series of four phases that obtained critical parameters, developed the best film cooling modeling practices, conducted an initial flat plate analysis, and applied both the CSSFC and BSSFC methods to a modified Vulcain II engine. The results of the four research phases indicate that the BSSFC method can improve the film cooling characteristics within the nozzle extension. Additional future research is required to improve the understanding of the limitations of the BSSFC method, investigate turbulence effects, and study three-dimensional mixing characteristics.

Chapter 10: Extension and Future Work

The research presented in the previous sections, while involved, did not fully investigate many aspects of BSSFC due to time constraints and computational limitations. The research outlined in this work can be considered an initial step in a broad area of research. Future research opportunities and investigations can build upon this initial step in numerous ways. The following subsections have been provided to describe areas of future BSSFC research.

10.1 Hydrocarbon Analysis

The film gases used throughout this work rely on the availability of hydrogen gases onboard a launch vehicle. While hydrogen fueled rockets have excellent propulsive efficiencies, only a select few launch vehicles utilize a hydrogen-oxygen combustion process. The vast majority of engines, due to economic, storage, and tank sizing issues, use a hydrocarbon fuel such as kerosene or RP-1. For supersonic film cooling to be a versatile cooling strategy, techniques must be developed with hydrocarbon fueled engines in mind. On paper such a proposal is relatively straightforward; however, the complex hydrocarbon combustion process coupled with the presence of soot particles and poor film qualities present hurdles that are not trivial to overcome.

10.2 Fluid-Structure Interactions

During engine operation, the nozzle of a rocket vibrates and shifts. The movement of the nozzle walls is particularly severe during the transient start-up of the engine when combustion first occurs. The fluctuations of the nozzle walls cause film gases to break apart and reduce overall cooling effectiveness. Performing a coupled fluid-structure analysis of the

engine start-up through steady state operation will provide valuable information regarding the wall temperature fluctuations. The wall temperature information can identify any potential critical heating regions within the engine.

10.3 Turbulence Effects

The mixing of binary gases and liquids is strongly dependent on the presence of turbulence and shearing effects. The work highlighted in the previous sections use moderate turbulence ratios that are believed to be conservative for rocket engine research. Therefore, any future research should incorporate reasonable turbulence values to study the mixing process and the effect on the cooling process.

References:

- [1] Smith-Strickland, K. (2013). *SpaceX President Gwynne Shotwell: The Case for Commercial Rockets*. Retrieved from <http://www.popularmechanics.com/science/space/news/spacex-president-gwynne-shotwell-the-case-for-commercial-rockets-15608331>
- [2] Kazan , C. (2010). *SpaceX Falcon 9 Rocket Launch: Signals Paradigm Shift to Private Space Era*. Retrieved from http://www.dailygalaxy.com/my_weblog/2010/02/spacex-falcon-9-rocket-launch-signals-pardigm-shift-to-private-space-ventureswill-be-test-of-commerc.html
- [3] Milstein, M. (2009). *NASA Makes Space U-Turn, Opening Arms to Private Industry*. Retrieved from <http://www.popularmechanics.com/science/space/4263233>
- [4] Rutan, B. (2007). *Burt Rutan: Entrepreneurs are the Future of Space Flight* [Video file]. Retrieved from <http://www.youtube.com/watch?v=nwfSEnkjJXY>
- [5] Greason, J. (2011). *Rocket Scientists: Making Space Pay* [Video file]. Retrieved from <http://www.youtube.com/watch?v=m8PlzDgFQMM>
- [6] Engines Ltd., R. (2011). *Space Access: Skylon*. Retrieved from http://www.reactionengines.co.uk/space_skylon.html
- [7] Mossman, J. B., & Perkins, D. R. (2001). Rocket Propulsion Technology Impact on TSTO Launch System Costs. U.S. Department of Defense, Air Force Research Laboratory. Retrieved from website: <http://www.nss.org/settlement/manufacturing/SM13.193.TSTOLaunchSystem.pdf>
- [8] Sponable, J. M. (1995). Assessing Single Stage to Orbit Feasibility. *ALAA 31st Joint Propulsion Conference and Exhibit*. doi:10.2514/6.1995-3004.
- [9] Goo, S. D. (1995). Boeing Approach to Evolved Expendable Launch Vehicles. *ALAA Space Programs and Technologies Conference*. doi:10.2514/6.1995-3670.
- [10] Buzzalto, J. L. (2003). The Transition of Space Launch – Heritage to EELV. *ALAA Space Conference and Exposition*. doi:10.2514/6.2003-6408.
- [11] Huether, J. (1995). Space Transportation Affordability. *ALAA Space Programs and Technologies Conference*. doi:10.2514/6.1995-3530.
- [12] Capps, S. (1995). Achieving Low Cost Access to Space: A Leveraged Commercial Approach. *ALAA Space Programs and Technologies Conference*. doi:10.2514/6.1995-3526
- [13] Caluori, V. A. (1993). Reusability – The Key to Launch System Effectiveness. *ALAA Space Programs and Technologies Conference and Exhibit*. doi: 10.2514/6.1993-4126
- [14] Schindler, C.M. (1990). Engine Costs for Reusability. *ALAA Joint Propulsion Conference and Exhibit*. doi:10.2514/1990-2689.

- [15] Borromee, J. Future European Reusable Propulsion Systems. Retrieved from http://rocket-propulsion.info/resources/articles/Eur_lpre_evolution.pdf
- [16] Gannon, M. (2013). Incredible Technology: How to Make Reusable Rockets for Cheap Space Travel. Retrieved from <http://www.space.com/22470-reusable-rocket-launches-incredible-technology.html>
- [17] Schindler, C.M.(2006). Cost Estimates of Near-Term, Fully-Reusable Space Access Systems. *ALAA Space Conference and Exhibition*. doi: 10.2514/6.2006-7209
- [18] Sutton, G. (2006). *History of Liquid Propellant Rocket Engines*-. Reston, Virginia: American Institute of Aeronautics and Astronautics.
- [19] Reynolds, J., Nesman, M. (2000). Liquid Propellant Rocket Engine Cost Model Update, Model Description, Boeing – Rocketdyne Propulsion and Power, RD00-280, Contract 4400030067 Science Applications International Corporation.
- [20] Sutton, G., & Biblarz, O. (2001). *Rocket Propulsion Elements*. (7th ed.). New York, NY: John Wiley and Sons.
- [21] Kirkman, M. (2008, July 27). *Space Shuttle Systems 101*. Retrieved from <http://www.interspacenews.com/FeatureArticle/tabid/130/Default.aspx?id=2130>
- [22] Humble, R., Henry, G., & Larson, W. (1995). *Space Propulsion Analysis and Design*. New York City: McGraw-Hill.
- [23] Minami, H. M. (1991). Atlas Engines – A History. *ALAA Joint Propulsion Conference and Exhibit*. doi:10.2514/6.1991-1943.
- [24] Meland, L. C., & Thompson F.C. (1989). History of the Titan Liquid Rocket Engines. *ALAA Joint Propulsion Conference and Exhibit*. doi: 10.2514/6.1989-2389.
- [25] Winter, F. H. (2003). On the Spaghetti Trail: The Story of a Revolution in Modern Rocket Technology. *54th International Astronautical Federation (IAF) Congress*. Paper: IAC-03-IAA.2.3.02
- [26] Clary, D. (2003). *Rocket Man: Robert Goddard and the Birth of the Space Age*. New York, NY: Hyperion Books.
- [27] Zakkay, V., L. Sakell, and K. Parthasarathy, "An Experimental Investigation of Supersonic Slot Cooling," Proceedings of 1970 Heat Transfer and Fluid Mechanics Institute, edited by T. Sarpkaya, Stanford University Press, Stanford, Ca. pp. 88-103.
- [28] *Innovative Nozzle Cooling*. (2001). Retrieved from http://www.volvogroup.com/group/global/en-gb/researchandtechnology/technology_award/2001/Pages/2001.aspx

- [29] Rosengren, L. (2001). *Stmnt re - Technology Prize*. Retrieved from <http://www.investigate.co.uk/article.aspx?id=200104260705126120C>
- [30] *Volvo Aero in Collaboration with PWR and NASA*. (2006). Retrieved from <http://www.businesswire.com/news/home/20061214005343/en/Volvo-Aero-Collaboration-PWR-NASA-Return-Moon>
- [31] *500 Second J-2X Test at Stennis Space Center*. (2011). Retrieved from <http://rocketry.wordpress.com/2011/11/11/500-second-j-2x-test-at-stennis-space-center/>
- [32] Dellimore, K. (2010). *Modeling and Simulation of Mixing Layer Flows for Rocket Engine Film Cooling*. (Doctoral dissertation, University of Maryland).
- [33] Suslov, D., Arnold, R., Haidn, J. (2010). Convective and Film Cooled Nozzle Extension for a High Pressure Rocket Subscale Combustion Chamber. *48th ALAA Aerospace Sciences Meeting*. doi: 10.2514/6.1010-1150.
- [34] Mizoguchi, M., Aso, S., Tani, Y. (2009). Influence of Coolant Gas Properties on Film Cooling Effectiveness in High Enthalpy Flows. *47th ALAA Aerospace Sciences Meeting*. doi: 10.2514/6.2009-1034.
- [35] McDonel, J., Eiswerth, J. (1977). Measured Effects of Film Injection on the Performance of a Cooled Turbine. *13th ALAA Propulsion Conference*. doi: 10.2514/6.1977-946.
- [36] Knuth, E. (1954). *The Mechanics of Film Cooling*. (Doctoral dissertation, California Institute of Technology).
- [37] El-Gabry, L., Heidmann, J., & Ameri, A. (2009). Numerical Analysis of Film Cooling at High Blowing Ratio. NASA/TM-2009-215517.
- [38] *Saturn V News Reference*. (1968). United States: Retrieved from http://history.msfc.nasa.gov/saturn_apollo/documents/F-1_Engine.pdf
- [39] Goldstein, R. J. (1971) Film Cooling. *Advances in Heat Transfer*, 7:321-379.
- [40] Tribus, M., Klein, J. (1953). Forced Convection from Non-Isothermal Surfaces. Heat Transfer, a Symposium, University of Michigan, Ann Arbor.
- [41] Simoneau, R. J., Hendricks, R. C., & Gladden, H. J. (1988) Heat Transfer in Aerospace Propulsion. *Proceedings of ASME National Heat Transfer Conference* (Houston, Tx), Vol. 3.
- [42] Seban, R.A., Back, L.H., "Velocity and Temperature Profiles in a Wall Jet," Int. J. Heat Mass Transfer, Vol. 3, pp. 255-265, 1961.
- [43] Oates, G. (1985). *ALAA Education Series: Aerothermodynamics of Aircraft Engine Components*. New York, NY: American Institute of Aeronautics and Astronautics, Inc.

- [44] Dailey, G. (2000). *Design and Calculation Issues, Aero-Thermal Performance of Internal Cooling Systems in Turbomachinery*, VKI, Belgium. Retrieved from <http://gtt.epfl.ch/page-63563-fr.html>
- [45] Smith, A.C., Hatchett, J.H., Nix, A.C., Ng, W.F., Thole, K.A., & Cunha, F.J. (2004). Effectiveness of Normal and Angled Slot Cooling. *ASME*. GT2004-53248.
- [46] “NASA Space Vehicle Design Criteria: Liquid Rocket Engine Nozzles (SP-8120),” July 1976. Retrieved from <http://ntrs.nasa.gov/archive/nasa/casi.ntrs.nasa.gov/19770009165.pdf>
- [47] Bruce-Black, J. Johns, D. Davidson, F., & Bogard, D.(2010). Practical Slot Configurations for Turbine Film Cooling Applications. *Journal of Turbomachinery*, 133(3), 031020.
- [48] Komori, S. (2008). *Environmental Fluids and Thermal Engineering Lab: Mixing layer flow*. Retrieved from <http://www.fluid.me.kyoto-u.ac.jp/english/study/mixing.html>
- [49] Kestin, J. and Wood, R. T. (1970). The Mechanism which Causes Free-Stream Turbulence to Enhance Stagnation Line Heat and Mass Transfer. *Heat Transfer*, Vol. 2, Elsevier, Amsterdam.
- [50] Karlsson, R.I., Eriksson, J. & Persson, J. (1993). An Experimental Study of a Two-Dimensional Plane Turbulent Wall Jet. *Vattenfall Utveckling AB, 1993-12-30*.
- [51] Birch, S. F. (1997). On the Role of Structure in Turbulent Mixing. *33rd AIAA Joint Propulsion Conference and Exhibit*. doi: 10.2514/6.1997-2636.
- [52] Vreman, A. W. (1995). Direct and Large-Eddy Simulation of the Compressible Turbulent Mixing Layer. Ph.D. Thesis, University of Twente, Twente, Netherlands.
- [53] Hatch, J.E., & Papell, S. (1959). “Use of a Theoretical Flow Model to Correlate Data for Film Cooling or Heating an Adiabatic Wall by Tangential Injection of Gases of Different Fluid Properties. NASA Technical Note D-130.
- [54] Papell, S. (1960). Effect on Gaseous Film Cooling of Coolant Injection Through Angled Slots and Non-trivial Holes. NASA Technical Note D-299.
- [55] Hartnett, J., Birkebak, R., & Eckert, E. (1961). Velocity Distributions, Temperature Distributions, Effectiveness and Heat Transfer for Air Injected Through a Tangential Slot into a Turbulent Boundary Layer,” *Transactions of ASME Journal of Heat Transfer*, Vol. 83, p. 293–306.
- [56] Simon, F., “Jet Model for Slot Film Cooling with Effect of Free-stream and Coolant Turbulence,” NASA TP-2655, October 1986.

- [57] Channapragada, R. (1963). Compressible Jet Spread Parameter for Mixing Zone Analysis. *ALAA Journal*. Vol. 1:2188-2190. doi: 10.2514/3.2037.
- [58] Volchkov, E., Kutateladze, S., & Leontev, A. (1966). Effect of Compressibility and Nonisothermicity on the Efficiency of Film Cooling in a Turbulent Boundary Layer. *Journal of Applied Mechanics and Technical Physics*, Vol. 7, No. 4, p. 93–94.
- [59] Repukhov, V. (1970). Effects of Compressibility and Non-isothermal Conditions on the Performance of Film Cooling. *Journal of Engineering Physics and Thermophysics*, Vol. 19, No. 5, p.1401–1408.
- [60] Pedersen, D., Eckert, E., & Goldstein, R. (1977). Film Cooling with Large Density Differences between the Mainstream and the Secondary Fluid Measured by the Heat-Mass Transfer Analogy. *Transactions of ASME Journal of Heat Transfer*, Vol. 99, 620–627.
- [61] Hansmann, T., Wilhelmi, H., & Bohn, D. (1993). An Experimental Investigation of the Film-Cooling Process at High Temperatures and Velocities. *5th International Aerospace Planes and Hypersonics Technologies Conference*. doi: 10.2514/6.1993-5062.
- [62] Papell, S., & Trout, A. (1959). Experimental Investigation of Air Film Cooling Applied to an Adiabatic Wall by Means of an Axially Discharging Slot. NASA TN D-9.
- [63] Hartnett, J., Birkebak, R., & Eckert, E. (1961). Velocity Distributions, Temperature Distributions, Effectiveness and Heat Transfer for Air Injected Through a Tangential Slot into a Turbulent Boundary Layer. *Transactions of ASME Journal of Heat Transfer*, Vol. 83, p. 293–306.
- [64] Juhasz, A., & Marek, C. (1971). Combustor Liner Film Cooling in the Presence of High Free Stream Turbulence. NASA TN D-6360.
- [65] Lebedev, V., Lemanov, V, Misyura, S., & Terekhov, V. (1991). Effects from Turbulence Intensity on Slot Protection Performance. *Journal of Applied Mechanics and Technical Physics*, Vol. 32, p. 360–364.
- [66] Juhany, K. A., Hunt, M.L., & Sivo, J.M. (1994). Influence of Injectant Mach Number and Temperature on Supersonic Film Cooling. *ALAA Journal of Thermophysics and Heat Transfer*, Vol. 8: 59-67. doi: 10.2514/3.501.
- [67] Lessen, M., Fox, J. A., & Zien, M. (1966). Stability of the Laminar Mixing of Two Parallel Streams with Respect to Supersonic Disturbances. *Journal of Fluid Mechanics*, Vol. 25, Part 4, 737–742.
- [68] Chalot, F., Marquez, B., Ravachol, M., Ducros, F., & Poinso, T. (1999). Large Eddy Simulation of a Compressible Mixing Layer: Study of the Mixing Enhancement. *14th Computational Fluid Dynamics Conference*. doi: 10.2514/6.1999-3358.

- [69] Sandham, N. D., & Reynolds, S. W. (1991). Three-dimensional Simulations of Large Eddies in the Compressible Mixing Layer. *Journal of Fluid Mechanics*, Vol. 224, p. 133–158.
- [70] Sarkar, S. (1995). The Stabilizing Effect of Compressibility in Turbulent Shear Flows. *Journal of Fluid Mechanics*, Vol. 282, p. 163–186.
- [71] Cleland, D., Gallagher, J., & Whitehead, R. (1993). *Military Project Management Handbook*. New York, NY: McGraw-Hill.
- [72] Goldstein, R. J., Eckert, E. R. G., Tsou, F. K., & Haji-Sheikh, A. (1966). Film Cooling with Air and Helium Injection Through a Rearward-Facing Slot into a Supersonic Air Flow. *ALAA Journal*, Vol. 4, No. 6, p. 981-985.
- [73] Cary, A. M., & Hefner, J. N. (1970). Film Cooling Effectiveness in Hypersonic Turbulent Flow. *ALAA Journal*, Vol. 8, No. 11, p. 2090, 2091.
- [74] Cary, A. M., & Hefner, J. N. (1972). Film-Cooling Effectiveness and Skin Friction in Hypersonic Turbulent Flow. *ALAA Journal*, Vol. 10, No. 9, p. 1188-1193.
- [75] Rousar, D. C., & Ewen, R. L. (1973). Hydrogen Film Cooling Investigation. NASA CR 121235.
- [76] *Getedata Graph Digitizer*. (2013). Retrieved from <http://www.getdata-graph-digitizer.com/index.php>
- [77] *ANSYS Fluent Theory Guide 14.5* (2012). United States: ANSYS, Inc. Retrieved from http://www.mecheng.osu.edu/documentation/Fluent14.5/145/flu_th.pdf
- [78] Eury, S., Gastal, J., Borromee, J. (1990) Development Status of the Vulcain Engine. 26th *ALAA Joint Propulsion Conference*. doi: 10.2514/6.1990-2251.
- [79] Lions, J. (1996). *Ariane 5 - Flight 501 Failure*. Paris, France: Retrieved from <http://www.di.unito.it/~damiani/ariane5rep.html>
- [80] *Safran Aerospace: Vulcain 2*. (2009). Retrieved from <http://www.safran-group.com/site-safran-en/aerospace/aerospace-propulsion/space-engines/vulcain-r-2/>
- [81] *Vulcain 2 Thrust Chamber* [Brochure]. (2008) Munich, Germany: Astrium Space Transportation. Retrieved from <http://cs.astrium.eads.net/sp/brochures/launcher-propulsion/Vulcain2.pdf>
- [82] Haidn, O. (2008). *Advanced Rocket Engines*. Lampoldshausen, Germany: Institute of Space Propulsion, German Aerospace Center (DLR). Retrieved from <http://ftp.rta.nato.int/public/PubFullText/RTO/EN/RTO-EN-AVT-150/EN-AVT-150-06.pdf>

- [83] Coulon, D. (2000) *Vulcain-2 Crogenic Engine Passes First Test with New Nozzle Extension* [Brochure]. Paris, France: Astrium Space Transportation. Retrieved from <http://www.esa.int/esapub/bulletin/bullet102/Coulon102.pdf>
- [84] Holmedahl, K. "Analysis and Testing of the Vulcain 2 Lox Turbine Blades for Prediction of High Cycle Fatigue Life," AIAA Joint Propulsion Conference and Exhibit, July 2000.
- [85] *Vulcain 2* [Brochure]. (2011) Evry Cedex, France: Safran/ Snecma. Retrieved from http://www.snecma.com/IMG/files/fiche_vulcain2_2012_modulvoir_file_fr.pdf
- [86] Olson, B. (2009). *2-D Nozzle Design*. Informally published manuscript, Department of Aerospace Engineering, Stanford University, Retrieved from <http://www.mathworks.com/matlabcentral/fileexchange/14682-2-d-nozzle-design>
- [87] *Vulcain 2 Rocket Engine - Thrust Chamber*. (2013). Retrieved from <http://cs.astrium.eads.net/sp/launcher-propulsion/rocket-engines/vulcain-2-rocket-engine.html>
- [88] Space Daily. (2006). *Volvo Aero Components Powering Large Number of Ariane 5 Launches*. Retrieved from http://www.spacedaily.com/reports/Volvo_Aero_Components_Powering_Large_Number_Of_Ariane_5_Launches.html
- [89] Space Images. (1998). *Vulcain MK2 Engine for Ariane 5E*. Retrieved from http://www.esa.int/spaceinimages/Images/1998/01/Vulcain_Mk2_engine_for_Ariane_5E_1998
- [90] Snecma. (2011). *Vulcain2 / HM7B*. Retrieved from <http://www.snecma.com/-vulcain-2-.html?lang=en>
- [91] Volvo. (2013). *Volvo aerospace - Important Supplied for the Aerospace Industry*. Retrieved from <http://nordicspace.net/wp-content/uploads/2013/07/NSA141.pdf>
- [92] Herteman, J. (2006). *European Space Propulsion Facing a Technical Challenge*. Retrieved from http://www.belspo.be/belspo/eisc/pdf/docu_eisc_semi/Herteman.pdf
- [93] François, L., Chopinet, J., Fayolle, P., & Verplancke, C. (2009). *Vulcain X Technological Demonstration Roadmap. 45th AIAA Joint Propulsion Conference and Exhibit*. doi: 2514/6.2009-4947
- [94] SAE International. (2009). *Volvo Aero Signs Nozzle/Turbine Supply Agreement*. Retrieved from <http://articles.sae.org/6658/>
- [95] Twist, J. (2004). *Super-Rocket Aims for January*. Retrieved from <http://news.bbc.co.uk/2/hi/science/nature/4054329.stm>

- [96] Knab, O., Frey, M., Gorgen, J., Maeding, C., Quering, K., & Wiedmann, D. (2009). Progress in Combustion Chamber and Heat Transfer Modeling in Rocket Thrust Chamber Applied Engineering. *45th AIAA Joint Propulsion Conference and Exhibit*. doi: 2514/6.2009-5477.
- [97] Moore, A. (1967). The Transonic Flow in the Throat Region of a Two-Dimensional Nozzle with Walls of Arbitrary Smooth Profile. *Ministry of Technology*. R.&M. No. 3481.
- [98] Astrium. (2006). *Vulcain Rocket Engine - Thrust Chamber*. Retrieved from <http://cs.astrium.eads.net/sp/launcher-propulsion/rocket-engines/vulcain-rocket-engine.html>
- [99] Oefelein, J. C., & Sankaran, R. U.S. Department of Energy, Office of Science. (2011). *High-Fidelity Large Eddy Simulation of Combustion for Propulsion and Power*. Retrieved from website: http://www.mcs.anl.gov/uploads/cels/papers/scidac11/final/Oefelein_Joseph.pdf
- [100] Gordon, S., & McBride, B. (1994). *Program for Calculation of Complex Chemical Equilibrium Composition and Applications (NASA Reference Publication 1311)*. Retrieved from <http://www.grc.nasa.gov/WWW/CEAWeb/ceaHome.htm>
- [101] Saxena, S. (1970). Transport Properties of Gases and Gaseous Mixtures at High Temperatures. *High Temperature Science* 3,168-188.
- [102] McBride, B., Gordon, S., & Reno, M. (1993). Coefficients for Calculating Thermodynamic and Transport Properties of Individual Species. NASA Technical Memorandum 4513.
- [103] Gordon, S., McBride, B., and Zeleznik, F., "Computer Program for Calculation of Complex Chemical Equilibrium Compositions and Application, Supplement I-Transport Properties," NASA TM-86885, 1984
- [104] Svehla, R. (1995). Transport Coefficients for the NASA Lewis Chemical Equilibrium Program. NASA Technical Memorandum 4647.
- [105] Anerson, J. (2006). *Hypersonic Aerodynamics and High Temperature Gas Dynamics*. (2nd ed.). Reston, Virginia: American Institute of Aeronautics and Astronautics, Inc.
- [106] B. Guillot. A reappraisal of what we have learnt during three decades of computer simulations on water. *Journal of Molecular Liquids*, 101(1-3):219{260, 2002.
- [107] Macrossan, M. (2006). *Scaling Parameters in Rarefied Flow: Breakdown of the Navier-Stokes Equations*. Informally published manuscript, Mechanical Engineering, Department, University of Queensland.

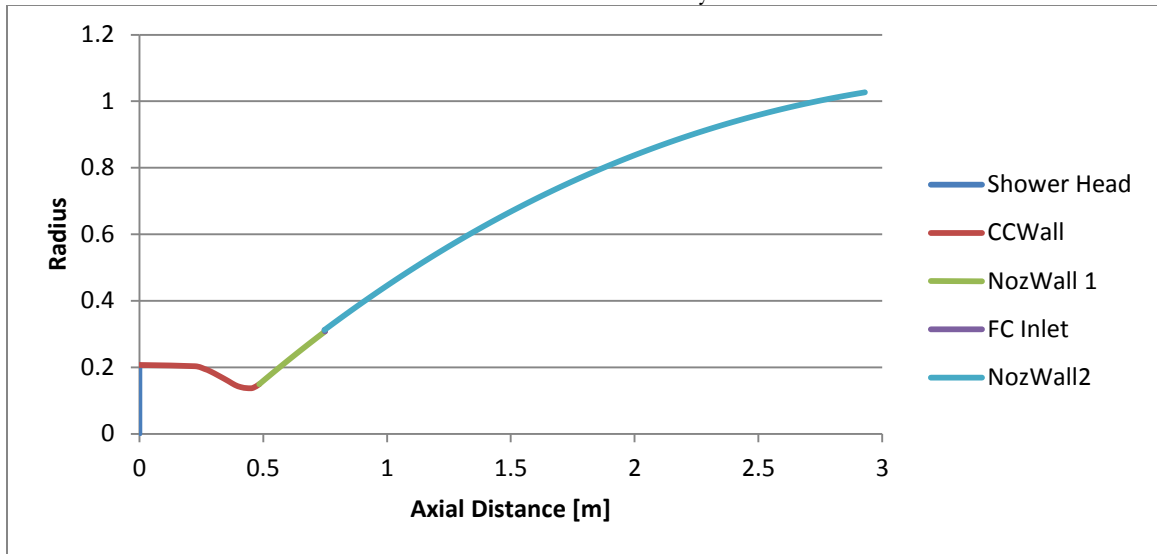
Appendix:

A) Engine Coordinates and Contours

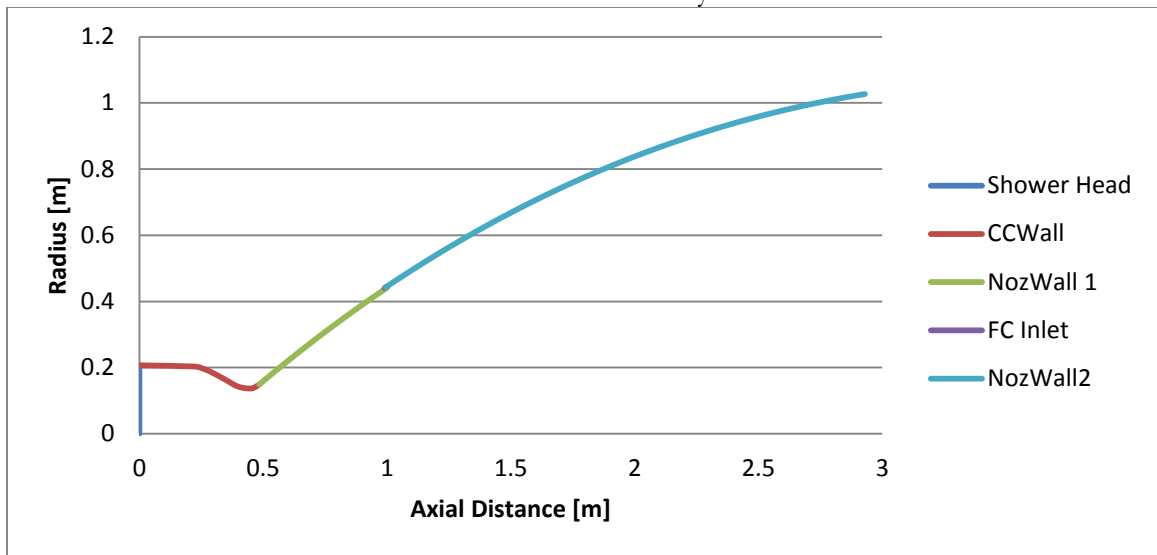
Default Coordinates		Model A Coordinates		Model B Coordinates	
X [m]	Radius [m]	X [m]	Radius [m]	X [m]	Radius [m]
0.000	0.000	0.000	0.000	0.000	0.000
0.000	0.207	0.000	0.207	0.000	0.207
0.225	0.203	0.225	0.203	0.225	0.203
0.262	0.195	0.262	0.195	0.262	0.195
0.287	0.188	0.287	0.188	0.287	0.188
0.320	0.175	0.320	0.175	0.320	0.175
0.360	0.158	0.360	0.158	0.360	0.158
0.386	0.147	0.386	0.147	0.386	0.147
0.410	0.140	0.410	0.140	0.410	0.140
0.435	0.137	0.435	0.137	0.435	0.137
0.459	0.138	0.459	0.138	0.459	0.138
0.484	0.149	0.484	0.149	0.500	0.159
0.500	0.159	0.750	0.308	0.750	0.308
0.750	0.308	0.748	0.312	1.000	0.442
1.000	0.442	1.000	0.446	0.998	0.446
1.250	0.561	1.250	0.564	1.250	0.565
1.500	0.666	1.500	0.668	1.500	0.669
1.750	0.757	1.750	0.759	1.750	0.760
2.000	0.836	2.000	0.838	2.000	0.839
2.250	0.902	2.250	0.904	2.250	0.905
2.500	0.957	2.500	0.959	2.500	0.959
2.750	1.000	2.750	1.002	2.750	1.003
2.930	1.025	2.930	1.027	2.930	1.028

Model C Coordinates		Model D Coordinates	
X [m]	Radius [m]	X [m]	Radius [m]
0.000	0.000	0.000	0.000
0.000	0.207	0.000	0.207
0.225	0.203	0.225	0.203
0.262	0.195	0.262	0.195
0.287	0.188	0.287	0.188
0.320	0.175	0.320	0.175
0.360	0.158	0.360	0.158
0.386	0.147	0.386	0.147
0.410	0.140	0.410	0.140
0.435	0.137	0.435	0.137
0.459	0.138	0.459	0.138
0.500	0.159	0.500	0.159
0.750	0.308	0.750	0.308
1.000	0.442	1.000	0.442
1.250	0.561	1.250	0.561
1.248	0.565	1.500	0.666
1.500	0.670	1.498	0.670
1.750	0.761	1.750	0.762
2.000	0.839	2.000	0.840
2.250	0.906	2.250	0.906
2.500	0.960	2.500	0.961
2.750	1.003	2.750	1.004
2.930	1.028	2.930	1.029

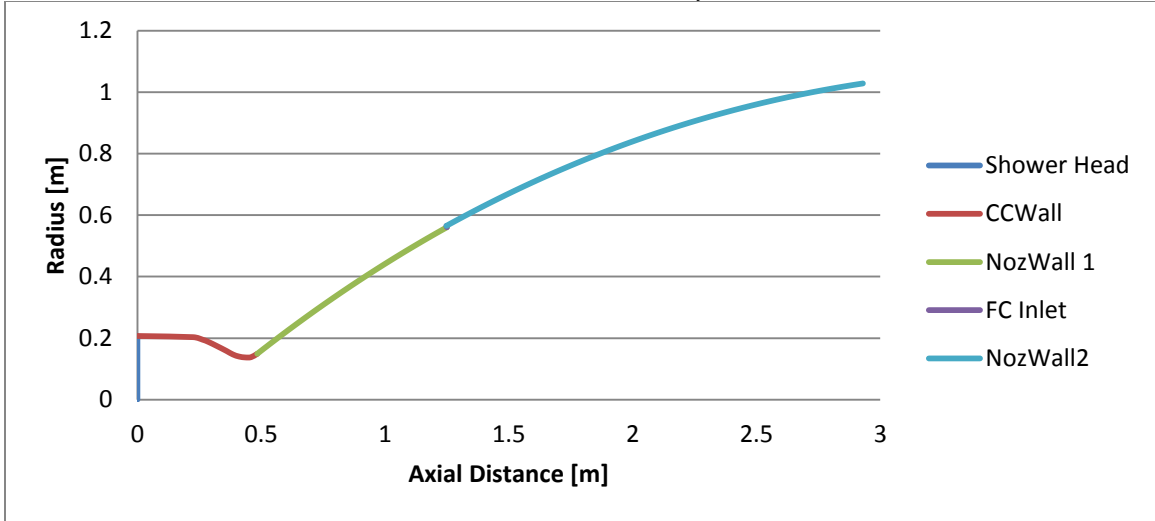
Model 'A' Geometry



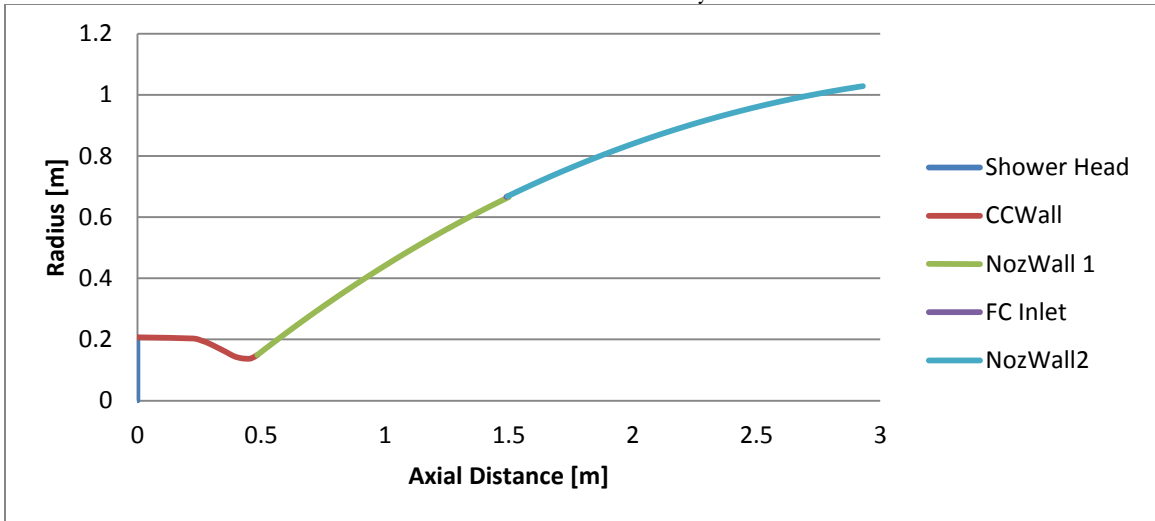
Model 'B' Geometry



Model 'C' Geometry



Model 'D' Geometry



B) Tabulated CEA Results

Area Ratio	Area [m ²]	Temperature [K]	Pressure [Bar]	C _p (T) [J/kgK]	Molecular Weight
CC	N/a	3628	112.05	9066.7	14.645
1	0.059	3436.5	66.255	8614.7	14.812
2	0.118	2965.67	15.096	6717.7	15.228
3	0.177	2783.92	8.3864	5792	15.359
4	0.236	2659.46	5.6351	5176.7	15.431
5	0.295	2563.31	4.1661	4743.2	15.477
10	0.59	2261.41	1.6606	3747	15.565
15	0.885	2084.55	0.97595	3410.5	15.588
20	1.18	1961.52	0.67042	3251.4	15.596
25	1.475	1868.43	0.50139	3158.3	15.599
30	1.77	1794.21	0.39561	3095.6	15.601
35	2.065	1732.88	0.32387	3049	15.601
40	2.36	1680.83	0.27237	3012	15.602
45	2.655	1635.78	0.23381	2981.3	15.602
50	2.95	1596.14	0.20397	2954.8	15.602
55	3.245	1560.86	0.18029	2931.6	15.603
58.2	3.4338	1540.17	0.16757	2918	15.603
60	3.54	1529.11	0.16109	2910.7	15.603
65	3.835	1500.28	0.14524	2891.8	15.603
70	4.13	1473.9	0.13195	2874.5	15.603
75	4.425	1449.62	0.12067	2858.4	15.603
80	4.72	1427.16	0.111	2843.5	15.603
85	5.015	1406.27	0.10262	2829.5	15.603
90	5.31	1386.75	0.0953	2816.4	15.603
95	5.605	1368.46	0.08885	2804	15.603
100	5.9	1351.25	0.08314	2792.3	15.603
125	7.375	1278.04	0.06226	2741.5	15.603
150	8.85	1220.18	0.04915	2700.3	15.603
175	10.325	1172.61	0.04023	2665.9	15.603
200	11.8	1132.38	0.03381	2636.4	15.603
250	14.75	1067.19	0.02529	2588.4	15.603
300	17.7	1015.8	0.01993	2550.7	15.603
350	20.65	973.67	0.01629	2519.7	15.603
400	23.6	938.14	0.01368	2493.5	15.603
450	26.55	907.54	0.01172	2471.1	15.603
500	29.5	880.76	0.01021	2451.7	15.603

Area Ratio	Area [m ²]	R_{gas}	γ	Viscosity [Pa s]	Conductivity [W/(m-K)]	Prandtl Number
CC	N/a	567.7	1.1359	0.00011092	1.78434	0.5623
1	0.059	561.3	1.1342	0.00010659	1.61818	0.5675
2	0.118	546.0	1.1365	0.000095501	1.09343	0.5867
3	0.177	541.3	1.1424	0.000091021	0.88192	0.5978
4	0.236	538.8	1.1487	0.000087883	0.748	0.6082
5	0.295	537.2	1.1549	0.000085418	0.65474	0.6188
10	0.59	534.2	1.178	0.000077431	0.43377	0.6689
15	0.885	533.4	1.1911	0.000072555	0.35177	0.7034
20	1.18	533.1	1.1992	0.000069061	0.31004	0.7242
25	1.475	533.0	1.2048	0.000066357	0.28448	0.7367
30	1.77	532.9	1.2091	0.000064162	0.26683	0.7443
35	2.065	532.9	1.2125	0.000062318	0.25362	0.7494
40	2.36	532.9	1.2155	0.000060733	0.24316	0.7523
45	2.655	532.9	1.218	0.000059344	0.23454	0.7543
50	2.95	532.9	1.2203	0.00005811	0.22722	0.7557
55	3.245	532.9	1.2223	0.000057	0.22087	0.7565
58.2	3.4338	532.9	1.2236	0.000056343	0.21721	0.7569
60	3.54	532.9	1.2242	0.000055993	0.21527	0.7571
65	3.835	532.9	1.226	0.000055072	0.21026	0.7574
70	4.13	532.9	1.2277	0.000054222	0.20573	0.7576
75	4.425	532.9	1.2292	0.000053435	0.2016	0.7577
80	4.72	532.9	1.2307	0.000052702	0.1978	0.7576
85	5.015	532.9	1.2321	0.000052016	0.1943	0.7575
90	5.31	532.9	1.2334	0.000051372	0.19104	0.7574
95	5.605	532.9	1.2347	0.000050766	0.188	0.7572
100	5.9	532.9	1.2359	0.000050192	0.18515	0.757
125	7.375	532.9	1.2413	0.000047719	0.17314	0.7556
150	8.85	532.9	1.2459	0.000045727	0.16377	0.754
175	10.325	532.9	1.2498	0.000044064	0.15615	0.7523
200	11.8	532.9	1.2533	0.000042638	0.14977	0.7506
250	14.75	532.9	1.2592	0.000040291	0.13959	0.7471
300	17.7	532.9	1.2641	0.000038404	0.1317	0.7438
350	20.65	532.9	1.2682	0.000036833	0.12531	0.7406
400	23.6	532.9	1.2718	0.000035491	0.11997	0.7377
450	26.55	532.9	1.2749	0.000034323	0.11541	0.7349
500	29.5	532.9	1.2777	0.000033291	0.11145	0.7324

Area Ratio	Hydrogen (H)	Hydrogen (H2)	Oxygen (O)	Oxygen (O2)	Hydroxyl (OH)	Hydro-Peroxyl (HO2)	Water Vapor (H2O)
CC	0.03071	0.18098	0.00576	0.00866	0.06318	0.00009	0.71059
1	0.02621	0.17464	0.00429	0.00697	0.05256	0.00005	0.73527
2	0.0146	0.15925	0.00132	0.00263	0.0256	0.00001	0.79659
3	0.01052	0.15494	0.00065	0.00138	0.01674	0	0.81576
4	0.00802	0.15287	0.00036	0.00078	0.01168	0	0.82628
5	0.00631	0.15177	0.00021	0.00046	0.00846	0	0.83279
10	0.00238	0.15049	0.00002	0.00005	0.00227	0	0.84479
15	0.00111	0.15051	0	0.00001	0.00082	0	0.84755
20	0.00059	0.15059	0	0	0.00035	0	0.84847
25	0.00034	0.15065	0	0	0.00017	0	0.84883
30	0.00021	0.1507	0	0	0.00009	0	0.849
35	0.00014	0.15072	0	0	0.00005	0	0.84909
40	0.00009	0.15074	0	0	0.00003	0	0.84914
45	0.00006	0.15075	0	0	0.00002	0	0.84917
50	0.00004	0.15076	0	0	0.00001	0	0.84919
55	0.00003	0.15076	0	0	0.00001	0	0.8492
58.2	0.00003	0.15077	0	0	0.00001	0	0.8492
60	0.00002	0.15077	0	0	0	0	0.8492
65	0.00002	0.15077	0	0	0	0	0.84921
70	0.00001	0.15077	0	0	0	0	0.84921
75	0.00001	0.15077	0	0	0	0	0.84921
80	0.00001	0.15077	0	0	0	0	0.84922
85	0	0.15078	0	0	0	0	0.84922
90	0	0.15078	0	0	0	0	0.84922
95	0	0.15078	0	0	0	0	0.84922
100	0	0.15078	0	0	0	0	0.84922
125	0	0.15078	0	0	0	0	0.84922
150	0	0.15078	0	0	0	0	0.84922
175	0	0.15078	0	0	0	0	0.84922
200	0	0.15078	0	0	0	0	0.84922
250	0	0.15078	0	0	0	0	0.84922
300	0	0.15078	0	0	0	0	0.84922
350	0	0.15078	0	0	0	0	0.84922
400	0	0.15078	0	0	0	0	0.84922
450	0	0.15078	0	0	0	0	0.84922
500	0	0.15078	0	0	0	0	0.84922

C) Gas Property Curve-Fit Coefficients and Water Models

Piece-Wise Specific Heat Coefficients [J/kgK]

Core-Flow Cp(T)		
Range [K]	Coefficient	Value
0<T<373.3	Cp1	2.138467E+03
	Cp2	0.000000E+00
	Cp3	0.000000E+00
	Cp4	0.000000E+00
	Cp5	0.000000E+00
373.3<T<1000	Cp1	2.091251E+03
	Cp2	-2.804534E-01
	Cp3	1.382517E-03
	Cp4	-8.611403E-07
	Cp5	2.084389E-10
1000<T<5000	Cp1	1.450526E+03
	Cp2	1.409464E+00
	Cp3	-3.612944E-04
	Cp4	4.390377E-08
	Cp5	-1.984747E-12

TEG Cp		
Range [K]	Coefficient	Value
0<T<373.3	Cp1	7.771914E+03
	Cp2	0.000000E+00
	Cp3	0.000000E+00
	Cp4	0.000000E+00
	Cp5	0.000000E+00
373.3<T<1000	Cp1	5.545223E+03
	Cp2	1.485738E+01
	Cp3	-3.588104E-02
	Cp4	3.744204E-05
	Cp5	-1.375930E-08
1000<T<5000	Cp1	6.303320E+03
	Cp2	2.322684E+00
	Cp3	-4.722208E-04
	Cp4	5.290216E-08
	Cp5	-2.376452E-12

Hydrogen (H2) Cp		
Range [K]	Coefficient	Value
0<T<373.3	Cp1	1.449423E+04
	Cp2	0.000000E+00
	Cp3	0.000000E+00
	Cp4	0.000000E+00
	Cp5	0.000000E+00
373.3<T<1000	Cp1	9.668389E+03
	Cp2	3.291292E+01
	Cp3	-8.033095E-02
	Cp4	8.313149E-05
	Cp5	-3.042027E-08
1000<T<5000	Cp1	1.209560E+04
	Cp2	3.409061E+00
	Cp3	-6.037862E-04
	Cp4	6.355340E-08
	Cp5	-2.840737E-12

Water-Vapor (H2O) Cp		
Range [K]	Coefficient	Value
0<T<373.3	Cp1	1.890390E+03
	Cp2	0.000000E+00
	Cp3	0.000000E+00
	Cp4	0.000000E+00
	Cp5	0.000000E+00
373.3<T<1000	Cp1	1.937761E+03
	Cp2	-9.398570E-01
	Cp3	3.009302E-03
	Cp4	-2.532813E-06
	Cp5	8.178051E-10
1000<T<5000	Cp1	1.235509E+03
	Cp2	1.372186E+00
	Cp3	-3.571109E-04
	Cp4	4.358312E-08
	Cp5	-1.970237E-12

Piece-Wise Viscosity Coefficients [Pa s]

Core-Flow Viscosity		
Range [K]	Coefficient	C.F. Value
0<T<373.3	Cnd1	1.194085E-05
	Cnd2	0.000000E+00
	Cnd3	0.000000E+00
	Cnd4	0.000000E+00
	Cnd5	0.000000E+00
373.3<T<5000	Cnd1	-5.449236E-06
	Cnd2	4.933071E-08
	Cnd3	-7.505006E-12
	Cnd4	9.485008E-16
	Cnd5	-5.174933E-20

TEG Viscosity		
Range [K]	Coefficient	C.F. Value
0<T<373.3	Cnd1	1.171720E-05
	Cnd2	0.000000E+00
	Cnd3	0.000000E+00
	Cnd4	0.000000E+00
	Cnd5	0.000000E+00
373.3<T<5000	Cnd1	1.313776E-06
	Cnd2	3.016621E-08
	Cnd3	-5.845650E-12
	Cnd4	1.098296E-15
	Cnd5	-8.001154E-20

Hydrogen (H2) Viscosity		
Range [K]	Coefficient	C.F. Value
0<T<373.3	Cnd1	1.054539E-05
	Cnd2	0.000000E+00
	Cnd3	0.000000E+00
	Cnd4	0.000000E+00
	Cnd5	0.000000E+00
373.3<T<5000	Cnd1	3.560503E-06
	Cnd2	2.005742E-08
	Cnd3	-3.901079E-12
	Cnd4	8.128144E-16
	Cnd5	-6.198858E-20

Water-Vapor (H2O) Viscosity		
Range [K]	Coefficient	C.F. Value
0<T<373.3	Cnd1	1.177245E-05
	Cnd2	0.000000E+00
	Cnd3	0.000000E+00
	Cnd4	0.000000E+00
	Cnd5	0.000000E+00
373.3<T<5000	Cnd1	-5.943931E-06
	Cnd2	5.007536E-08
	Cnd3	-7.324735E-12
	Cnd4	8.613748E-16
	Cnd5	-4.335374E-20

Piece-Wise Thermal Conductivity Coefficients [W/(m-K)]

Core-Flow Conductivity		
Range [K]	Coefficient	C.F. Value
0<T<373.3	Cnd1	3.361019E-02
	Cnd2	0.000000E+00
	Cnd3	0.000000E+00
	Cnd4	0.000000E+00
	Cnd5	0.000000E+00
373.3<T<5000	Cnd1	-1.057685E-02
	Cnd2	1.072324E-04
	Cnd3	3.626736E-08
	Cnd4	-1.009130E-11
	Cnd5	8.304801E-16

TEG Conductivity		
Range [K]	Coefficient	C.F. Value
0<T<373.3	Cnd1	2.004668E-01
	Cnd2	0.000000E+00
	Cnd3	0.000000E+00
	Cnd4	0.000000E+00
	Cnd5	0.000000E+00
373.3<T<5000	Cnd1	7.975203E-02
	Cnd2	3.230154E-04
	Cnd3	7.380581E-09
	Cnd4	-8.178555E-14
	Cnd5	-4.951594E-17

Hydrogen (H2) Conductivity		
Range [K]	Coefficient	C.F. Value
0<T<373.3	Cnd1	2.225108E-01
	Cnd2	0.000000E+00
	Cnd3	0.000000E+00
	Cnd4	0.000000E+00
	Cnd5	0.000000E+00
373.3<T<5000	Cnd1	9.573536E-02
	Cnd2	3.352151E-04
	Cnd3	1.206921E-08
	Cnd4	-8.121250E-13
	Cnd5	1.739453E-18

Water-Vapor (H2O) Conductivity		
Range [K]	Coefficient	C.F. Value
0<T<373.3	Cnd1	2.114858E-02
	Cnd2	0.000000E+00
	Cnd3	0.000000E+00
	Cnd4	0.000000E+00
	Cnd5	0.000000E+00
373.3<T<5000	Cnd1	-1.431428E-02
	Cnd2	8.001332E-05
	Cnd3	4.459608E-08
	Cnd4	-1.231069E-11
	Cnd5	1.014726E-15

Water Model	Sigma (Angstroms)
SSD	3.016
SPC	3.166
SPC/E	3.166
SPC/HW	3.166
SPC/Fw	3.166
TIP3P	3.15061
TIP3P/Fw	3.1506
iAMOEBA	3.6453
PPC	3.234
TIP4P	3.15365
TIP4P-Ew	3.16435
TIP4P-FQ	3.15365
TIP4P/ICE	3.1668
TIP4P/ 2005	3.1589
TIP4P/ 2005f	3.1644
COS/G3	3.17459
COS/D	3.4365
GCPM	3.69
SWM4-NDP	3.18395
SWM6	3.19833
ST2	3.1
TIP5P	3.12
TIP5P-Ew	3.097
POL5/TZ	2.9837
QCT	3.14
Average	3.1979

D) Matlab Script Files

```
%Mike Carkin
%AE 700 Thesis: Coordinate Manipulation

%Code Purpose: Modify Existing Nozzle Contour Coordinates to Include a
%Film Injection Inlet at a User-Defined Location.

%Clear and Close All
clc;
clear all;
close all;

%Define File Name and Excel Ranges
File_Name='VulcainIICoordinates.xlsx'; %Excel File Containing Nozzle Data
Sheet_Name='Default Coordinates'; %Excel Sheet Name
X_Range='B4:B503'; %X-Coordinate Column Range
Radius_Range='C4:C503'; %Radius Column Range
filename='Model G';

%Specify Film Cooling Injection Geometry
FC_Loc=1.0; %Axial Distance Between F.C. Inlet and Shower Head (Meters)
Slot_h=0.005; %Slot Injection Height (Meters)

%Extract 'Default' Nozzle Coordinates From Excel
X_Coords=xlsread(File_Name,Sheet_Name,X_Range);
Radius_Coords=xlsread(File_Name,Sheet_Name,Radius_Range);

%Construct Coordinate Arrays
Default_Coords(length(X_Coords),2)=zeros; %Initialize Coordinate Array
Default_Coords(:,1)=X_Coords; %Insert X-Coordinates
Default_Coords(:,2)=Radius_Coords; %Insert Radius-Coordinates
FC_Coords(length(X_Coords)+2,2)=zeros; %Initialize Film Cooling Coordinate Array

%Compare Final X-Coordinate to Film Injection Location
if Default_Coords(length(X_Coords),1)<FC_Loc
    disp('Error: Nozzle Length < Film Injection Location')
else

    %Determine Cell Indices Containing Nozzle Geometry Adjacent to Film Injection
    Cell_Count=0;
    for i=1:size(Default_Coords(:,1))
        if Default_Coords(i,1)<FC_Loc
            Cell_Count=Cell_Count+1;
        else
            end
    end

    %Extract Points Adjacent to Film Inlet
    FC_X1=Default_Coords(Cell_Count,1);
    FC_R1=Default_Coords(Cell_Count,2);
```

```

FC_X2=Default_Coords(Cell_Count+1,1);
FC_R2=Default_Coords(Cell_Count+1,2);
FC_X3=Default_Coords(Cell_Count+2,1);
FC_R3=Default_Coords(Cell_Count+2,2);

%Calculate Inner Lip Coordinates Via Interpolation
FC_IX=FC_Loc; %X-Coordinate of Film Cooling Inlet
FC_IY=abs(((FC_R2-FC_R1)*(FC_X2-FC_Loc)/(FC_X2-FC_X1))-FC_R2); %Inner Radius of Film
Cooling Inlet

%Calculate Slope and Wall Angle of Nozzle Profile Adjacent to Film Inlet
if FC_X1==FC_Loc || FC_X2==FC_Loc
    Slope1=(FC_R2-FC_R1)/(FC_X2-FC_X1);
    Slope2=(FC_R3-FC_R2)/(FC_X3-FC_X2);
    Slope=(Slope1+Slope2)/2;
    Theta=atan(Slope);
else
    %Calculate Slope of Nozzle Wall Adjacent to Film Injection if Injection is Closer to First Point
    if abs(FC_Loc-Default_Coords(Cell_Count,1)) < abs(FC_Loc-Default_Coords(Cell_Count+1,1))
        Slope=(FC_IY-FC_R1)/(FC_Loc-FC_X1);
        Theta=atan(Slope);

    %Calculate Slope of Nozzle Wall Adjacent to Film Injection if Injection is Closer to Second Point
    elseif abs(FC_Loc-Default_Coords(Cell_Count,1)) > abs(FC_Loc-Default_Coords(Cell_Count+1,1))
        Slope=(FC_R2-FC_IY)/(FC_X2-FC_Loc);
        Theta=atan(Slope);

    %Calculate Slope of Nozzle Wall Adjacent to Film Injection if Equal Distance from Points
    else
        Slope=(FC_R2-FC_R1)/(FC_X2-FC_X1);
        Theta=atan(Slope);
    end
end

%Calculate Outer Injection Lip Coordinates
if Slope>0
    FC_OX=FC_Loc-(Slot_h*sin(Theta));
    FC_OY=FC_IY+(Slot_h*cos(Theta));

elseif Slope<0
    FC_OX=FC_Loc+(Slot_h*cos((3.14159/2)-Theta));
    FC_OY=FC_IY+(Slot_h*sin((3.14159/2)-Theta));

else
    FC_OX=FC_Loc;
    FC_OY=Slot_h+FC_IY;

end

%Determine Cross Sectional Area of Film Inlet
FC_Area=3.14159*(((FC_IY+(Slot_h/cos(Theta)))^2)-(FC_IY^2));

%Generate FC Nozzle Coordinates
for i=1:Cell_Count
    for j=1:2

```



```

        FC_Coords(i,j)=Default_Coords(i,j);
    end
end

%Insert Film Injection Lip
FC_Coords(Cell_Count+1,1)=FC_IX;
FC_Coords(Cell_Count+1,2)=FC_IY;

FC_Coords(Cell_Count+2,1)=FC_OX;
FC_Coords(Cell_Count+2,2)=FC_OY;

%Connect Aft Nozzle Geometry
for i=Cell_Count+3:size(Default_Coords,1)+2
    FC_Coords(i,1)=Default_Coords(i-2,1);
end

for i=Cell_Count+3:size(Default_Coords,1)+2
    FC_Coords(i,2)=sqrt((FC_Area/3.14159)+(Default_Coords(i-2,2)^2));
    %FC_Coords(i,2)=Default_Coords(i-2,2)+1.2*(Slot_h*cos(Theta)); BS
end

end

%Write FC Coordinates to Excel File
xlswrite(File_Name,FC_Coords,filename)

dist=sqrt(((FC_IX-FC_OX)^2)+((FC_IY-FC_OY)^2))

```

%Gas Mixture Specific Heat Calculator

%NASA GAS POLYNOMIALS

```
%Cp/R = a1 + a2 T + a3 T^2 + a4 T^3 + a5 T^4  
%H/RT = a1 + a2 T / 2 + a3 T^2 / 3 + a4 T^3 / 4 + a5 T^4 / 5 + a6/T  
%S/R = a1 lnT + a2 T + a3 T^2 / 2 + a4 T^3 / 3 + a5 T^4 / 4 + a7  
%Information Obtained from NASA TM 4513  
%Temperature Range: 0K < T < 1000K, 1000K < T < 5000K
```

```
%Clear Screen and Variables
```

```
clc;  
clear;
```

```
%Inputs
```

```
Temp=1400; %Kelvin
```

```
%%
```

```
%{
```

```
%Mole Fractions at A/A*=10
```

```
n=8; %Number of species
```

```
xH=0.00238;
```

```
xH2=0.15049;
```

```
xO=0.00002;
```

```
xO2=0.00005;
```

```
xOH=0.00227;
```

```
xH2O=0.84479;
```

```
xHO2=0;
```

```
xH2O2=0;
```

```
%}
```

```
%Mole Fractions of TEG
```

```
n=8; %Number of species
```

```
xH=0;
```

```
xH2=0.8866;
```

```
xO=0;
```

```
xO2=0;
```

```
xOH=0;
```

```
xH2O=0.1134;
```

```
xHO2=0;
```

```
xH2O2=0;
```

```
%{
```

```
%Mole Fractions of H2 Gas
```

```
n=8; %Number of species
```

```
xH=0;
```

```
xH2=1;
```

```
xO=0;
```

```
xO2=0;
```

```
xOH=0;
```

```
xH2O=0;
```

```
xHO2=0;
```

```
xH2O2=0;
```

```
%}
```

```
%{
```

```
%Mole Fractions of Water Vapor
```

```
n=8; %Number of species
```

```

xH=0;
xH2=0;
xO=0;
xO2=0;
xOH=0;
xH2O=1;
xHO2=0;
xH2O2=0;
%}

%Check Mole Fractions
CheckMF=xO+xO2+xH+xH2+xOH+xH2O+xHO2+xH2O2

%Molecular Masses (g/mol or Kg/kmol)
MmH=1.008;
MmH2=2*1.008;
MmO=15.999;
MmO2=2*15.999;
MmOH=1.008+15.999;
MmH2O=1.008+1.008+15.999;
MmHO2=15.999+15.999+1.008;
MmH2O2=15.999+15.999+1.008+1.008;

%Gas Constants
RH=8314.3/MmH;
RH2=8314.3/MmH2;
RO=8314.3/MmO;
RO2=8314.3/MmO2;
ROH=8314.3/MmOH;
RHO2=8314.3/MmO2;
RH2O=8314.3/MmH2O;
RH2O2=8314.3/MmH2O2;

%Mass Fractions
Mtotal=(xH*MmH)+(xH2*MmH2)+(xO*MmO)+(xO2*MmO2)+(xOH*MmOH)+(xH2O*MmH2O)+(xHO
2*MmHO2)+(xH2O2*MmH2O2);
MfH=xH*MmH/Mtotal;
MfH2=xH2*MmH2/Mtotal;
MfO=xO*MmO/Mtotal;
MfO2=xO2*MmO2/Mtotal;
MfOH=xOH*MmOH/Mtotal;
MfH2O=xH2O*MmH2O/Mtotal;
MfHO2=xHO2*MmHO2/Mtotal;
MfH2O2=xH2O2*MmH2O2/Mtotal;

%Molecular Weight
MW_mix=(xH*MmH)+(xH2*MmH2)+(xO*MmO)+(xO2*MmO2)+(xOH*MmOH)+(xH2O*MmH2O)+(x
HO2*MmHO2)+(xH2O2*MmH2O2)

%Define Symbolic Temperature Variable
T=sym('T');

%Calculate Cp Polynomial
if Temp<1000 %Temp < 1000 K
    %Set O Coefficients
    Ocp1=3.1682671E+00;

```

Ocp2=-3.27931884E-03;
Ocp3=6.64306396E-06;
Ocp4=-6.12806624E-09;
Ocp5=2.11265971E-12;

%Set O2 Coefficients

O2cp1=3.78245636E+00;
O2cp2=-2.99673415E-03;
O2cp3=9.84730201E-06;
O2cp4=-9.68129509E-09;
O2cp5=3.24372837E-12;

%Set H Coefficients

Hcp1=2.50000001E+00;
Hcp2=0;%-2.30842973E-11;
Hcp3=0;%1.61561948E-14;
Hcp4=0;%-4.73515235E-18;
Hcp5=0;%4.98197357E-22;

%Set H2 Coefficients

H2cp1=2.34433112E+00;
H2cp2=7.98052075E-03;
H2cp3=-1.94781510E-05;
H2cp4=2.01572094E-08;
H2cp5=-7.37611761E-12;

%Set OH Coefficients

OHcp1=3.99201543E+00;
OHcp2=-2.40131752E-03;
OHcp3=4.61793841E-06;
OHcp4=-3.88113333E-09;
OHcp5=1.36411470E-12;

%Set H2O Coefficients

H2Ocp1=4.19864056E+00;
H2Ocp2=-2.03643410E-03;
H2Ocp3=6.52040211E-06;
H2Ocp4=-5.48797062E-09;
H2Ocp5=1.77197817E-12;

%Set HO2 Coefficients

HO2cp1=4.30179801E+00;
HO2cp2=-4.74912051E-03;
HO2cp3=2.11582891E-05;
HO2cp4=-2.42763894E-08;
HO2cp5=9.29225124E-12;

%Set H2O2 Coefficients

H2O2cp1=4.27611269E+00;
H2O2cp2=-5.42822417E-04;
H2O2cp3=1.67335701E-05;
H2O2cp4=-2.15770813E-08;
H2O2cp5=8.62454363E-12;

else (Temp>1000)&&(Temp<5000); %Temp>1000 K
%Set O Coefficients

Ocp1=2.54363697E+00;
Ocp2=-2.73162486E-05;
Ocp3=-4.19029520E-09;
Ocp4=4.95481845E-12;
Ocp5=-4.79553694E-16;

%Set O2 Coefficients

O2cp1=3.660960834E+00;
O2cp2=6.56365523E-04;
O2cp3=-1.41149485E-07;
O2cp4=2.05797658E-11;
O2cp5=-1.29913248E-15;

%Set H Coefficients

Hcp1=2.50000001E+00;
Hcp2=-5.6533424E-09;
Hcp3=3.63251723E-12;
Hcp4=-9.19949720E-16;
Hcp5=7.95260745E-20;

%Set H2 Coefficients

H2cp1=2.93286579E+00;
H2cp2=8.26607967E-04;
H2cp3=-1.46402335E-07;
H2cp4=1.54100359E-11;
H2cp5=-6.88804432E-16;

%Set OH Coefficients

OHcp1=2.83864607E+00;
OHcp2=1.10725586E-03;
OHcp3=-2.93914978E-07;
OHcp4=4.205242476E-11;
OHcp5=-2.42169092E-15;

%Set H2O Coefficients

H2Ocp1=2.67703787E+00;
H2Ocp2=2.97318329E-03;
H2Ocp3=-7.73769690E-07;
H2Ocp4=9.44336689E-11;
H2Ocp5=-4.26900959E-15;

%Set HO2 Coefficients

HO2cp1=4.17228728E+00;
HO2cp2=1.88117647E-03;
HO2cp3=-3.46277408E-07;
HO2cp4=1.94657853E-11;
HO2cp5=1.76254294E-14;

%Set H2O2 Coefficients

H2O2cp1=4.57333537E+00;
H2O2cp2=4.04984070E-03;
H2O2cp3=-1.29479479E-06;
H2O2cp4=1.97281710E-10;
H2O2cp5=-1.13402846E-14;

end

%Cp(T) Polynomials

```
CpO=RO*(Ocp1+Ocp2*T+Ocp3*T^2+Ocp4*T^3+Ocp5*T^4);  
CpO2=RO2*(O2cp1+O2cp2*T+O2cp3*T^2+O2cp4*T^3+O2cp5*T^4);  
CpH=RH*(Hcp1+Hcp2*T+Hcp3*T^2+Hcp4*T^3+Hcp5*T^4);  
CpH2=RH2*(H2cp1+H2cp2*T+H2cp3*T^2+H2cp4*T^3+H2cp5*T^4);  
CpOH=ROH*(OHcp1+OHcp2*T+OHcp3*T^2+OHcp4*T^3+OHcp5*T^4);  
CpH2O=RH2O*(H2Ocp1+H2Ocp2*T+H2Ocp3*T^2+H2Ocp4*T^3+H2Ocp5*T^4);  
CpHO2=RHO2*(HO2cp1+HO2cp2*T+HO2cp3*T^2+HO2cp4*T^3+HO2cp5*T^4);  
CpH2O2=RH2O2*(H2O2cp1+H2O2cp2*T+H2O2cp3*T^2+H2O2cp4*T^3+H2O2cp5*T^4);
```

%Construct Symbolic Mathematical Expression and Simplify

```
Cpgas=(MfO*CpO)+(MfO2*CpO2)+(MfH*CpH)+(MfH2*CpH2)+(MfOH*CpOH)+(MfH2O*CpH2O)+(MfHO2*CpHO2)+(MfH2O2*CpH2O2);  
MCpgas=vpa(Cpgas)
```